University of Groningen

Kapteyn Insitute

Disk Structure and the Search for Keplerian Rotation around Young High-Mass Stars

Author:
Jim Morrison

Advisor:
prof. dr. Floris van der Tak

June 2020

Dedication and Acknowledgement

This thesis would not be possible if not for the help of many people. Thank you to Dr. Jonathan Tan of Chalmers University and Dr. Riccardo Cesaroni of Arcetri for taking the time to provide input and advice on this project. Thank you to Dr. John Tobin and Dr. Mark Lacy of NRAO for assisting me with handling some particularly tricky ALMA files. Another thank you to Felix Bosco of the Max Planck Institute for personally assisting me with his *KeplerFit* code.

A big thank you is in order to my Advisor, Prof. dr. Floris van der Tak, for his guidance throughout this project.

Thank you to my parents who have supported me every step of the way, despite me moving 6000 KM away.

And last but not least, the biggest thanks goes to my Wife, Anna, who is my biggest inspiration and gave me the courage to begin this journey, and stick with it to the end.

Contents

Chapter 1

Introduction

1.1 Importance of High-Mass Stars

High-mass stars, defined as having a mass of 8 $M_{\odot}$ or greater, are keystone components in shaping the interstellar medium (ISM), impacting star-forming regions, galaxy formation, and galactic evolution. High-mass protostars produce powerful radiation, high luminosities ($>10^3$ $L_{\odot}$), and stellar winds. They are a key source of heavy elements, produced via nucleosynthesis during their stellar evolution, and released into the local ISM via supernova explosions. They are influential subjects in both astrophysics and astrochemistry. Despite the considerable impact of high-mass stars, their formation remains poorly understood, particularly in comparison to their lower mass counterparts.

1.2 Low-Mass Star Formation

In the case of low-mass star formation (M < 2 $M_{\odot}$), the formation process is well known, with many in-depth studies (Shu *et al.,* 1987, McKee *et al.,* 2007). The initial stages of star formation occur in giant clouds of molecular gas, several parsecs in size, at cold temperatures (10-50 K), and mainly composed of H_2 molecules. Recent *Herschel Space Observatory* observations have found these clouds are often comprised of extended filamentary structures (André, 2017), hosting many star forming regions (e.g. Figure 1.1). The filaments are believed to be formed via magnetic fields. The Planck Collaboration (Adam *et al.,* 2016, Ade *et al.,* 2016) revealed that magnetic field lines are aligned with low-density filaments, and perpendicular to higher density, star-forming filaments, indicating that the formation and evolution of star forming filaments occurs from matter accumulation via magnetic field lines. The subsequent stages of formation can be seen in Figure 1.2. Within the giant molecular clouds form Infrared Dark Clouds (IRDCs) filaments (Perault *et al.,* 1996). The IRDCs are named as such due to their high column densities (10^{23}-10^{25} cm^{-2}), making them optically thick at mid-IR wavelengths. Within the IRDCs, gravitational instabilities cause fragmentation and molecular clump formation (Tan, 2018). Within the clumps, temperatures decrease to below

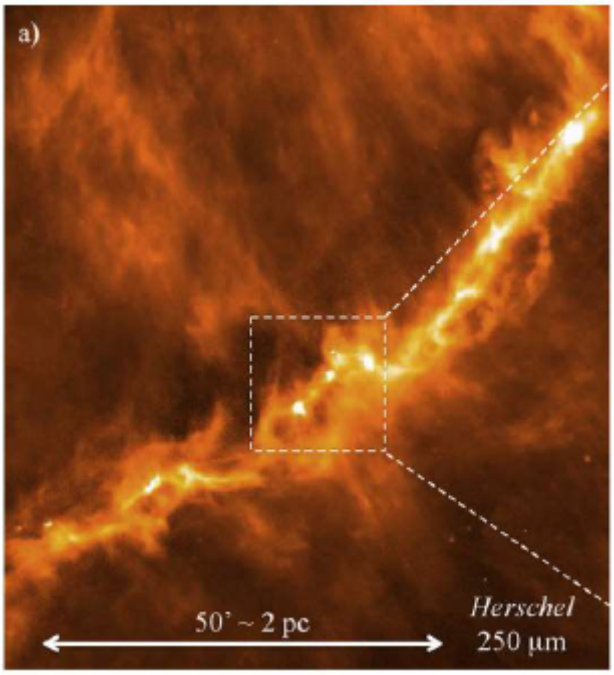

Figure 1.1: *Herschel*/SPIRE 250 µm dust continuum image of the Taurus B211/B213 filament, with several notable dense cores visible (from Palmeirim, P. *et al.,* 2013).

10 K, followed by a global infall to form a dense core. These cores are typically less than 0.2 parsecs in size and have a density of 10^{4-5} cm^{-3} (Wang, 2013). Infall occurs when the gravitational potential energy of the clump within the cloud exceeds the pressure of outward forces, such as kinetic energy and turbulence. This occurs when the core reaches a specific mass, also know as the Jeans' Mass, given by equation 1.1. Here k is the Boltzmann constant, T is the temperature of the gas, G is the gravitational constant, μ is the mean molecular mass, m_H is the mass of hydrogen and ρ_C is the density of the core.

$$M_J = (\frac{5kT}{G\mu m_H})^{3/2}(\frac{3}{4\pi\rho_C})^{1/2} \tag{1.1}$$

During this collapse, mass is transferred inward from the outer envelope leading to a pre-stellar core. To conserve angular momentum during this collapse, circumstellar disks in Keplerian rotation form around the central core, and any additional angular momentum is released in the form of bipolar outflows. As matter is accreted onto the core from the outer envelope, a pre-main sequence (PMS) star forms surrounded by a protoplanetary disk. Eventually the surrounding material is exhausted, accretion ceases, and the outflows are terminated. The PMS star contracts until it reaches the hydrogen burning phase and the main sequence. The timescale of this process is determined via the Kelvin-Helmholtz timescale (eq. 1.2, M is stellar mass, R is stellar radius and L is luminosity of the star).

$$t_{KH} = \frac{GM^2}{RL} \tag{1.2}$$

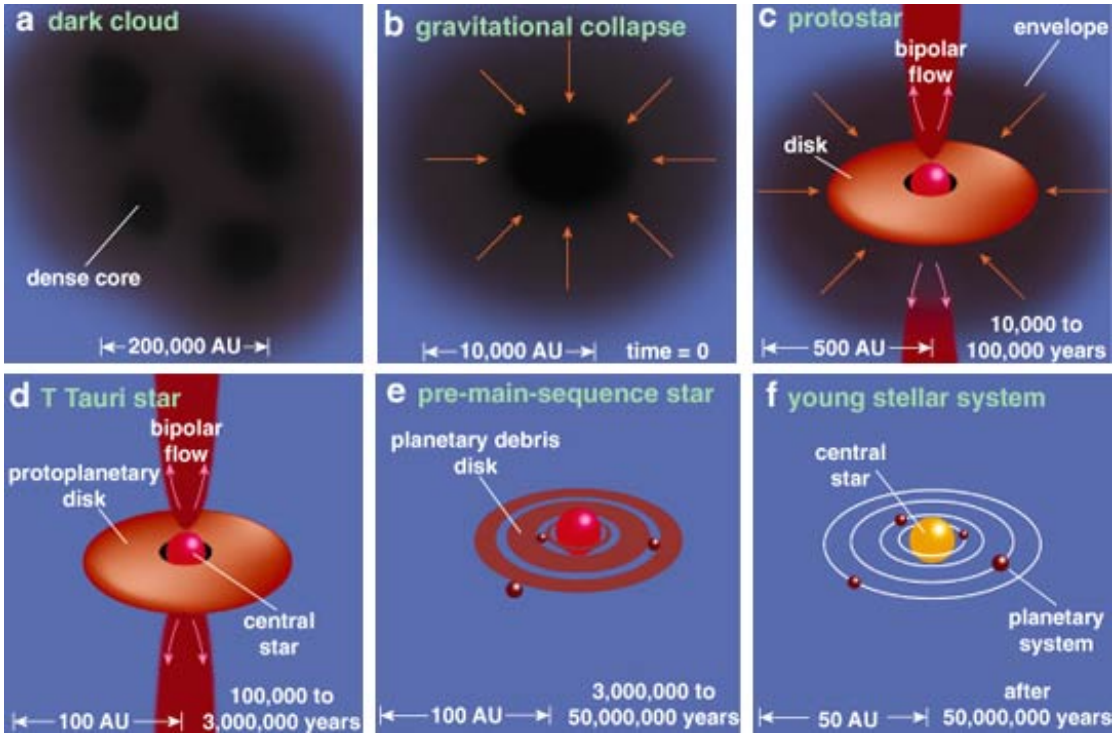

Figure 1.2: Evolutionary stages of low-mass star formation (from Greene, 2001)

Overall, this process is relatively slow, transpiring around 10^7 years or more and constituting around 0.1% of the star's life span (McKee *et al.,* 2007). The accretion time, $t_{acc} = M_*/\dot{M}_{acc}$ (where M_* is the stellar mass and $\dot{M}_{acc}$ is the mass accretion rate) is small due to their low-mass. Thus, the accretion time is much smaller than the KH timescale, and the low-mass pre-stellar object reaches the main sequence well past its accretion phase. The stellar initial mass function (IMF) indicates that low-mass stars formed at much greater rates that high-mass stars (Salpeter, 1955). Thus, low-mass stellar objects are both visible and plentiful in our local field of view, resulting in many detections and observations.

1.3 High-Mass Star Formation

Table 1.1 displays the properties and scales of high-mass star forming regions (HMSFRs). Similar to low-mass stars, high-mass star formation is localized within dense cores and clumps within giant molecular clouds. However, these clouds require much higher masses; a cloud in the order of 10^3 and 10^5 $M_\odot$ is needed form stars of 8-50 $M_\odot$ (Zinnecker *et al.,* 2007). Within the clouds form clumps of higher density, which are birthplaces of the young stellar objects (YSOs), often formed in binaries or small groups (Motte *et al.,* 2018). The clumps encompassing high-mass protostars are heated internally through stellar radiation, outflows and shocks, producing smaller scale, high temperature hot core regions. At very small scales (100 - 1000 AU), potential disk structures may form, assuming formation scenarios similar to low-mass objects.

Table 1.1: Approximate properties and scales of high-mass star forming regions, similar to that of Hirota, 2018

Object	Size	Mass	Temperature	Density
	AU	$M_\odot$	K	cm^{-3}
Cloud	$>10^6$	>1000	10-20	10^2-10^4
Clump	10^5-10^6	$\sim$100	10-20	10^4-10^6
Core	10^3-10^4	$\sim$10	$\sim$100	$>10^6$
Disk	10^2-10^3	$\sim$1	100-1000	$>10^7$

While the general formation regions and scales are understood, the mechanism that produces the YSOs is not. Young high-mass star formation is difficult to study for several reasons; first being, high-mass stars are less populous than their low-mass counterparts. This is in part a result of having much shorter lifetimes. With luminosities exceeding $>10^3$ $L_\odot$, massive YSO Kelvin-Helmholtz timescales are very short, while accretion timescales are high. Therefore, high-mass stars reach the main sequence much more quickly (approximately 10^5 years, Motte *et al.,* 2018) while still in the accretion phase, and live much shorter lives. Another consequence of this rapid evolution is that young massive stars are often still completely embedded in their surrounding envelope when they reach the main sequence. As a result, they are not visible at conventional optical wavelengths, and must be probed in centimeter to far-infrared wavelengths to penetrate the envelope. Until the creation of large arrays such as ALMA, instruments were unable to view these objects with sufficient resolution to perform studies on small-scale structures surrounding the protostars.

While observations remained problematic, two main theories have been developed for the formation of high-mass stars: Core Accretion and Competitive Accretion.

Core Accretion:

The Core Accretion theory is based on the assumption that the initial conditions of high-mass stars are scaled up versions of their low-mass counterparts, i.e., gravitationally bound cores. However, this model includes some key differences; stars of high-mass will need more massive clouds and higher accretion rates to form. These accretion rates are expected to be 10^{-4} to 10^{-5} $M_\odot yr^{-1}$, but can reach as high as 10^{-3} $M_\odot yr^{-1}$ in episodic bursts (Tan *et al.,* 2014). The core accretion model has three main challenges. First, the radiation produced from the increased accretion and from the protostar would be strong enough to hinder or even halt accretion, thus preventing the necessary conditions needed to continue mass gain to reach the sizes observed. Second, massive molecular clouds should fragment into smaller clouds, as dictated via Jeans' instability; these smaller molecular clouds would then not contain the necessary masses to form high-mass protostars. Finally, for the Core Accretion theory to hold, disks would form around the massive stars to conserve angular momentum. However, as recently as 2015 there were

only a handful of observed B-type disk candidates (Cesaroni *et al.,* 2007, Beltrán *et al.,* 2011b), with even fewer O-type candidates (Wang *et al.,* 2012, Zapata *et al.,* 2015), which were often found to be slow rotating, massive (>100 $M_{\odot}$) toroid structures (Beltrán *et al.,* 2016).

Solutions to the Core Accretion issues have been proposed; (Yorke *et al.,* 1999) suggested, as in the low-mass scenario, outflows provide an outlet for radiation to escape, preferentially in the bipolar direct. This is known as the flashlight effect, and keeps accretion rates high enough to stimulate high mass stellar formation. Furthermore, high-mass stars produce powerful and dynamic magnetic fields, increasing the turbulence of the surrounding material. This turbulence can produce ram pressure that would prevent fragmentation. Finally, the third concept of disk structures around high-mass stars has been partially solved, thanks to high-resolution instruments such as ALMA, with confirmed disk detections of B-type stars in particular (e.g. Moscadelli *et al.,* 2019, Ginsburg *et al.,* 2018). O-type stars remained elusive until Johnston *et al.,* 2015 found Keplerian signatures in the 25 $M_{\odot}$ star AFGL 4176. However, the lack of consistency of detections of disks is a major factor for the design of this study.

Competitive Accretion:

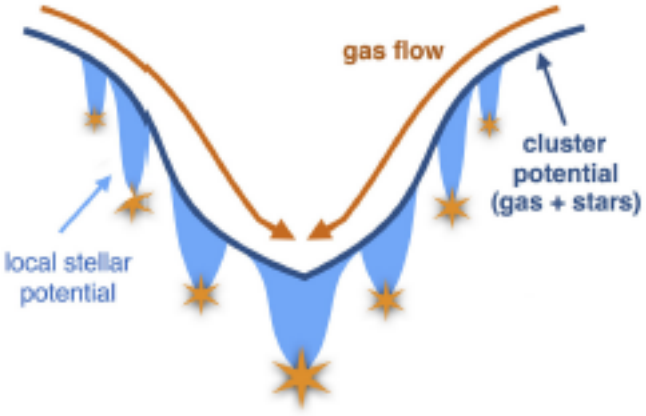

Figure 1.3: Illustration of the Competitive Accretion theory (Wright, 2015)

The Competitive Accretion theory (Bonnell *et al.,* 2001) is a "clump-fed" model. Within a molecular cloud, clumps will form containing several small cores. These cores gravitationally collapse and compete with each other for the surrounding gas. The most massive cores grow more quickly and intake more surrounding gas, and gas is funneled onto the main core from a wide region encompassing the clump. In contrast to the core accretion theory, this gas never constituted part of a gravitationally bound core enclosing the stellar object. In higher density situations, stellar collisions can increase the mass of the most influential star.

The model is based on the observational fact that stars usually form in clustered environments, with a primary massive star surrounded by a population of lower mass protostars (Zinnecker *et al.,* 2007). Furthermore, competitive accretion often leads naturally to the stellar initial mass function (Bonnell, 2007). However, Tan *et al.,* 2014 shows that the accretion rate of the Competitive Accretion model are not fast enough to produce massive stars. This model also suffers from the challenges of outward radiation pressure/outflows from accretion. Again, disks are expected to form in the model, but would be smaller than those in the Core Accretion model.

1.4 Circumstellar Disks

In low-mass star formation, much of the newborn star's growth occurs through accretion from circumstellar disks. The disks of pre-main sequence (PMS) stars have been confirmed via extensive studies and reviews (e.g. Mundy *et al.,* 2000).

Alternatively, circumstellar disks for massive star formation has proven to be problematic, both theoretically and observationally. Disk hindering effects such as stellar winds, outward radiation pressure and photo evaporation are all linked with massive stars and massive disks suffer dissipation effects at AU scales due to viscous accretion (Cesaroni *et al.,* 2006). Despite the problematic nature of high-mass protostar formation, high-mass stars are still detected and thus must be formed through some mechanism. If this mass accumulation mechanism is accretion, then a circumstellar disk must form. Despite their ambiguity, these disks remain a popular physical interpretation of high-mass star formation, for several reasons. For example, a symmetric rotating disk in Keplerian rotation, formed due to angular momentum, could allow for radiation escape in the polar direction (Yorke *et al.,* 1999). In turn high accretion rates would remain unhindered and allow the protostars to reach their massive sizes. Observationally, determining disk structure and morphology has proven difficult, given their deeply embedded nature within the surrounding envelope. Thus, the distinction between disk and envelope can be ambiguous. A velocity gradient displaying a systemic shift may be an indication of rotation, but also could be due to infalling gas or outflows. Therefore, an important criterion to determine the separation of disks from envelopes is if the velocity gradient is perpendicular to the systematic velocity at larger scales.

Until the last decade, B-type disk detection proved to be difficult, and O-type detection was non-existent, whether due to observational biases, limited sensitivity or simply a lack of disks existing around the stars. Fortunately, this has changed in the past five or so years, thanks to high-resolution instruments such as ALMA. Signatures of disks have been observed around high-mass protostars at an increasing rate in recent years. The disks that have been detected are fractionally larger than their low-mass counterparts; the ratio of disk mass to stellar mass of low-mass PMS is $< 0.1\ M_{\odot}$ (Cesaroni *et al.,* 2006), while in the high-mass case this ratio can reach upwards to, or even above 1. This result is expected, as a

inside-out collapse with a constant accretion rate results in disk mass profiles of R $\propto$ M^3 (Terebey *et al.,* 1984). While expected, this poses a new issue of stability, particularly in cases where the disk is almost equal mass of the central core. In both high-mass formation models, the angular momentum is transferred outwards via viscous torques as a result of gravitational and magneto-rotational instabilities (MRI), producing spiral arms and possible fragmentation to binary/multiple systems (Kratter *et al.,* 2010). High gas temperatures and high rotation velocities are key for disk stabilization; thus, the outer radii of the disk are particularly susceptible to instability and fragmentation.

In the Core Accretion model, a massive disk will be in non-Keplerian rotation as the envelope transitions from infall to rotational stability and circular orbits. Once the infall envelope has ceased, a lower-mass Keplerian disk may remain, until it also dissipates from accretion or feedback (Tan *et al.,* 2014). This aspect of Keplerian rotation is particularly important. Keplerian rotation is the predicted result of gravitational collapse disk formation and is observed in many low-mass cases (e.g. Aso *et al.,* 2017). While identifying Keplerian rotation in a disk is paramount for confirmation of the Core Accretion theory, the lack of detection does not necessarily indicate that there is/was no disk; the source may just be in another stage of its evolution.

1.5 Chemistry of High-Mass Star Formation

Radiation and outflows produced by YSOs can yield a rich composition of complex molecules in HMSFRs. The composition is essential to determine formation history, evolutionary timescales, tracing dynamics and establishing physical properties. The most complex molecules are predominantly formed via grain-surface reactions throughout three main phases (van der Tak, 2005): the cold 'dark cloud' phase (T $\sim$ 10 K), the warm-up phase (T = 10-100 K), and the hot core phase (T $>$ 100 K). The cold phase occurs during gravitational collapse. Here the temperature is low enough to form icy mantles on dust grains within the core. The mantles are predominantly made of H_2O, CO and CO_2, followed by CH_3OH, NH_3 and CH_4 (Öberg *et al.,* 2011). The icy mantles provide a location for molecules to accrete and react to form new species. As the temperature increases from 10-100 K during the warm-up phase, the protostar heats the surrounding gas and dust. During this phase the first complex organic molecules (COMs) are hypothesized to form on the grain mantles (Tielens *et al.,* 1982). At temperatures of 25-30 K, H_2 evaporates, allowing more complex molecules to diffuse within the mantles (Oberg *et al.,* 2013). The temperature then continues to rise into the hot core phase. Here the sublimation of the icy mantles occurs, the COMs are released. During the hot core phase all ices are sublimated, and only gas-phase chemistry occurs, initiating new chemical reactions and species formation. Other reactions may occur from subsequent outflows and feedback produced by the protostar. Feedback events shock the gas, facilitating activation energy reactions (Bell *et al.,* 2014).

With extreme formation environments, high-mass star forming regions continue to

intrigue with their chemical abundances and compositions. Recent studies show the chemical composition of HMSFRs can vary from one another, and even between sources within the region (Watanabe *et al.,* 2017), possibly due to differences in mass and luminosity of the central objects. Links between the chemical composition, physical properties and evolution in HMSFRs are possible, but currently remains a topic open for interpretation.

In this study, we will focus on the molecule methyl cyanide (CH_3CN, also known as acetonitrile). It was first detected by Solomon *et al.,* 1971 in the molecular clouds of Sgr A and Sgr B2. Solomon *et al.,* 1971 simultaneously observed six closely spaced lines of different excitation levels of the J=6-5 transition. CH_3CN has a prolated symmetric top structure, producing several emission lines in small frequency spans, which can be observed and analyzed fairly easily, minimizing uncertainties. Each J-transition has an associated K-line "ladder"; a set of increasing K-transitions that span a wide range of energies over a narrow spectral window. The symmetric rotational structure of CH_3CN is particular adept at tracing kinetic temperatures up to nearly 1000 K (Bell *et al.,* 2014).

There remains some uncertainty around the formation method of CH_3CN, although it is believed to form similarly to many COMs via grain-surface reactions during the cold collapse phase; here CN combines with elemental atoms in succession on icy mantles:

$$CN \rightarrow C_2N \rightarrow HC_2N \rightarrow CH_2CN \rightarrow CH_3CN$$

The CH_3CN is then released when the ices evaporate as surrounding temperatures increase above 90 K (Garrod *et al.,* 2008). While this is believed to be the dominant formation route, it is hypothesized that moderate abundances are formed in gas-phase reactions of HCN and CH_3^+ ions, particularly at temperatures above 40 K (Garrod *et al.,* 2017) with the addition of HCN molecules into the gas phase. Bell *et al.,* 2014 demonstrates the possibility to further enhance CH_3CN abundances via shocks. Grain mantle "sputtering" in the shock front releases species that have yet to be sublimated from the mantles back into the gas phase. Further gas phase chemistry can then occur with the newly released molecules, as the shocked gas cools down.

While the basics of high-mass star formation has been covered above, more extensive reviews have been produced in recent years (e.g. Tan *et al.,* 2014, Motte *et al.,* 2018) covering the theoretical aspects behind the formation process.

1.6 ALMA and the Search for High-Mass Stars

As previously mentioned, due to relative rarity and difficulty of detection, many fundamental questions remain about the formation process of these objects. Since high-mass star formation occurs in small dense clusters, often found at large distances, achieving high spatial resolution and sensitivity is a serious problem for observations, particularly in infrared and submillimeter wavelengths that are

needed to pierce the outer envelope. Large scale surveys, using instruments such as Herschel, Planck and Spitzer have provided many candidate young stellar objects high-mass star forming regions, however, the resolution is limited 1-10" with these surveys (see Figure 1.4).

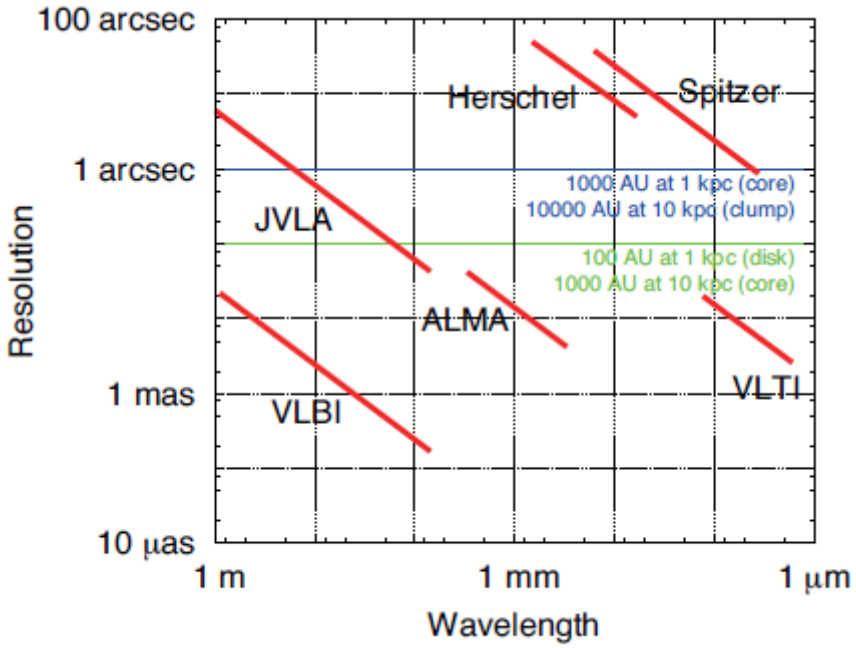

Figure 1.4: Angular resolutions for four interferometers (JVLA, ALMA, VLBI, VLTI), Herschel and Spitzer telescopes. Red lines correspond to highest resolutions of the instrument. Blue line and green line represent angular beam sizes in which 0.1 and 1.0 arcseconds, respectively, can be resolved. Image from Hirota, 2018.

Thanks to radio facilities constructed in recent decades, the astronomical community can now investigate the unknowns of high-mass star formation with greater detail. Facilities such as Jansky Very Large Array (JVLA), Northern Extended Millimeter Array (NOEMA), and the Very Long Baseline Array (VLBA), have been crucial in advancing high-mass star formation research. The Atacama Large (sub)Millimeter Array (ALMA) in particular increased sensitivities and resolutions by on order of magnitude or larger than previously constructed arrays (Hirota, 2018). Composed of 66 antennas, ALMA operates at wavelengths between 0.3 - 3.5 mm. ALMA has the capability to resolve down to scales of 100-1000 AU, ideal for investigating disks and outflows associated with the central YSO. ALMA observations have produced high quality disk studies for low-mass stars (such as in Figure 1.5), in addition to high-mass stars (e.g. Cesaroni *et al.,* 2007, Cesaroni *et al.,* 2017); studies in which this thesis forms its basis on.

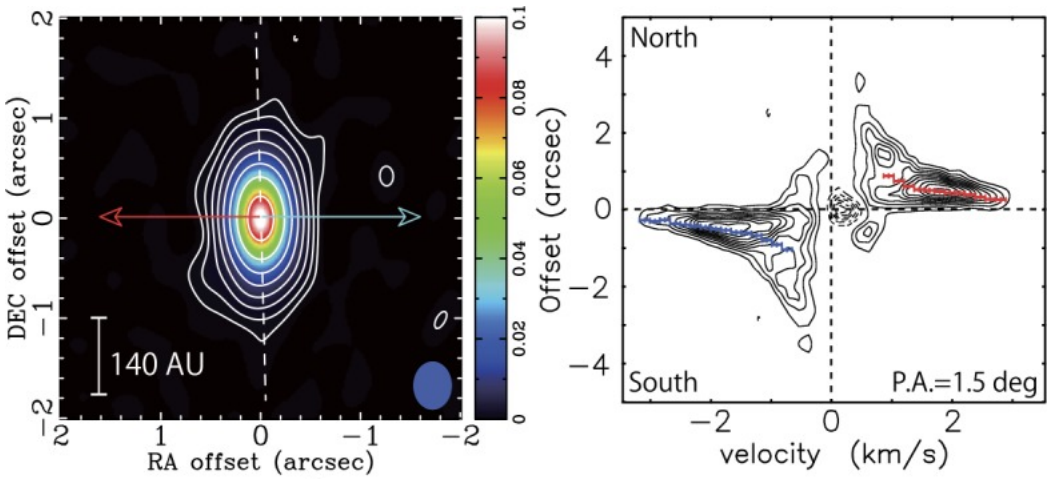

Figure 1.5: ALMA observations of the low mass (0.45 $M_{\odot}$) protostar L1527 IRS, from Aso *et al.*, 2017. *Left:* Dust continuum image of 1.3 mm emission with outflow directions (arrows). *Right:* Position velocity diagram with PV fitting.

1.7 Goals of this Thesis

In recent years, many studies have been published utilizing ALMA to investigate high-mass star forming regions, examining and probing disk properties. These studies often focused on a single source in-depth, or a population with more widespread discussion. While disks have been discovered surrounding high-mass stars, they have not been found to be universal around high-mass protostars, especially amongst O-type stars.

In this thesis, a sample of high-mass protostars will be studied. The questions that will be addressed in this study are the following:

- What are the structure surrounding high-mass stars? Are they disks?
- Are the structures in rotation, and if so, is it Keplerian rotation?
- What is the distribution of the physical and thermal properties within the disk/structure?

This study will use available data from the ALMA archive database[1] from previous studies with CH_3CN spectra and continuum data. It will be organized in the following manner: In Section 2, the methodology explaining the data acquisition, analysis and techniques used. In Section 3, the results of data analysis, in conjunction with an interpretation in the context of the research questions will be presented. In Section 4, a comparative discussion of the sample will take place, and a final classification of the structures will be determined. This will be followed by a discussion of potential uncertainties in the analysis. Finally, in Section 5 the thesis will close with a summary, conclusions, and recommendation for further work.

[1]The ALMA archive can be found at almascience.nrao.edu/aq/

Chapter 2

Methodology

2.1 Target Selection

Table 2.1: Target Sample with general properties.

Source	Right Ascension	Declination	V_{sys}	d	Angular Res		Spectral Res	CH_3CN Lines	
	(hms)	(°′″)	(km s^{-1})	(kpc)	(″)	(AU)	(km s^{-1})	J'→J"	K
AFGL 4176	13 43 01.704	-62 08 51.23	-52.0	4.2	0.47	1974	0.57	13-12	5-8
G23.01 -0.41	18 34 40.290	-09.00.38.30	+77.4	4.6	0.16	736	0.66	12-11	0-7
G24.78 +0.08	18 36 12.661	-07 12 10.15	+111.0	7.7	0.15	1155	0.66	12-11	0-8
G29.96 -0.02	18 46 03.665	-02 39 22.00	+98.0	5.3	0.35	1855	1.24	12-11	0-8
G34.43 +0.24MM1	18 53 18.007	+01 25 25.53	+59.7	3.7	0.34	1258	1.24	12-11	0-8
G35.03 +0.35	18 54 00.645	+02 01 19.23	+49.5	3.2	0.18	576	0.83	19-18	0-8
G35.20 -0.74N	18 58 13.027	+01 40 35.94	+30.0	2.2	0.18	396	0.83	19-18	0-9
G37.55 +0.20	18 59 10.348	+04 12 18.22	+85.4	6.7	0.99	6633	0.66	6-5	0-5

The goal of this thesis is to obtain properties and analyze structure of disks around high-mass protostars. To obtain the appropriate data, literature searches were conducted on investigations of O and B-type protostars that utilized ALMA for observations. The core of this thesis focuses on methyl cyanide (CH_3CN) spectra for data analysis, so further examination of the ALMA archive data was completed to look for adequate CH_3CN lines. The CH_3CN spectrum ideally contains K-lines covering energy ranges over several hundred Kelvin (preferrably 0-500 K), with minimal blending. Candidate sources were also found with the criteria used by Cesaroni *et al.,* 2017 via the RMS database[1](Lumsden *et al.,* 2013):

1. Object labelled as YSO.
2. Luminosity $>10^4$ $L_\odot$, for minimum B-type stars. Preference given to those with $>10^5$ $L_\odot$ for O-type stars.
3. Distance <8 kpc to maximize potential candidates without reducing resolution.

[1]This paper made use of information from the Red MSX Source survey database at http://rms.leeds.ac.uk/cgi-bin/public/RMS_DATABASE.cgi which was constructed with support from the Science and Technology Facilities Council of the UK.

4. If possible, known association with jets/outflows in literature

Table 2.1 lists the final target population studied in this thesis, including their coordinates, systematic velocities, distances, spectral and angular resolutions, and spectral CH_3CN emission lines. The corresponding ALMA project codes used can be found at the end of Section 5. While several targets are single high-mass stellar cores, some targets are high-mass star forming regions containing several cores. In these cases, the majority of the analysis focuses on the largest core, particularly when in comes to structure and kinematics, however the physical and thermal properties some of the nearby smaller cores are also analyzed. Figures 2.1 and 2.2 display the continuum emission maps of all eight sources. Most targets present clumpy structures with multiple cores, while G34.43 and G37.55 are solitary sources.

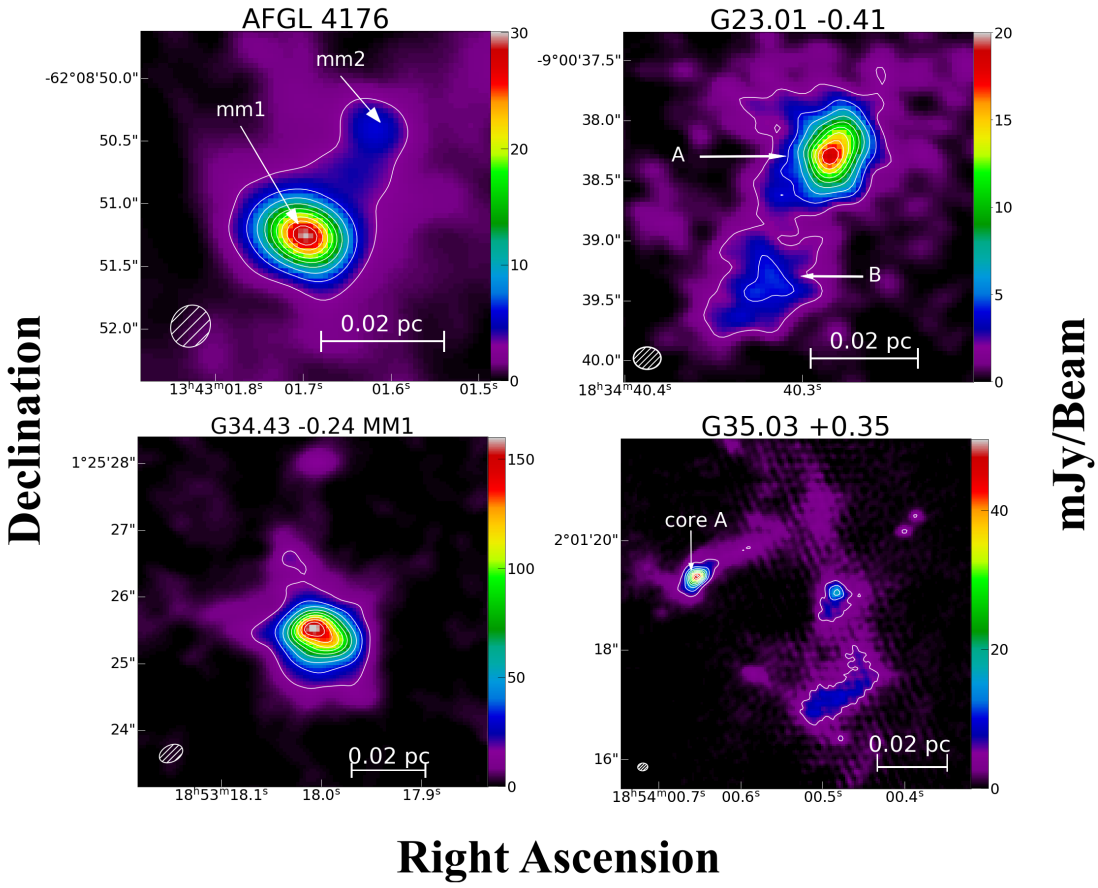

Figure 2.1: Maps of continuum emissions of the first four selected sources, at 1.21 mm, 1.38 mm, 1.32 mm and 1.33 mm for AFGL, G23, G24 and G29, respectively. White contours represent 10, 20,...90% contours of peak emission. Beam size and distance scale provided.

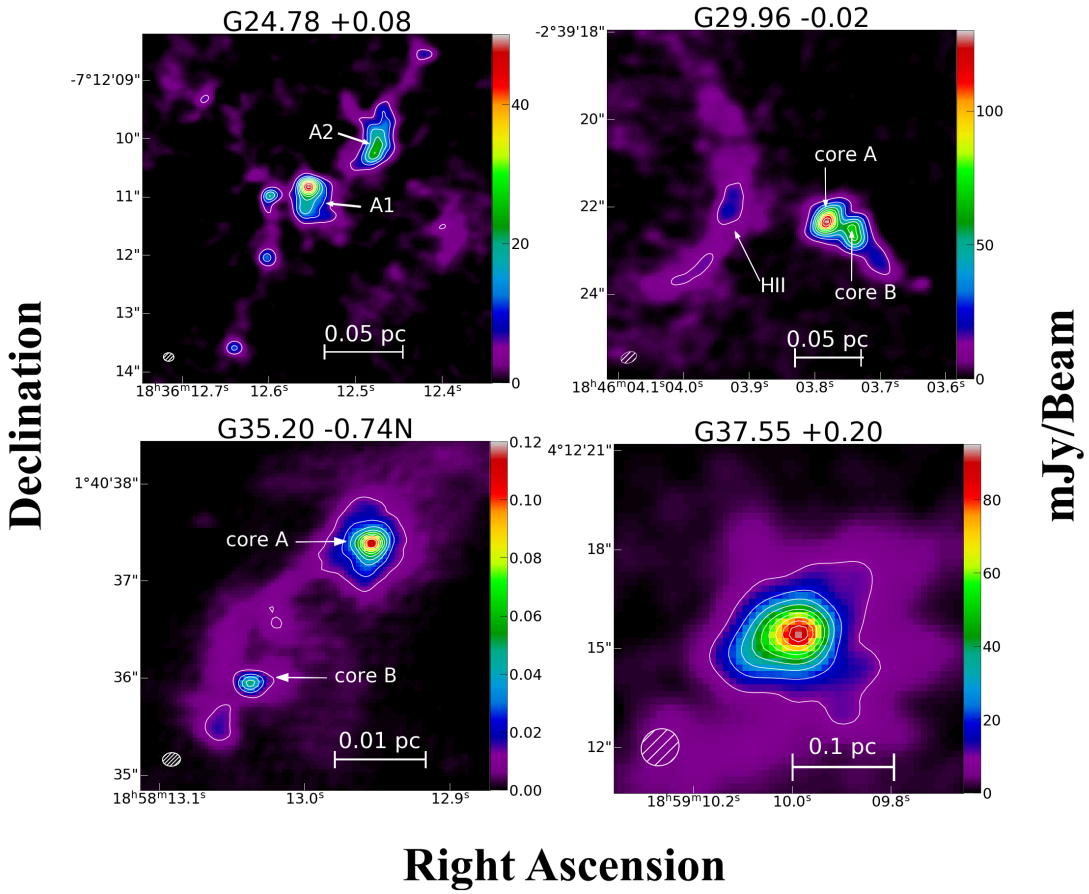

Figure 2.2: Maps of continuum emissions of the final four selected sources, at 1.33 mm, 0.88 mm, 0.88 mm and 2.90 mm for G34, G35.03, G35.20, and G37.55, respectively. Contours same as in figure 2.1

2.2 Spectral Analysis of CH_3CN

To best understand the kinematics and properties of disks around high-mass stars, one must probe the densest and hottest gas, close to the central core. The ALMA archive data can provide an abundance of spectra, encompassing emission lines of many different molecules that probe many different environments. However, the core of this study will focus on analyzing the spectra of CH_3CN lines. CH_3CN has been a proven tracer of hot, dense gas in previous studies of circumstellar disks around B-type protostars (e.g. Cesaroni *et al.,* 2007) and O-type protostars (e.g. Cesaroni *et al.,* 2017).

In this thesis, a selection of targets with previously observed CH_3CN spectra is used to estimate physical and thermal properties, as well as analyzing dynamical structure and kinematics. Several different sets of CH_3CN transitions were used, depending on the data available from the ALMA archive. Table 2.2 provides an overview of the spectroscopic properties of each of the CH_3CN emission lines

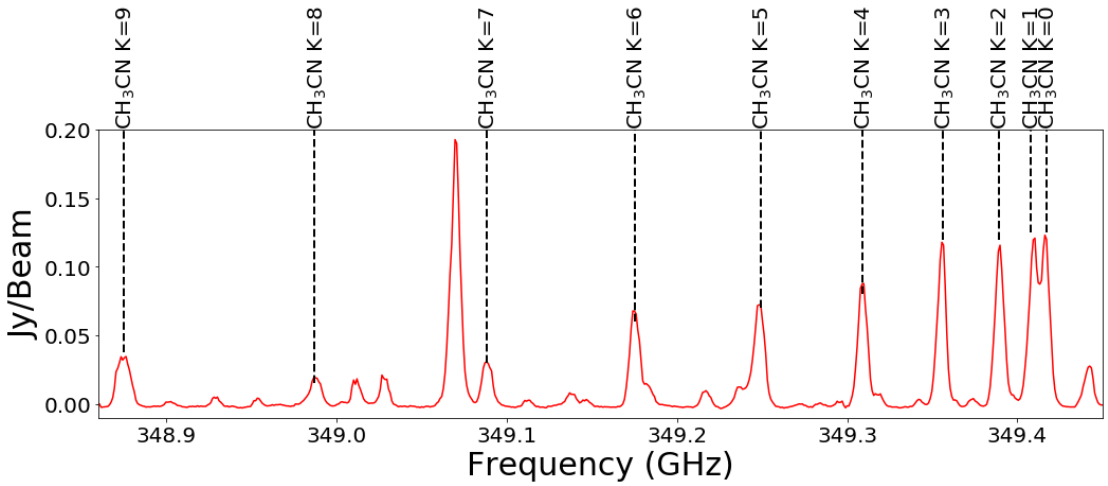

Figure 2.3: An example of CH_3CN K-ladder spectrum; for the source G35.20 -0.74N for transition J=19-18.

used in this study, obtained from the Leiden Atomic and Molecular Database[2] (LAMDA, Schöier *et al.,* 2005). Properties include the J transition, K-level, frequency, Einstein coefficient (A_{ij}), upper state energy level (E_{up}), upper state degeneracy statistical weight (g_{up}) and critical density (n_{crit}) at 100 K. The critical density is given by A_{ij}/C_{ij}, where C_{ij} is the collisional coefficient in cm^3s^{-1}. The higher J-transitions presented in Table 2.2 reach a cap of K=8 or 9, as no levels were used beyond this K-level in the data sets, either due to poor signal-to-noise levels or lack of detection. Figure 2.3 displays an example of a CH_3CN K-ladder, transition J=19-18, K=0-9, for the source G35.20 -0.74N.

2.3 Kinematic Analysis of Disks

2.3.1 Moment Maps

A key component of this thesis is the investigation of disk structure and kinematics. An integral source of information on disk dynamics is found through moment maps. The general mathematical definition of moments is given by equation 2.1, based on the relevant variables to astronomy, velocity and intensity.

$$M_n = \int_{-\infty}^{\infty} V^n I(V) dV \tag{2.1}$$

While several orders of moment maps (n) can be created, publications commonly study Moments 0,1 and 2. In this study we will focus on Moment 0 and 1 maps. Moment 0 maps are integrated intensity maps, averaging the emission over a given set of channels (eq. 2.2).

$$M_0 = \int I(V) dV \tag{2.2}$$

[2]https://home.strw.leidenuniv.nl/~moldata/

Table 2.2: Spectroscopic values of CH_3CN from LAMDA

Transition		Frequency	A_{ij}	E_{up}	g_{up}	n_{crit}
J'→J"	K	(GHz)	(s^{-1})	(K)		(cm^{-3})
6-5	0	110.38350	$1.10x10^{-4}$	18.5	26	$5.5x10^{5}$
6-5	1	110.38138	$9.20x10^{-5}$	25.7	26	$4.7x10^{5}$
6-5	2	110.37499	$9.20x10^{-5}$	47.1	26	$4.9x10^{5}$
6-5	3	110.36434	$7.36x10^{-5}$	82.8	52	$4.0x10^{5}$
6-5	4	110.34944	$5.52x10^{-5}$	132.8	26	$3.1x10^{5}$
6-5	5	110.33028	$1.84x10^{-5}$	197.1	26	$1.1x10^{5}$
12-11	0	220.74727	$9.19x10^{-4}$	68.9	50	$4.7x10^{6}$
12-11	1	220.74301	$8.42x10^{-4}$	76.0	50	$4.1x10^{6}$
12-11	2	220.73024	$8.42x10^{-4}$	97.4	50	$4.2x10^{6}$
12-11	3	220.70895	$8.42x10^{-4}$	133.2	100	$4.3x10^{6}$
12-11	4	220.67914	$7.65x10^{-4}$	183.2	50	$4.0x10^{6}$
12-11	5	220.64082	$6.88x10^{-4}$	247.4	50	$3.6x10^{6}$
12-11	6	220.59399	$6.87x10^{-4}$	325.9	100	$3.7x10^{6}$
12-11	7	220.53864	$5.34x10^{-4}$	418.6	50	$2.9x10^{6}$
12-11	8	220.47477	$4.58x10^{-4}$	525.6	50	$2.5x10^{6}$
12-11	9	220.40238	$3.81x10^{-4}$	646.7	100	$2.1x10^{6}$
13-12	0	239.13793	$1.17x10^{-3}$	80.3	54	$5.7x10^{6}$
13-12	1	239.13331	$1.08x10^{-3}$	87.5	54	$5.3x10^{6}$
13-12	2	239.11948	$1.08x10^{-3}$	108.9	54	$5.4x10^{6}$
13-12	3	239.09641	$1.08x10^{-3}$	144.6	108	$5.5x10^{6}$
13-12	4	239.06412	$9.91x10^{-4}$	194.6	54	$5.1x10^{6}$
13-12	5	239.02261	$9.90x10^{-4}$	258.9	54	$5.2x10^{6}$
13-12	6	238.97187	$8.99x10^{-4}$	337.4	108	$4.8x10^{6}$
13-12	7	238.91190	$8.09x10^{-4}$	430.1	54	$4.3x10^{6}$
13-12	8	238.84271	$7.18x10^{-4}$	537.0	54	$3.9x10^{6}$
13-12	9	238.76430	$5.38x10^{-4}$	658.2	108	$3.0x10^{6}$
19-18	0	349.45372	$3.70x10^{-3}$	167.7	78	$1.8x10^{7}$
19-18	1	349.44697	$3.50x10^{-3}$	174.9	78	$1.7x10^{7}$
19-18	2	349.42675	$3.50x10^{-3}$	196.3	78	$1.7x10^{7}$
19-18	3	349.39304	$3.50x10^{-3}$	232.0	156	$1.7x10^{7}$
19-18	4	349.34585	$3.50x10^{-3}$	282.0	78	$1.7x10^{7}$
19-18	5	349.28518	$3.31x10^{-3}$	346.2	78	$1.7x10^{7}$
19-18	6	349.21102	$3.30x10^{-3}$	424.7	156	$1.7x10^{7}$
19-18	7	349.12338	$3.11x10^{-3}$	517.4	78	$1.6x10^{7}$
19-18	8	349.02225	$2.91x10^{-3}$	624.3	78	$1.5x10^{7}$
19-18	9	348.90765	$2.71x10^{-3}$	745.4	156	$1.4x10^{7}$

Here I(V) is the emission line flux density in Jy/beam, and dV is the velocity channel width in km/s. Moment 0 maps depict the overall gas distribution of a source by displaying emission intensities.

Moment 1 maps are the intensity-weighted velocity maps (eq.2.3).

$$M_1 = \frac{\int I(V) V dV}{\int I(V) dV} \tag{2.3}$$

First moment maps provide a gas velocity field, which is used to interpret the movement of the gas. A velocity gradient across a Moment 1 map can be an indication that the gas is in rotation, as is observed in Keplerian disks around low-mass stars. In this thesis, moment maps were produced via CASA[3] (McMullin *et al.,* 2007), version 5.6.0, using the *immoments* command. 3σ noise is removed, and by selecting the appropriate channels/frequency range, a Gaussian fit is made with each K emission line to produce the moment maps. From these moment maps, intensities and velocities are obtained for further analysis.

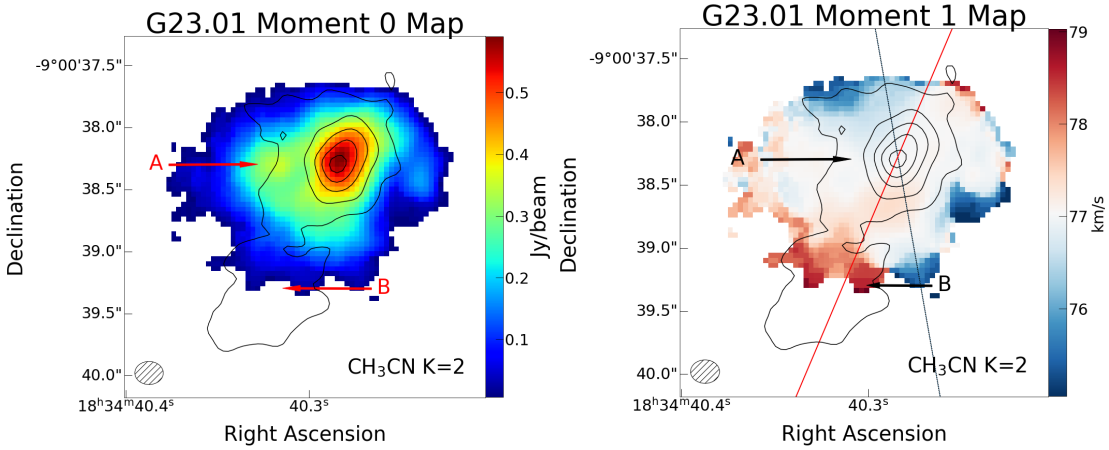

Figure 2.4: An example of Moment 0 (*left*) and Moment 1 maps (*right*) of source G23.01, CH_3CN(12-11) K=2 line. Contours represent 10, 30..,90% peak continuum flux emission. Black line velocity gradient position angle used for position-velocity diagrams. Red line indicates molecular outflow direction determined by Sanna *et al.,* 2019.

2.3.2 Position-Velocity Diagrams

Another useful tool in analyzing disk kinematics is position-velocity (PV) diagrams. PV cuts are made through the data cube, at position angles that follow the velocity gradient determined in Moment 1 maps. The resulting diagram is the gas velocity as a function of the offset from the central position (see Figure 2.5 for example). If the gas is in Keplerian rotation, the resulting diagram will produce a "butterfly pattern", or more specifically, trace Kepler's third law (eq. 2.4):

$$\Delta V = sin(i)\sqrt{\frac{GM_*}{R}} \tag{2.4}$$

[3]Common Astronomy Software Applications is available from http://casa.nrao.edu/

Here ΔV is the velocity, i is the inclination, G is the gravitational constant, M_* is the mass of the star, and R the radius of the disk. Inclination plays a key role in the observed masses and velocities. Thus, in this thesis, inclinations found from literature are preferred. If no inclination value is found, an inclination factor is derived from the major (θ_{major}) and minor axis (θ_{minor}) of the disk, with the assumption that the disk is a thin, circular morphology.

$$i = cos^{-1}\left(\frac{\theta_{minor}}{\theta_{major}}\right) \tag{2.5}$$

A low K-line is preferred for analysis of PV plots, as they often present strong emission. In our sources, K-lines 0 and 1 were often blended together (see Section A.9 for spectral windows), thus K=2 is used for moment maps and PV plot analysis (with the exception of AFGL 4176; see Section 3.8 for more details). The PV plots were produced with the *impv* command in CASA.

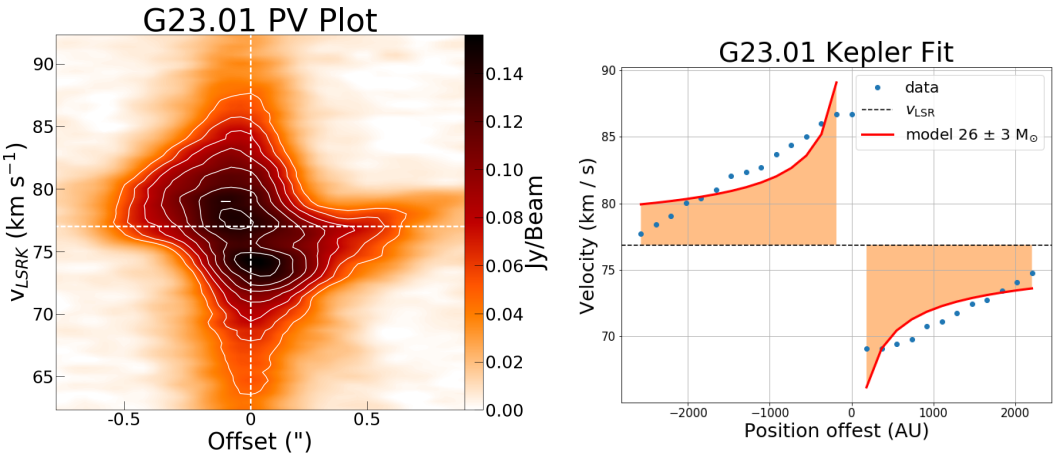

Figure 2.5: *Left*: Example of Position-velocity diagram for G23.01, for CH_3CN K 2 line. The cut is made through the continuum peak, along a position angle of 10° W of N. Contours represent 20, 30,..., 90% of peak emission. *Right*: Example of Kepler fit using Seifried *et al.,* 2016 method (see Section 2.4.4). Blue dots represent data points, while red curve indicates the Kepler fit.

2.3.3 Temperature and Velocity Gradient Profiles

The structure of the disk can be inferred by the temperature gradient as a function of radius. For a geometrically thin disk, assuming heat is dissipated as thermal radiation from both the top and bottom of the disk, Pringle, 1981 stated the temperature profile of an accretion disk is given by the following:

$$\sigma T^4 = \frac{3\dot{M}}{8\pi R^2}\frac{GM}{R}\left[1 - (\frac{R_i}{R})^{1/2}\right] \tag{2.6}$$

where σ is the Stefan-Boltzmann constant, $\dot{M}$ is the accretion rate and r_i the inner radius of the disk. Assuming $r > r_i$, the temperature of a steady-state accreting disk, such as those found around high-mass stars, follows the approximate

temperature-radius relation:

$$T \propto R^{-3/4} \tag{2.7}$$

Kenyon *et al.,* 1987 expanded on this, stating that disk curvature plays an important role in the temperature profile, particularly at larger radii. They deduced that a disk with flared edges will produce a temperature profile of

$$T \propto R^{-1/2} \tag{2.8}$$

Many other factors can come into play when determining temperature profiles. Ahmadi *et al.,* 2018 found that positive slopes are even possible, if the source is experiencing external heating. That being said, equation 2.7 and 2.8 are the benchmarks that will be used for comparison to our results of temperature gradients[4].

The dynamics of the structure is further probed to determine if the disk is experiencing rotation, specifically Keplerian rotation. In this case, an assumption is made that the disk is in Kepler rotation, and another simple temperature-radius profile is constructed from Kepler's third law (eq. 2.4). Gas in Keplerian rotation around a disk at radius R produces line emissions at a maximal velocity from the rest frequency (ΔV). This velocity is measured from the line widths of each K-ladder emission line detected, and a radius is determined from Kepler's third law. Since each K-transition has a correlated upper energy level temperature, a temperature is associated to each measured line width, and a temperature vs radius profile is determined. Line widths are measured from the CH_3CN emission lines, using CASA's *specfit* command. This profile is compared to the temperature gradient profile produced from temperature measurements. A disk in Keplerian rotation will theoretically produce a slope in agreement with the temperature gradient profile results. If the slopes do not agree, it is likely that the assumption of Keplerian rotation is invalid.

Another simple relation constructed is velocity gradients as a function of radius. Velocity gradients are determined by measuring the change in velocity across the Moment 1 maps across the position angle, along with the associated gradient length. Each K-line produces a moment map with its own velocity gradient. Based on the K-line upper level energy, this moment map will traces a different region of the core; higher K-lines trace small, central, hot regions, and lower K-lines trace broad, cool regions. The upper level energy temperature is converted to a radius from the temperature-radius profiles, and plotted against the respective derived velocity gradient. A disk in Keplerian rotation is expected to have the hottest gas closest to the central core, as well as the highest velocity, due to differential rotation. As a result, higher velocity gradients are expected to be measured in the hottest K-lines for a disk in Keplerian rotation.

[4]Temperature measurement methodology is explained Section 2.4

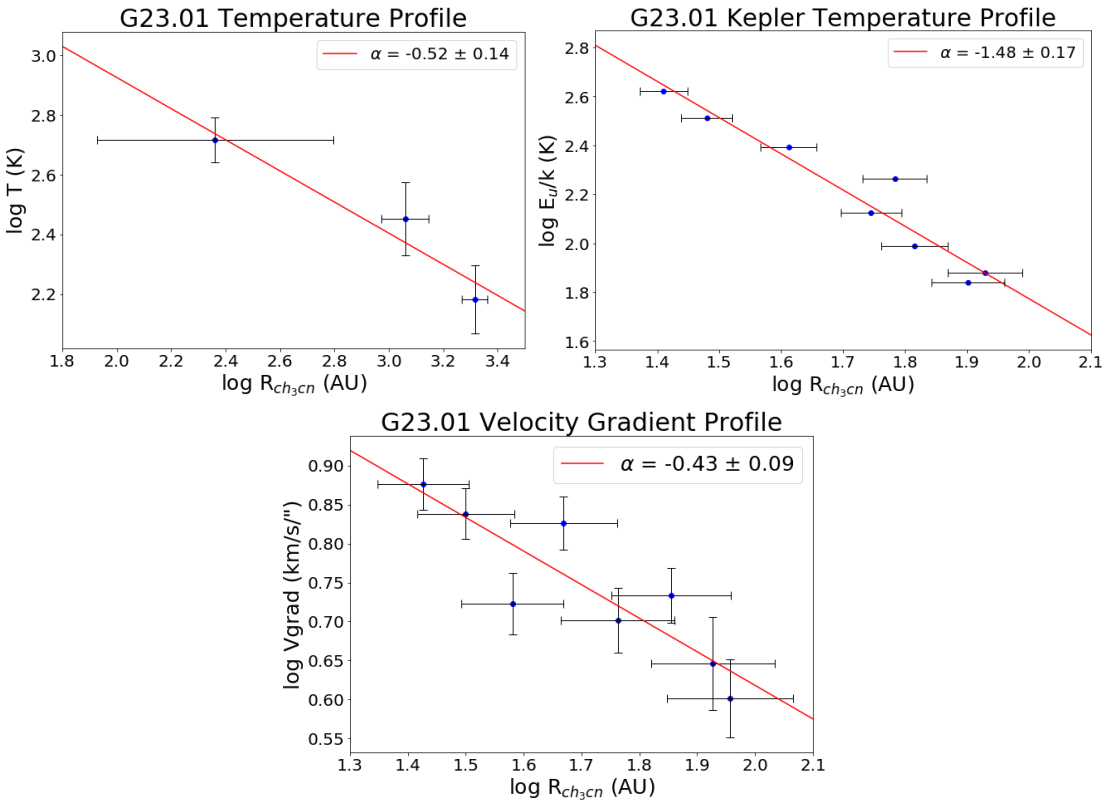

Figure 2.6: *Top Left*: Example of Temperature vs Radius profile of G23.01 from temperature gradient. Error bars are based on radius and temperature measurement uncertainties *Top Right*: Temperature profile of G23.01 determined from line widths, assuming Kepler rotation. Errors are based on velocity line width uncertainties *Bottom:* Velocity gradient profile of G23.01. Velocity gradient errors are based on velocity resolution, while radius errors are based on the beam size.

2.4 Physical & Thermal Properties of Disks

Along with disk structure and dynamics, we also determine physical and thermal properties of the protostars and surrounding structures. Thanks to the high resolution of ALMA data, this thesis will provide in-depth analysis of these properties as a function of position, and distribution plots will be produced. This is accomplished via placing a grid over each target. Properties such as kinetic temperature, column density, volume density and abundances are then obtained for each grid point. These values are compared within the sample and to those in literature, to determine if there are any noticeable trends, and to classify the structures surrounding the protostars. Two core analysis methods were used, one assuming local thermodynamic equilibrium (LTE), using population diagrams and the other assuming non-LTE conditions.

2.4.1 LTE Analysis: Population Diagrams

Population diagrams are a powerful tool in determining physical properties of a molecular species, in particular column densities and excitation temperatures. Developed by Goldsmith *et al.,* 1999, population diagrams are based on rotation diagrams. Linke *et al.,* 1979 first used rotation diagrams as a method of determining gas properties, but they were brought into popularity by the extensive use of Turner, 1991. Rotation diagrams assume level populations of a molecule are in local thermodynamic equilibrium (LTE) at a single excitation temperature (T_{ex}).

$$ln\left(\frac{\gamma_u W}{g_u}\right) = ln\left(\frac{N}{Z(T_{ex})}\right) - \frac{E_u}{kT_{ex}} \tag{2.9}$$

where γ_u is a combination of constants consisting of Boltzmann (k), Planck (h) and speed of light (c) constants, along with frequency (ν) and corresponding Einstein coefficient (A) of transition i $\rightarrow$ j. W is the measured integrated line intensity, and g_u is the upper state degeneracy.

$$\gamma_u = \frac{8\pi k\nu_{ij}^2}{hc^3 A_{ij}} \tag{2.10}$$

The combination of γ_uW is the upper state column density (N_u) of a transition in cm^{-2}, while N is the total column density of the molecule over all states. E_u is the upper state energy in K, and Z is the rotational partition function. For a symmetric top molecule such as CH_3CN, the partition function is given by equation 2.11(Gibb *et al.,* 2000), where A,B and C are the rotational constants.

$$Z(T_{ex}) = \sqrt{\frac{\pi}{ABC}\left(\frac{kT_{ex}}{h}\right)^3} \tag{2.11}$$

From the integrated intensity measurements, the upper state column density is calculated and plotted as a function of upper state energies, E_u. From this diagram the excitation temperature is obtained from the inverse of the slope of a least-square fit line. With the derived rotational temperature, the partition function is computed. Finally, a total column density is obtained from the y-intercept of the linear fit.

Population diagrams expand on rotation diagrams by including factors for line opacity and beam dilution. If a source is optically thick, its measured intensity is reduced by a factor related to photon escape probability (eq. 2.12). Adding the factor C_τ will correct for any optical depth alterations.

$$C_\tau = \frac{\tau}{1 - e^{-\tau}} \tag{2.12}$$

The optical depth of transition j$\rightarrow$j-1, is determined via equation 2.13;

$$\tau_{j,j-1} = \frac{8\pi^3\mu^2}{3h^2}\frac{N}{\Delta V}\frac{1}{Z} j e^{-aj(j+1)}(e^{2aj} - 1) \tag{2.13}$$

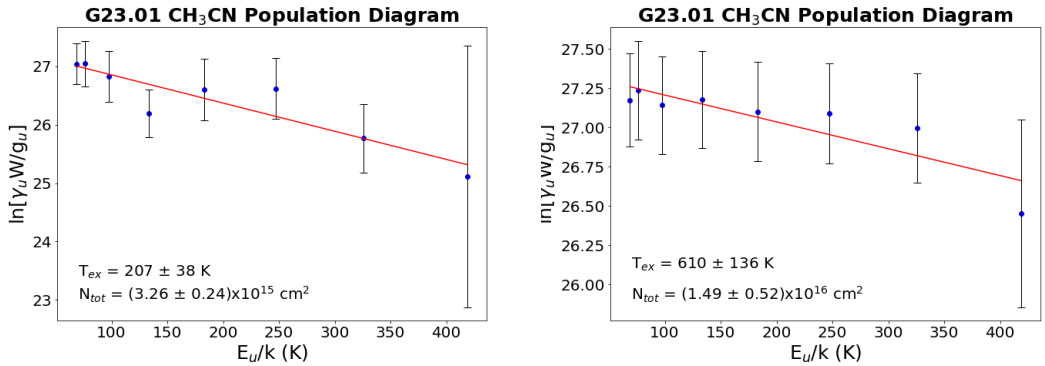

Figure 2.7: Examples of population diagrams produce for the source G23.01 -0.41, including the central hot zone (right figure). Error bars are determined from 3σ noise levels. Errors in T_{ex} and N_{tot} are based on the linear fit.

where ΔV is the line width, and $a = hB/kT$. Finally, a beam dilution factor is included, to take into account if a object does not completely fill the beam. The relation for population diagrams now the following:

$$ln\left(\frac{\gamma_u W}{g_u}\right) + ln(C_\tau) + ln\left(\frac{\Delta\Omega_a}{\Delta\Omega_s}\right) = ln\left(\frac{N}{Z(T_{ex})}\right) - \frac{E_u}{kT_{ex}} \tag{2.14}$$

$\Delta\Omega_a$ is the solid angle of the antenna beam, while $\Delta\Omega_s$ is the solid angle of the source. From here the same methodology is followed as rotation diagrams, to obtain excitation temperatures and column densities. Figure 2.7 includes two examples of population diagrams produced for the source G23.01 -0.41. Errors are based on flux errors and the linear fit.

While population diagrams represent a powerful tool for obtaining temperatures and column densities, there are some drawbacks. First, they are based on the assumption of LTE. This is reasonable in high density regions, but not so in less dense, tumultuous regions. Also, they assume a single excitation temperature for each K-transition, when in reality each transition has its own excitation temperature. Furthermore, lower K transitions can have higher opacities, leading to a flattening of slopes in the diagrams. This results in over-estimated temperatures, and under-estimated column densities. The inclusion of multiple J-transitions helps constrain these effects, particularly isotopologues of CH_3CN, which inhibit optical depth variations. However, in this thesis a second method of non-LTE modelling was used to determine physical and thermal quantities of the circumstellar disks.

2.4.2 Non-LTE Analysis: RADEX

RADEX[5] (van der Tak *et al.,* 2007) is a computer program that calculates intensities of atomic and molecular lines and estimates physical, thermal and chemical properties such as temperatures, volume density and column density. The code uses statistical equilibrium calculations based on collisional and radiative

[5]RADEX is available online from https://home.strw.leidenuniv.nl/~moldata/radex.html

processes, assuming a homogeneous medium. Optical depth is treated via escape probability method, and collisional data (Green, 1986) is obtained from the LAMDA database.

Using this code, a grid in parameter space is created over three parameters: kinetic temperature, CH_3CN column density, and H_2 volume density. The grid span is based on the population diagram results, but in general are given around the following ranges: T from 20 - 600 K, column density from 10^{13}-10^{17} cm^{-2}, and H_2 volume density from 10^4-10^8 cm^{-3}. These values encompass CH_3CN property ranges predicted (i.e Garrod *et al.,* 2017) and observed around high-mass protostars (i.e. Bell *et al.,* 2014, Bøgelund *et al.,* 2019). Other factors taken into account include frequency range, i.e. which CH_3CN transitions are being measured, line widths, background temperature (assumed to be 2.73 K for black-body radiation of cosmic microwave background), and collisional partners. In this case we assume only one partner with CH_3CN, that being H_2. Approximately 25 grid points are selected per parameter, creating a 25x25x25 grid of approximately 15,000 points. For each point, RADEX produces modelled intensities of each CH_3CN emission line. The modelled intensities are then compared to the measured intensities found via CASA Moment 0 maps. The best-fit parameters are determined by performing a χ^2 minimization over the grid.

$$\chi^2 = \frac{1}{\#_{obs} - \#_{par}} \sum \left[\frac{I_{obs} - I_{mod}}{\sigma_{obs}} \right]^2 \tag{2.15}$$

Here $\#_{obs}$ is the number of observed lines, $\#_{par}$ is the number of free parameters in the model (in this case three: temperature, column density and volume density), I_{obs} and I_{mod} are the observed and modelled intensities, respectively, and σ_{obs} is the 1σ uncertainty on the observed intensity. This uncertainty is given by the root-mean squared value (RMS) provided in CASA added in quadrature with 10 % of the measured flux intensity (eq. 2.16).

$$\sigma_{obs} = \sqrt{(RMS)^2 + (0.1 * I_{obs})^2} \tag{2.16}$$

The resulting best-fit parameters is then compared to those of the population diagrams. While RADEX does not suffer from the drawbacks of population diagrams, it is limited by the data provided to it. More specifically, the CH_3CN data cannot provide information above 600 K in combination with scenarios at the high ends of our volume and column density ranges. Non-LTE modelling uncertainties are difficult to quantify. The collisional data of CH_3CN in LAMDA was originally determined by Green, 1986, therefore we will use the uncertainties provided in this paper. Green, 1986 state uncertainties of the order of 50% up to a factor of two. Overall, it is beneficial to use both population diagrams and RADEX grids to compare source properties and minimize bias. Population diagrams represent LTE cases and will henceforth labelled as such, while similarly RADEX represents a non-LTE approach and is referred to as non-LTE analysis.

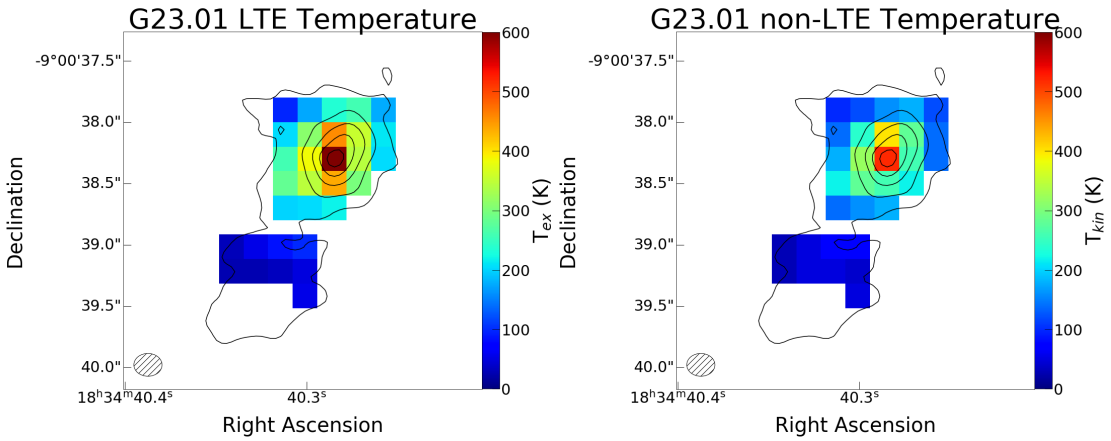

Figure 2.8: *Left*: Temperature map of G23.01 LTE analysis via population diagrams. *Right*: Temperature map of G23.01 non-LTE analysis via RADEX grids.

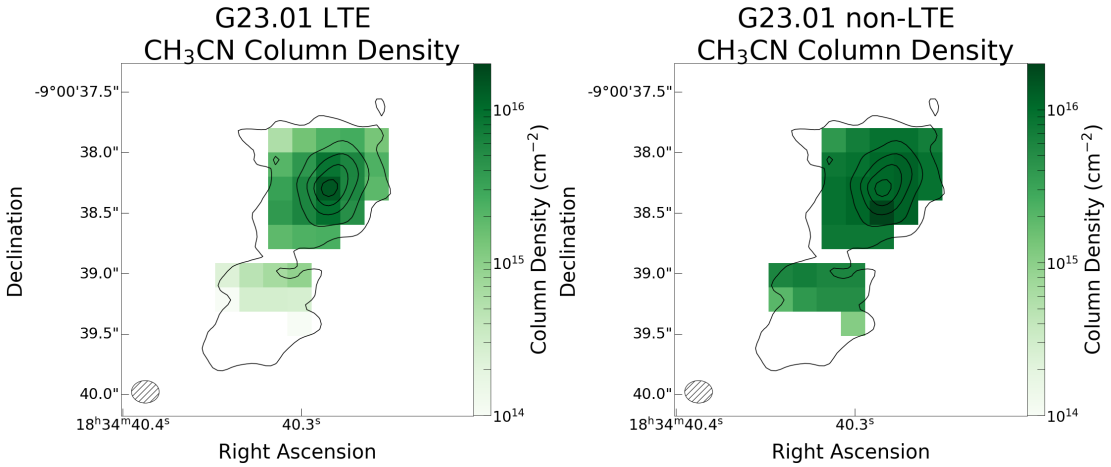

Figure 2.9: *Left*: CH_3CN column density map of G23.01 LTE analysis via population diagrams. *Right*: CH_3CN column density map of G23.01 non-LTE analysis via RADEX grids.

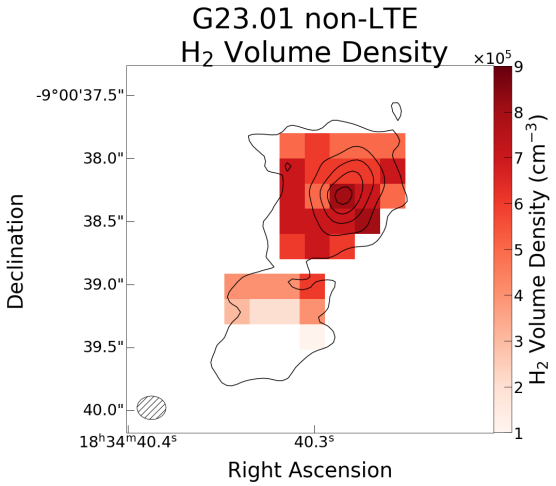

Figure 2.10: H_2 volume density of G23.01, determined through Non-LTE RADEX analysis.

2.4.3 Continuum Data

While the bulk of this thesis used CH_3CN, continuum data was also used for additional analysis. Column densities of H_2 gas for each data point are determined via the dust continuum equation 2.17.

$$N_{H_2} = \frac{100 * I_v}{\Omega_{beam} * \mu_{H_2} * m_H * \kappa_v * B_v(T)} \tag{2.17}$$

I_v is the measured continuum intensity, Ω_{beam} is the beam solid angle, μ_{H_2} is the mean molecular mass of H_2 equaling 2.33, m_H is the mass of the hydrogen atom, κ_v is the opacity and $B_v(T)$ is the Planck function. The factor of 100 represents the gas-to-dust ratio. The opacity factor is dependent on frequency, determined by Ossenkopf *et al.*, 1994. For our sample, we assume the dust temperatures needed for the Planck function follow the temperatures determined by the CH_3CN analysis. Since two temperature profiles are determined (LTE and non-LTE), two H_2 column density distributions are formed. However, the difference between the two scenarios is minimal. Both versions of the plots are shown in the Appendix, but only one will be discussed per source, unless significant variations exist.

With hydrogen column densities determined, relative abundance profiles of CH_3CN/H_2 are made for each of our data points as well.

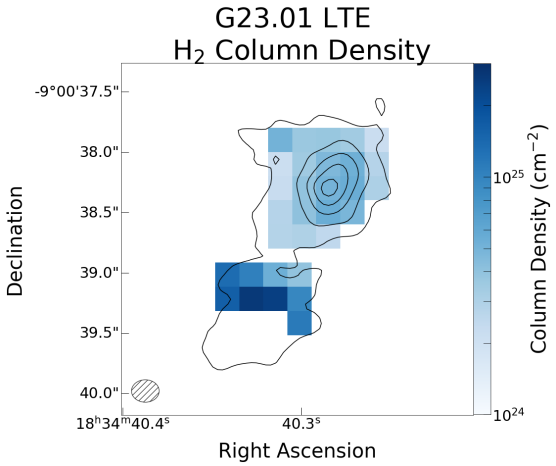

Figure 2.11: :*Left*: H_2 column density map of G23.01.

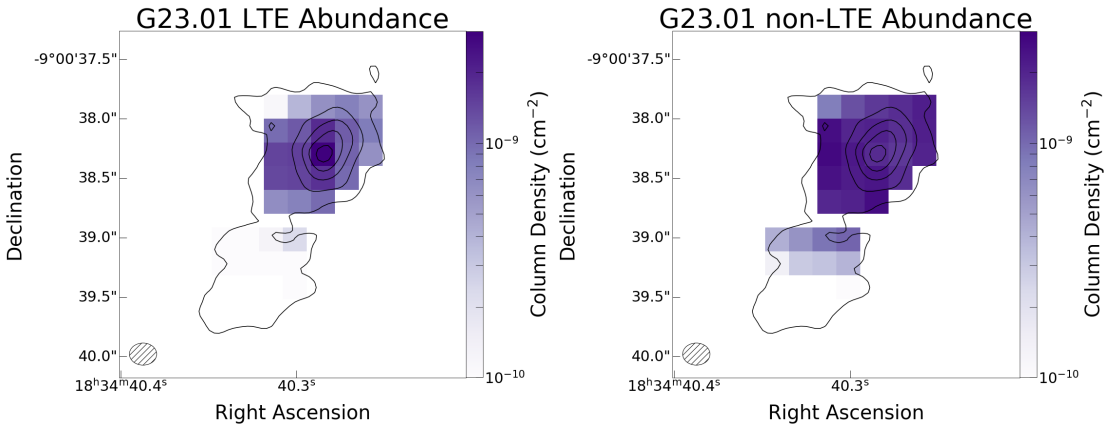

Figure 2.12: *Left*: Abundance map of G23.01 CH_3CN LTE analysis. *Right*: Abundance map of G23.01 CH_3CN non-LTE analysis.

Disk Mass

Continuum data were also used to determine disk masses. The masses were derived using equation 2.18.

$$M_d = \frac{D^2 S_v}{\kappa_v B_v(T_d)} \tag{2.18}$$

Where M_d is the dust mass, D is the distance to the source, S_v is the flux density, κ_v is the dust opacity, and $B_v(T_d)$ is the Planck function at temperature T_d. The temperatures, gas-to-dust ratios and opacities are the same as discussed for the H_2 column densities.

2.4.4 Stellar Mass

Central stellar masses were determined via two methods; from a luminosity-mass relation and from the dynamical mass.

Stellar masses are produced via the luminosity-mass relationship of Vitrichenko *et al.,* 2007 (eq. 2.19), determined from taking a linear fit of a population of 10-50 $M_\odot$ stars. Luminosities of our population were either adopted from the RMS database or from literature (see Table 3.4 for specific references). In some cases, the luminosity encompassed a HSFMR containing multiple protostars. Thus, the luminosity and stellar mass is the combination of all sources within the region. This is such a case for G24.78, G29.96 (where a significant portion is represent by the neighbouring HII cloud), G35.03 and G35.20. For these cases the derived mass can only be assumed to be an upper limit.

$$\frac{L}{L_\odot} \approx 19 \left(\frac{M}{M_\odot}\right)^{2.76} \tag{2.19}$$

Stellar masses are also determined from a fit of Kepler's third law via PV diagram. This is done through the method developed by Seifried *et al.,* 2016. Known as the Seifried method, the first step is to determine the two main quadrants, i.e. the quadrants with the most emission, either the upper left and lower right, or vice versa. Then a certain threshold for emission is selected; 5σ is commonly cited (i.e. Ahmadi *et al.,* 2018), and is the value adopted for this thesis. Starting with the central offset location, a data point is placed at the highest velocity pixel exceeding this threshold. The methodology is repeated as you move outwards from the central position, creating the upper edge of the PV plot. The same technique is done for the lower quadrant, but using the lowest velocity pixel. These outer edge points are then fitted to Kepler's third law to determine the central mass. For this method the *KeplerFit* code was used, described by Bosco *et al.,* 2019[6]. An example of this fitting can be see in Figure 2.5 for source G23.01.

2.4.5 Toomre Stability

The stability of a disk in rotation is directly related between the disk and stellar mass, and is determined via the Toomre Q parameter. Originally quantified by Toomre, 1964 for disks of galaxies, the physics is applicable in many scenarios, including the circumstellar disks in this thesis. The outward forces and gas pressure of a rotating disk can provide stability against gravitational collapse, and this stability is quantified by the Toomre Q parameter (eq 2.20).

$$Q = \frac{c_s \Omega}{\pi G \Sigma} \tag{2.20}$$

Here c_s is the speed of sound, Ω is the angular velocity of the disk, and Σ is the surface density. The speed of sound is a function of temperature (eq 2.21), where γ is the adiabatic index, equal to 5/3. The temperatures again are adopted from CH_3CN temperatures.

$$c_s = \sqrt{\frac{\gamma k_B T}{\mu_{H_2} m_H}} \tag{2.21}$$

[6]KeplerFit is available at https://github.com/felixbosco/KeplerFit

The angular velocity is given by,

$$\Omega(r) = \sqrt{\frac{G(M_\star + M_{disk}(r))}{r^3}} \tag{2.22}$$

Where $M_\star$ is the central stellar mass, and M_{disk} is the disk mass within radius, r. Finally, the surface density is a function of H_2 column density and the mean molecular mass of hydrogen:

$$\Sigma = N_{H_2} * \mu_{H_2} * m_H \tag{2.23}$$

If the Toomre Q parameter is below 1, a thin disk is considered unstable against gravitational instabilities.

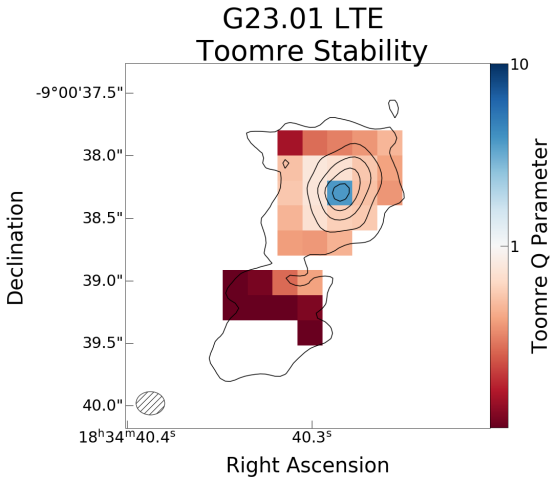

Figure 2.13: Toomre Q stability plot of G23.01. Values <1 indicate instability against asymmetric gravitational instabilities.

2.5 Comparison to Chemical Models

Many chemical models have been constructed to predict and explain observed abundances of molecular species (Garrod, 2013, Viti *et al.,* 1999). In this thesis, an elementary comparison of measured CH_3CN abundances are compared to two chemical models, constructed by Allen *et al.,* 2017 and Garrod *et al.,* 2017. Both models are based on the work of Garrod *et al.,* 2008. The models are composed of three different warm-up phase timescales; fast, medium and slow, corresponding to approximately 50, 200, and 1000 kyr, respectively. Assuming certain accretion rates, a central mass can be correlated to each formation timescale. The total time to collapse a spherical shell is given by equation 2.24.

$$t_c = t_{exp} + t_{ff} = \int_0^r \frac{dx}{\sigma(x)} + \left\{ \frac{3\pi}{32G < \rho_0(r) >} \right\}^{\frac{1}{2}} \tag{2.24}$$

Here the collapse time is the sum of the expansion time (t_{exp}) and free fall-time (t_{ff}). $\sigma(x)$ is the velocity dispersion and $< \rho_0(r) >$ the mean density. Thus a more

massive core with greater density will collapse more quickly, and have a shorter warm-up phase. As described by Allen *et al.,* 2017 an accretion rate of 10^{-4} to 10^{-5} $M_{\odot}yr^{-1}$ will correspond to a mass of 60, 15 and 6 $M_{\odot}$ for a fast, medium and slow warm-up time, respectively. This is based on the work of Bernasconi *et al.,* 1996, who modelled contraction and formation timescales of stars up to 120 $M_{\odot}$ via accretion. However, episodic accretion has been observed to reach as high as 10^{-3} $M_{\odot}yr^{-1}$ (Tan *et al.,* 2014). Higher accretion rates increase the outward pressure, thus extending collapse times and corresponding to lower stellar mass values of 8, 4 and 1 $M_{\odot}$ for fast, medium and slow warm-ups, respectively.

For the work by Allen *et al.,* 2017, three different initial H_2 densities are used, 10^7, 10^8, and 10^9 cm^{-3}, that remain constant over the warm-up phase, while the gas and dust temperature increases from 10 - 500 K. The model has enhanced initial conditions of CO and CO_2 (initial condition 5 in Allen *et al.,* 2017). Their focus was on the central cores of HMSFR, however, since this thesis has abundances for a distribution of data points, an average abundance over the entire disk is used for comparison.

Garrod *et al.,* 2017 simulates hot-core chemistry via grain-surface formation for nitriles and alkanes to predict the abundances of carbon-chain molecules in the hot-core of the HMSFR SgrB2(N). The initial conditions differ from the Allen model, as it includes two-phases, an initial free fall collapse, followed by the warm-up phase. Thus, the initial ices are formed in a model dependent manner, while the Allen model used several sets of initial ice abundances. Garrod *et al.,* 2017 assumes a single gas density of $2x10^8$ cm^{-3} and warm-up from 8-400 K. For comparison with this model, an assumption is made that all of our sources are in agreement with this density. The average densities determined in this study are a considered a minimum, and less than this cited value, therefore are acceptable with the Garrod comparison. However, some degree of uncertainty remains. Initial elemental abundances are that of Garrod, 2013. However, both Allen and Garrod determined that initial elemental abundances have minimal effect on the final abundances of more complex species. Figure 2.14 displays an example model of both scenarios for the fast warm-up phase (at 10^8 cm^{-3} for the Allen model, for equal comparison).

We compare our calculated abundances, H_2 densities and central masses to the chemical models, and determine which scenario fits our data best. As all of our sources are intermediate to high-mass (proto)stars, it can be assumed that most likely the fast or medium warm-up phases best fit our data. Many other factors come into play when modelling abundances, including starting temperatures and cosmic-ray ionization rates, however the scope of this thesis focuses on densities and warm-up times.

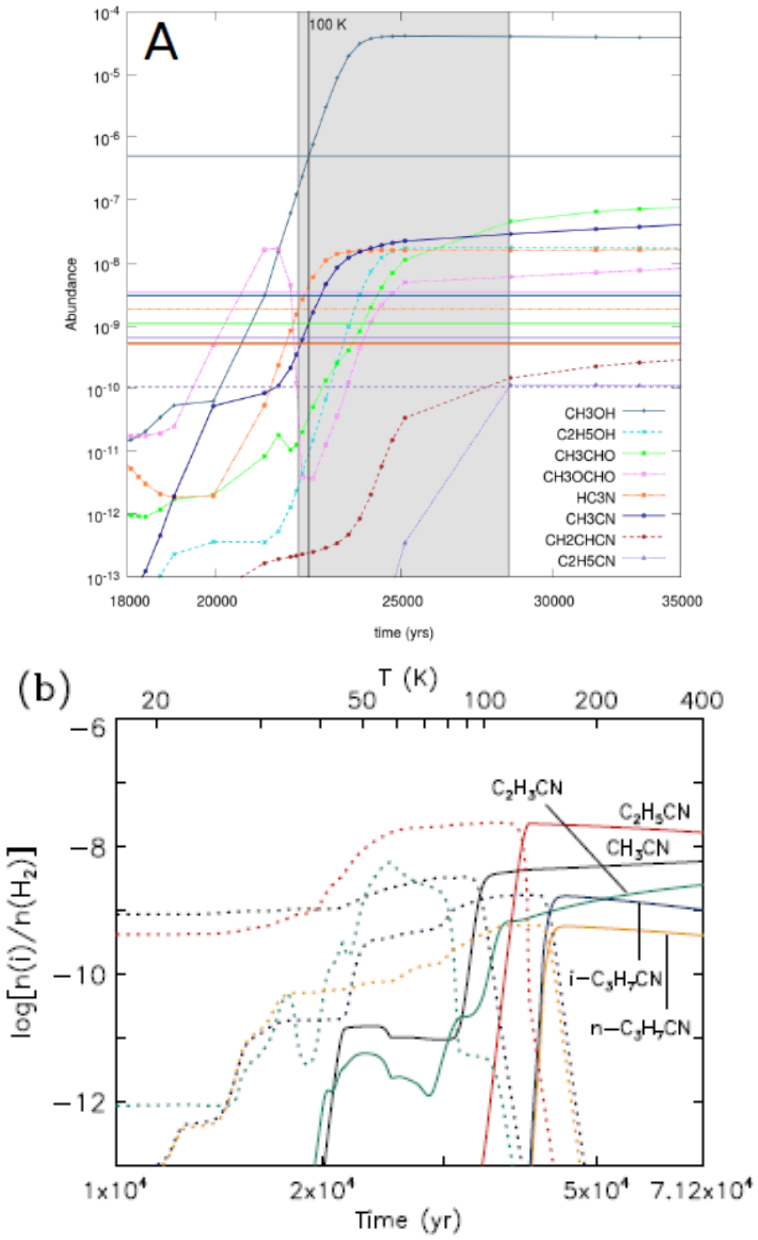

Figure 2.14: *Top*: Example of chemical abundance model of CH_3CN (and other molecules) for fast warm-up phase, from Allen *et al.*, 2017 *Bottom*: Same as left but from Garrod *et al.*, 2017. Solid lines represent gas-phase abundances, while dotted lines represent grain species.

Chapter 3

Results

The following Section is an overview of the results established in this study. The core of results can be viewed at the end of the section in Tables 3.1 (slopes of temperature and velocity gradient profiles), 3.2 (peak physical properties), 3.3 (average physical properties) and 3.4 (mass profile). For consistency, averages were determined for data points at least partially within the outer continuum contour, so not to confuse disk properties with those of the surrounding envelope. The plots of G23.01 were used as examples in the Section 2, while all remaining source plots are located in the Appendix.

3.1 G23.01 -0.41

G023.01-00.41 is a high-mass star forming region that hosts a known high-mass core (Sanna *et al.,* 2019). In the continuum image (Figure 2.1), the hot molecular core is visible as core A. A secondary region is visible to the south of core A, labelled as B.

The Moment maps of G23 (Figure 2.4), illustrate high CH_3CN emission in core A that extends approximately 0.5" into core B in the S direction, where it ceases. The Moment 1 map indicates a velocity gradient across core A at a position angle of 10° W of N, blue-shifting in the NW and red-shifting in the SE.

The temperature analysis (Figure 2.8) illustrates peak temperatures (Table 3.2) at the continuum peak, reaching 610 K (LTE) and 520 K (non-LTE). The temperature gradient decreases to the S, towards the mid-section of B, indicating their is no central source in B. More likely this implies the warmer gas in the N of region B originated from the main core A, and is being expelled outward. In fact, Sanna *et al.,* 2019 state that there is a bipolar outflow of cold gas at position angle 33° (E of N), which matches the direction of the southern core as compared to the northern counterpart.

The temperature gradient constructs a profile of $T \propto R^{-0.52}$ (Figure 2.6), indicating a flared disk structure. When assuming Kepler rotation however, the slope

increases to -1.48 (same figure). This disagreement between α values suggests that the assumption of Keplerian rotation may not be valid for this source.

CH_3CN Column densities (Figure 2.9) peak at the continuum peak for LTE ($1.5\text{x}10^{16}$ cm^{-2}), while peaking 0.2" south for non-LTE conditions ($2.2\text{x}10^{16}$ cm^{-2}). While the peak values are similar, non-LTE analysis has a particularly flat profile, averaging over double the column density of the LTE analysis. However, with errors upwards of 50% in non-LTE and 20-30% in LTE analysis, the differences are only significant on the very edges of the map. It is here that signal-to-noise uncertainties are highest.

While core A has peak H_2 column densities at the continuum peak (Figure 2.11), higher values are found at the southern edge of source B, peaking at $2.6\text{x}10^{25}$ cm^{-2}, almost double the peak values for the main source A. This may indicate a buildup of gas from the outflow or shocks originating from A.

Peak positions and distributions of abundances (Figure 2.12) mirror the CH_3CN column densities, with similar peaks ($3.0\text{x}10^{-9}$) for both LTE and non-LTE methods. The abundances fit the model of a medium warm-up timescale determined by Garrod *et al.,* 2017, where temperatures of 160 K (compared to our averages of 168 and 217 for LTE and non-LTE, respectively) are reached after approximately 190 kyr. Note that the CH_3CN abundances are very low in area B; Far from the heating source, minimal sublimation of grains would occur in this region. The detectable CH_3CN in this region is likely produced from the shock front of the outflow.

The PV plot (Figure 2.5) constructed from the Moment 1 map position angle displays arguably the most noticeable visual representation of a butterfly pattern of the sample, and produces a dynamical mass of 26 $M_\odot$ via the Seifried Method. The luminosity relation produces a smaller mass of 16 $M_\odot$ (Table 3.4). The discrepancy between the two mass estimate suggests that the Seifried Keplerian fit may not provide an accurate measurement of the central mass in this case. It is possible that the source is a binary system. Binary systems produce lower luminosities than a single massive star, while simultaneously skewing the velocity field in the PV diagram (Cesaroni *et al.,* 2017). This is in agreement with Sanna *et al.,* 2019 who determine a central stellar mass of 20 $M_\odot$, almost directly in-between our two estimates.

The disk mass was determined to be 2.1 $M_\odot$ (Table 3.4), between 18-31% of the stellar mass. The Toomre stability plots (Figure 2.13) indicate stability around the central core, with marginal stability throughout the disk. The disk instability increases at larger radii, becoming highly unstable in B.

An eye-test of the PV diagram, combined with the increasing velocity gradient profile (Figure 2.6), suggest that G23.01 in Keplerian rotation. However, it is only experiencing marginal stability and the Kepler temperature profile does not produce a similar slope, indicating that the rotation not completely Keplerian. It is possible the source is young and in the early stages of forming a Keplerian disk, where part of the rotation is due to in-falling gas. This is confirmed by the work

of Sanna *et al.,* 2019, who suggests a disk close to free-fall with sub-Keplerian velocities, possibly only experiencing stable Keplerian rotation within the inner 500 AU.

3.2 G24.78 +0.08

The high-mass star forming region of G24.78 contains several cores, as seen in the continuum image (Figure 2.1), three of which have been reportedly showing signs of rotation (Beltrán *et al.,* 2011b).

In the Moment 0 map (Figure A.11), the CH_3CN emission predominantly covers source A1 and A2 (following the naming documentation of Beltrán *et al.,* 2005), and is the focus of this study for this particular region. Both cores display strong CH_3CN emission throughout the surrounding structure. A2 provides the clearest indication of rotation, as observed in the Moment 1 map (Figure A.11), with a N-S velocity gradient at a position angle of 0°, red-shifting in the N direction. This N-S gradient matches the gradient seen in Cesaroni *et al.,* 2017 and is perpendicular to the SiO outflow mentioned in Codella *et al.,* 2013. A2 to the NE was determined to have a velocity gradient at a position angle of 14° W of N, red-shifting to the NW. This gradient is fairly weak, particularly at higher K-lines, while Cesaroni *et al.,* 2017 could not find any gradient.

The temperatures derived from G24 represent the hottest in our sample (Figure A.15, Table 3.2 & 3.3), peaking above 700 K for LTE and 600 K for non-LTE, while averaging over 300 K for both A1 and A2. There is no defined point of peak temperature, with hot temperatures above 600 K are found throughout both sources.

Temperature gradients produce a T vs R slope of -0.4 ± 0.15 for both sources (Figure A.14). This suggests flared disks structures, agreeing within error of a slope of -0.5. The slope is clearly flattened due to the hot temperatures throughout the structure. Ahmadi *et al.,* 2018 indicated that external heating can produce positive slopes. While the slopes are not positive, external heating may be the cause of the flattening the slopes, albeit only marginally. The temperature profile assuming Keplerian rotation was constructed for A1 produces slope of -1.9, the steepest of the sample, well beyond the value determined through temperature gradients, indicating the structure is not likely in Keplerian rotation. A2 did not provide strong enough gradients for a second profile to be made, with little indication of rotation.

High CH_3CN column densities (Figure A.5) above 10^{16} cm^{-2} are spread throughout the sources in LTE analysis, peaking $5.5x10^{16}$ and $5.6x10^{16}$ cm^{-2} for A1 and A2, respectively. Assuming non-LTE, A1 peaks 0.5" SE of the continuum peak at $4.0x10^{16}$ cm^{-2}. This location does not coincide with a hot region, thus may be an indicator of build up from outward expansion of the gas. A2 CH_3CN column density profile is flat, averaging $9.6x10^{15}$ cm^{-2} throughout the source.

The H_2 column densities (Figure A.17)mirror that of the CH_3CN, with high col-

umn densities (>10^{24} cm^{-2}) throughout both sources. Both LTE and non-LTE peak around the continuum peak, however again high column densities are seen in the SE corner of A1, particularly in the non-LTE case.

Abundances (Figure A.18) for A1 peak 0.3" S of the continuum peak at 2.8x10^{-8} (for LTE) and to the NE section of A2 at 3.1x10^{-8}, while non-LTE produced lower, flatter profiles with no obvious peak point. For comparison to chemical models, the entire area was treated as one entity, instead of focusing on the specific cores. Only the Garrod models are able to reproduce the G24's CH_3CN abundances at high temperatures in their slow warm-up timescale, reaching 400 K. However, slow warm-up timescales only account for masses up to 6 $M_\odot$ (see Section 2.5), so it may be more reasonable to assume the medium warm-up time, as G24.78 A1 and A2 are O-type stellar objects. This medium warm-up phase results in a temperature of 220 K after approximately 210 kyr.

A PV diagram is produced for both sources, (see Figure A.12 & A.13). The fits result in central masses of 45 and 18 $M_\odot$ for A1 and A2, respectively. The luminosity of the region results in a 30 $M_\odot$ total between the two objects, thus the mass estimate for A1 is considered an overestimation. It should also be noted that source A1 is contaminated by a HII region surrounding the core, producing free-free emission (Beltrán *et al.,* 2007), thus the value determined by Beltrán *et al.,* 2007 of 22 $M_\odot$ for A1 is adopted for further analysis.

Both disk masses (Table 3.4) are substantial fractions of the central mass, at 12 $M_\odot$ (56%) and 15 $M_\odot$ (83%) for A1 and A2 respectively. The stability analysis in the Toomre plots (Figure A.19) clearly indicates both sources are highly unstable, albeit with small pockets of stability throughout the disk.

Both sources show weak indications of Keplerian rotation. A2 does not present strong enough velocity gradients for further analysis, and while A1 does present increasing gradients (Figure A.20) with decreasing radius, this does not guarantee Keplerian rotation. The structures are highly unstable and appear to have experience fragmentation. The modelling scenarios performed by Klassen *et al.,* 2016 indicate that fragmentation, followed by the formation of secondary cores at distances away from the original core, are expected for high-mass protostars, after the formation of a disk. This indeed may be the case for G24.78; secondary cores would explain the hot internal temperatures and overestimated dynamic masses. Thus it is possible that the structures in G24.78 are past their Keplerian disk stage, have experienced fragmentation are outwardly expanding. The analysis of Moscadelli *et al.,* 2018 agree with this conclusion, as they propose that the gradient observed in G24.78 A1 is due to outward expansion, and not rotation.

3.3 G29.96 -0.02

G29.96 displays a prominent hot molecular core (HMC), along with an ultracompact HII region, apparent as the arc-like feature to the W in Figure 2.1. The HMC may contain up to six cores (Sanchez-Monge, 2019). Core A represents the most

influential in the region, while to the SE lies the secondary core B. Core B may be in fact multiple cores, but our analysis is unable to confirm this with confidence, and therefore will treat this region as a singular unit.

A velocity gradient at a position angle of 55° W of N is found across the core A (Figure A.21), blue-shifting towards the SE and core B. The gradient matches well with the 52° found in Cesaroni *et al.,* 2017, who also indicate a perpendicular SiO outflow to this position angle, emerging directly from the HMC. The CH_3CN emission encompasses all of core A, extending until 0.5" SE of core B, failing to reach the tip of the "tail" of the structure. This elongated SW region contains several of the smaller cores mentioned by Sanchez-Monge, 2019, which are likely not be hot enough to sublimate the grain mantles to produce CH_3CN emission.

Peak temperatures (Figure A.24) were observed at the peak continuum emission, extending N of the peak by 0.25". The peak was measured at 696 K for LTE and 600 K for non-LTE. The surrounding gas for both scenarios remains above 200 K in the vicinity of core A and B, and drops below 100 K outside these regions.

The temperature profile constructed from the temperature gradient (Figure A.23) is modelled by an α value of -0.71. This is an indication that the disk is a geometrically flat, thin structure. Creating the same profile assuming Kepler rotation (Same figure) produces a slope of -1.10 $\pm$ 0.57. Technically the two values agree within error limits, although the errors are large in the Kepler case, and can only be considered a marginal agreement at best.

G29.96 produced the highest column density peak of our sample (Figure A.25, Table 3.2), reaching 7.0x10^{16} cm^{-2} for LTE analysis and mirroring the peak temperature location. The non-LTE case is lower, with locations both S, W and NE of the peak emission reaching near 2.0x10^{16} cm^{-2}.

The H_2 column density profile is fairly flat (Figure A.26), with the highest densities tracing the inner continuum contours. In the LTE case, the peak value of 1.4x10^{25} cm^{-2} is found at the CH_3CN emission edge to the SE. This is possibly due to a dense region near another core, although the extended morphology of the region indicates possible gas flow towards this SE edge.

Abundances within the contoured region (Figure A.27) peak again at the continuum peak and to the N in the LTE case, while the non-LTE displays a flatter profile, with marginally higher abundances at the NE outer edge. The average abundances fit the fast warm-up Allen model, producing temperatures of 113 K (compared to the average 122 K (LTE) and 151 K (non-LTE) in our study) with a warm-up timescale of approximately 22 kyr.

The PV plot can be seen in Figure A.22. The Seifried method yields a mass of 34 $M_\odot$, while the luminosity relation indicates a mass of 42 $M_\odot$. However this includes the HII region to the west, which is predominantly free-free emission. Thus it can be only concluded that the luminosity mass for G29.96 A and B is less than 42 $M_\odot$. That being said, our fitted value of 34 $M_\odot$ is within this luminosity limit, but it may include the mass of core B as well.

The disk mass of G29 is determined to be 24 $M_{\odot}$, 70 % of the stellar mass, and again encompassing the region of core B. If the area around core A is isolated, the resulting disk mass drops to 13 $M_{\odot}$. For consistency the larger values encompassing both cores for both disk mass and stellar mass are adopted. Toomre stability analysis (Figure A.28) further indicates the region is experiencing turbulent motion, as the entire disk region is unstable, particularly towards the SE edge.

Velocity gradients (Figure A.21) are seen perpendicular to an outflow (Cesaroni *et al.,* 2017), so while it can be said that some ongoing kinematic rotation within the disk structure, there is little evidence of Kepler rotation. The majority of the structure structure is flat and unstable. The inner stable region (0.25" around the continuum peak) may be a small disk in rotation, however the larger structure outside is likely due to outward expansion/outflow. It is possible that the source is more evolved, remnants of the Keplerian disk remain but the outer region has fragmented, producing the secondary cores in B, and is expanding. Sanchez-Monge, 2019 provides evidence that G29.96 has a disk, but it has been truncated by the outflow, while Cesaroni *et al.,* 2017 states that G29 is amongst the oldest of their sample population of O-type protostars.

3.4 G34.43 +0.24 MM1

G34.43 +0.24 is a infrared dark cloud (IRDC) of filamentary morphology, containing up to nine clumps (Sanhueza *et al.,* 2010). Rathborne *et al.,* 2008 determined one of these clumps, MM1, to be a hot molecular core in the early stages of forming a massive protostar, due to its high luminosity, H_2O maser emission and molecular outflows.

The Moment 1 map of CH_3CN (Figure A.30) displays a velocity gradient with a position angle of 55° W of N, red-shifted to the SE. Shepherd *et al.,* 2007 determined that there is an outflow perpendicular to this gradient, at an angle of 38° E of N.

Temperatures in G34 (Figure A.33) presents another hot region of 600+ K for both LTE and non-LTE scenarios. This hot zone is 0.5"x0.5" centralized around the continuum peak.

Temperature gradient profiles (Figure A.32) model an α value -0.68 $\pm$ 0.19. A flared disk structure is possible, but the gradient suggests some flattening of the disk. The temperature profile assuming Kepler rotation produces a slope of -1.10 $\pm$ 0.35. Similar to G29.96, while technically in agreement, it is a marginal fit at best.

Peak column densities (Figure A.34, Table 3.2) mirror the hot zone in LTE analysis, peaking at 4.1x10^{16} cm^{-2}. Column densities are found to peak S of the continuum in the non-LTE case, reaching a value of 2.0x10^{16} cm^{-2}.

The H_2 column density profiles (Figure A.35) are flat averaging 5.5x10^{24} cm^{-2}

over the whole structure, while peaking at 3.2x10^{25} cm^{-2}.

Abundances (Figure A.36) peak higher in the LTE case (8x10^{-9} vs 4x10^{-9} in non-LTE) but both average to approximately 1x10^{-9} within the contour limit. With average temperatures of 202 K(LTE) and 165 K(non-LTE), the data was fitted to the Garrod medium warm-up chemical model, producing a temperature of 160 K after 190 kyr.

The PV plot and Seifried fit can be viewed in Figure A.31. The fit yields 18 $M_{\odot}$, while luminosity estimates produces 12 $M_{\odot}$. Both masses are certainly plausible, but due to possibility of overestimation of dynamical masses from kinematic effects (e.g. as in Section 3.1, 3.2), the lower mass is adopted.

This is a critical difference, as the disk mass was determined to be 15 $M_{\odot}$, which is greater than that of the stellar mass. G34 represents the only source in the sample with an estimated disk mass larger than the stellar mass. In several cases in our sample, disk mass is strongly dependent on the chosen radius (the 10% peak continuum contour for consistency for all sources in our sample). However, in this case, reducing the radius to the 30% peak emission contour still produces a disk mass similar to the central stellar mass. The effects of the self-gravitating disk is seen in the Toomre plots (Figure A.37). G34 is distinctly unstable, and at risk of fragmentation.

As stated by Tan *et al.,* 2014, a disk in Keplerian rotation surrounding a protostar will eventually dissipate. Since signatures of rotation are present in G34, but highly unstable, it may be that G34 is in the process of evolving past its Keplerian rotation phase, moving towards fragmentation. The shape of the continuum contours may even suggest early signatures of spiral arms as the disk begins to fragment from instabilities. This is expected to occur in older protostars (Klassen *et al.,* 2016).

3.5 G35.03 +0.35

The high-mass star forming region of G35.03 +0.35 has previously been studied in detail (Beltrán *et al.,* 2014, Allen *et al.,* 2017) and contains up to six cores. In following Beltrán *et al.,* 2014 notation, core A is the focus of this study, as it was the only core to present significant CH_3CN emission.

The Moment 0 and Moment 1 maps can be seen in Figure A.39. A velocity gradient is present across the source at a position angle of 25° in the SW-NE direction. It is mainly blue-shifted, with red-shifting occurring on the NE edge. This gradient matches the one found in Beltrán *et al.,* 2014, who find extended outflow emission of $H^{13}CO^+$, C_2H, $C^{17}O$, $C^{34}S$, and H_2CS perpendicular to the position angle.

Temperatures (Figure A.42) reach 380 K in LTE and 460 K in non-LTE, within the inner 0.5" surrounding continuum peak. The average temperature (Table 3.3) is one of the coolest in the sample, averaging 119 K and 190 K in the LTE and non-LTE analysis.

The temperature as a function of radius profile (Figure A.41) produces the relation of $T \propto R^{-0.54}$, suggesting a flared disk structure. Assuming Kepler rotation, the relation becomes $T \propto R^{-0.66}$. The agreement between the two methods is one of the strongest in the sample, displaying convincing evidence of Kepler rotation.

LTE and non-LTE analysis of the CH_3CN column densities produced two different distributions (Figure A.43). Column densities peak at 4x10^{15} cm^{-2} at the continuum peak in LTE analysis, and drops below 10^{14} cm^{-2} at the outer edges. Non-LTE analysis produces peaks at 9x10^{15} cm^{-2} and remains above 10^{15} cm^{-2} along the NE-SW axis. The average column density is nearly a factor of 2x higher, however, as previously mentioned, this is skewed by the outer values where LTE analysis drops off significantly due to poor signal-to-noise ratios.

H_2 column densities (Figure A.44) mirror this NE-SW axis of higher densities, with dense points at the NE and SW edges, along with another high density point to the E, all approximately 1.0x10^{25} cm^{-2}. This NE-SW axis of high column densities aligns with the rotation gradient seen in Figure A.39. It is possible that we are observing an edge-on view of the disk, with the center plane being the mid-plane of the disk.

The ensuing abundance profiles (Figure A.45) are affected by the differences in column density distributions. LTE peaks at 2x10^{-9} around the continuum peak, while non-LTE peaks to the S at a higher value of 1.4x10^{-8}. The central values are within agreement with the main discrepancies again occurring on the outer edges. Overall, the average abundances are an order of magnitude higher in the non-LTE case. Due to the discrepancy of the two methods(LTE and non-LTE), a single abundance value of 1x10^{-9} is selected, as this value fits the central region for both scenarios. Similarly, average temperatures ranged from 117-190 K for the two scenarios. Due to possible overestimated temperatures (see Section 4.4 for further discussion), we err on the side of caution and choose the lower value. A fast warm-up time of 22 kyr produces 100 K for the Allen chemical model in this scenario.

The PV plot can be seen in Figure A.40. The plot shows signatures of Keplerian butterfly "wings", albeit the resolution is somewhat poor (0.18") in relation to the size of the source (0.6"). The Seifried PV plotting (same figure) produces a mass of 8 $M_\odot$, within the upper limit of the 10 $M_\odot$ from the luminosity relation, which contains the other intermediate and low-mass cores of G35.03.

G35.03 presents the smallest disk mass (Table 3.4), at 0.6 $M_\odot$ and has the lowest fractional ratio of disk mass to core mass at 0.08. This effect is seen in the Toomre stability plots (Figure A.46); G35.03 displays stable parameters throughout the disk, only experiencing instabilities near the NE and SW corners.

G35.03 clearly indicates a classic flared disk structure, with strong evidence of Keplerian rotation, which is stabilizing the disk from gravitational instabilities.

3.6 G35.20 -0.74N

The region of G35.20 -0.74N is a well known high-mass star forming region, characterized by an elongated structure containing two main YSO cores, A and B in Figure 2.2, and another core to the southeast, known as G35MM2 (Sánchez-Monge *et al.,* 2013). The region is surrounded by a NE-SW nebula, where bipolar outflows are detected in the same direction, observed in ^{12}CO (Gibb *et al.,* 2003).

In Figure A.48, the Moment 0 map exhibits a clumpy structure of this lower core. Both core A and B experience a velocity gradient, at position angles of approximately 20° W of N and 45° E of N, respectively. The gradient of core A is red-shifted towards the SE, and perpendicular to the bipolar outflow found in Gibb *et al.,* 2003. Core B is red-shifted to the NE and matches the outflow direction within 10°. This suggests that core A is powering the outflow, and the velocity gradient seen in core B is not of disk rotation, but of the resulting outflow. Higher resolved observations determine that core B is consisting of multiple cores (Allen *et al.,* 2017). While the ALMA archive data set is of high resolution (0.18"), defining the disk regions of the multiple cores in B is challenging and beyond the scope of this study, particularly due to the cores in B being of low-to-intermediate mass. Physical properties are determined for both A and B, referring to the labels of smaller cores in B from Allen *et al.,* 2017 when applicable, but rotation analysis will focus solely on core A for this study.

Temperatures in core A (Figure A.51) peak at the continuum peak at 576 K and 460 K, for LTE and non-LTE respectively. The multiplicity of the region is clearly seen in the temperature measurements of the region around core B; Peak temperatures are found to the S, reaching 248 (LTE) and 360 K (non-LTE). This location is labelled B3 in Allen *et al.,* 2017. The core that we label as B (B1 in Allen *et al.,* 2017) has lower peak temperatures of approximately 200 K.

The temperature gradient of core A (Figure A.50) decreases with radius with a slope of -0.51, suggesting a flared disk structure. Assuming Kepler rotation, the slope steepens to -1.05, outside the accepted range of the initial temperature profile

CH_3CN Column densities (Figure A.52) within core A peak at the central continuum peak at 7x10^{15} cm^{-2} and 8x10^{15} cm^{-2}, for LTE and non-LTE scenarios. Similar to G35.03, non-LTE analysis produces a flatter distribution and overall higher average column density (Table 3.3) of 3.2x10^{15} cm^{-2}, compared to 0.5x10^{15} cm^{-2} for LTE. In core B the there were no significant variations in CH_3CN column densities between the sub-cores, peaking at 5x10^{15} cm^{-2}.

H_2 column densities (Figure A.53) are highest at the central core (3.6x10^{25} cm^{-2} peak value), however there are also similar peaks in the NE and SW edges of core A, following a similar trend of high H_2 column densities in-line with outflow gradients. For core B, the higher H_2 column densities are seen in the N core (B1 from Allen *et al.,* 2017), peaking at 1.6x10^{25} cm^{-2}.

Abundances (Figure A.54) peak in the central core of A for LTE scenario (0.7x10^{-9}), and SE of the core in non-LTE scenario (2.0x10^{-9}). In core B, higher abundances

are found to the S near B3 from Allen *et al.,* 2017. Coinciding with the higher temperatures, this core likely has sublimated more grains and released more CH_3CN in the surrounding structure. Again, the non-LTE temperatures produce a flatter profile with a higher average abundance (Table 3.3). Thus, the same methodology is adopted for G35.20 as G35.03 for chemical modelling, and the comparison is made to the central core abundance of $0.7\text{x}10^{-9}$. We fit the data to the Garrod medium warm-up model, which produces a temperature of 160 K over 190 kyr.

G35.20 A PV plot can be seen in Figure A.49. Some signatures of a butterfly pattern are visible, indicating possible Keplerian rotation. PV fitting produces a mass of 10 $M_\odot$, while the luminosity mass estimate is 16 $M_\odot$. The luminosity estimate would include all of the smaller cores around core B, which are determined to be 4 $M_\odot$ or less by Allen *et al.,* 2017. Thus our PV mass estimate of of 10 $M_\odot$ is valid within the limit of 16 $M_\odot$.

Disk mass of G35.20 A is 1.2 $M_\odot$, with a fractional mass of 0.12. Toomre analysis (Figure A.55) indicates that G35.20 A is marginally stable, particularly within the inner radii, while the core B region suffers from instability.

It is likely that G35.20 A is experiencing moderate Keplerian rotation. It is marginally stable with outflows perpendicular to the velocity gradients. G35.20 A possibly represents a young protostar in its earliest stages of Keplerian rotation, with some infall. The rotation seen in core B is likely due to the outflow originating from core A. The instability seen around core B is a possible explanation for the multiplicity seen in the area, as fragmentation often produces new cores (Klassen *et al.,* 2016).

3.7 G37.55 +0.20

G37.55, also known as IRAS 18566+0408, is a high-mass star forming region of particular interest for its CH_3OH masers (van der Walt, 2014). G37 represents the lowest J-transition of CH_3CN amongst the sample (J = 6-5), and thus traces the coldest gas, up to approximately 200 K.

In the Moment maps (A.57), we see that the CH_3CN emission is centrally located, and does not trace the gas of the full continuum contours. While the emission region appears small, this is not the case as G37.55 is in fact the largest source, in terms of diameter, at approximately 20000 AU. It is likely the emission contours are tracing beyond any disk structure and into the surrounding envelope, or the disk is a massive toroid structure. A clear velocity gradient is visible across at a position angle of 106° W of N, red-shifted just S of W, and blue shifted in the opposite direction. Outflows have been found centered at the continuum peak in the NW-SE direction, mapped in SiO by Zhang *et al.,* 2007. This outflow coincides within 30° of the E-W gradient in the Moment 1 maps, suggesting the emission traces the outflow instead of Keplerian disk rotation.

Temperature distributions (Figure A.60) peak S of the continuum peak for LTE at 337 K, and 420 K at the continuum peak for non-LTE. G37 represents another

cool source, averaging temperatures (Table 3.3) of 108 K and 139 K for LTE and non-LTE analysis, respectively.

The temperature gradient profile (Figure A.59) is on the order of $T \propto R^{-0.94\pm0.57}$. The closest fitting description is of a flat disk, which produces a profile of $T \propto R^{-0.75}$, however, these findings are ambiguous due to the large error in the fit. With the Keplerian rotation assumption, the slope increases to $T \propto R^{-1.62\pm0.36}$. Both slopes are technically within agreement, but again due to the large error in both results, a conclusion of Kepler rotation cannot be validated with this method.

Both column density distributions (Figure A.61) emulate each other, peaking at the continuum peak at approximately 1.0x10^{16} cm^{-2}.

In contrast, the H_2 column densities (Figure A.62) peak on the outer edge of the disk structure, reaching 2.0x10^{24} cm^{-2}. This value is the lowest peak (and average of 5.0x10^{23} cm^{-2}) of the sample.

The abundance distributions can be seen in Figure A.63. As a result of the low H_2 column densities and the moderate CH_3CN column densities, the CH_3CN abundance for G37 is the highest of the sample, averaging above 1.0x10^{-8} and peaking at 6.7x10^{-8}. These abundances fit with the Allen fast warm-up time, producing temperatures of 113 K (compared to the average 108 (LTE) and 139(non-LTE) measured for G37) after approximately 23 kyr.

The most notable difference in G37.55, when compared to the rest of the sample, is seen in the PV plot (Figure A.58). While all sources display different PV morphology, G37 presents a particularly unique ellipsoidal shape. This PV diagram fits a very high central mass fit of 66 $M_\odot$, approximately a factor of three greater the mass of 24 $M_\odot$ calculated from the luminosity.

As expected from its large size, the mass of the disk is quite high at 17 $M_\odot$, upward to 70% of the stellar mass. However, if we consider the region of CH_3CN emission to be the true disk area, the disk mass decreases to 10 $M_\odot$, only 42% of the stellar mass. In the Toomre Plots (Figure A.64), the disk is found to be marginally stable in its inner radius.

G37 display little-to-no signatures of Keplerian rotation. One can observe that the PV plot does not resemble a Kepler pattern in any form. A similar pattern was determined by Silva *et al.,* 2017, who deduced no rotation in G37, however, they were also not able to find any velocity gradients, which were found both in our study and that of Hofner *et al.,* 2017. Another factor to consider is the resolution of the data. Cesaroni *et al.,* 2017 were able to produce a similar PV plot morphology from their O-type protostar, G345.50, by degrading the angular resolution by a factor of 3.5, distorting the original PV pattern. While G37 represents the poorest resolved source in our source sample, the fact that it has produced two similar PV plots from two different instruments (ALMA; 0.99" angular resolution, Submillimeter Array (SMA) in Silva *et al.,* 2017; 2.0"(compact) and 0.4"(very-extended) angular resolution) suggests it is not solely a resolution effect. It is likely the velocity gradients seen are due to expansion, which is corroborated by

the high H_2 densities on the outer edges of the structure. This expansion must be relatively slow, as the disk itself is marginally stable.

3.8 AFGL 4176

Historically, AFGL 4176 is significant as it represents the first O-type star to display strong evidence of Keplerian-like properties in its disk, shown by Johnston *et al.,* 2015. By tracing the disk kinematics with CH_3CN in Moment maps and LTE line modelling, they were able to show velocity clear gradients and higher order velocities at small radii, with a central mass of 25 $M_\odot$. The structure observed were consistent with the models presented by Boley *et al.,* 2012. AFGL 4176 represents a benchmark for kinematic analysis to compare with to other targets. Similar to Johnston *et al.,* 2015, the data from the ALMA archive is that of CH_3CN(13-12). However, unlike the rest of the sources presented in this study, AFGL 4176's spectrum only contains K-lines 5-8. Thus, one must err on the side of caution when viewing the results, and a bit more emphasis is placed on comparison to literature for this source. This is remarked upon later in Section 4.5.

The area has several Class II methanol maser spots in close proximity to the source; in the continuum image (Figure 2.1) two are visible, the main target labelled as mm1, and a secondary core mm2.

Despite having only higher K-lines, which in most cases are less prominent, we can see in the Moment maps (Figure A.1) why AFGL 4176 is a strong candidate for Keplerian rotation. Particularly in the velocity Moment 1 map, we see a striking gradient, shifting from red to blue in the N-W direction. This velocity gradient matches the position angle of 61.5° W of N presented by Johnston *et al.,* 2015, who note a bipolar outflow perpendicular to this position angle, observed in ^{12}CO

AFGL temperature (Figure A.4) peaks at 380 K for the LTE analysis and 330 K for the non-LTE analysis, with average temperatures around 150 K for the entire source. Both peaks are just within a hot zone 0.6"x0.6", encompassing the continuum peak, with the LTE peak to the E and non-LTE to the N. Johnston *et al.,* 2015 found excitation temperatures peaking at 290 K, while Bøgelund *et al.,* 2019 found 270 ± 40 K. Our results thus present moderately hotter conditions, and may be because the K=5-8 CH_3CN lines trace the higher end of the temperature spectrum.

The temperature profile constructed from the measured temperature gradient generates a slope of -0.57. This is an indication of a flared disk structure. Assuming Kepler rotation, a matching slope is produced of -0.51, further indication that AFGL 4176 is indeed in Keplerian rotation.

The CH_3CN column densities (Figure A.5) peak 3.0 and 2.0x10^{16} cm^{-2} for the non-LTE and LTE analysis, which are in agreement with Johnston *et al.,* 2015 (2.8x10^{16} cm^{-2}) and Bøgelund *et al.,* 2019 (3.4x10^{16} cm^{-2}).

H_2 column densities (Figure A.6) peak at 2.0x10^{24} cm^{-2}, however only the non-LTE peaks at the continuum peak. The non-LTE scenario peaks to the north within the mm2 source. This peak value agrees with the H_2 column density determined for mm2 in Johnston *et al.,* 2020, but they also determined that mm1 peak at 8.0x10^{24} cm^{-2}, higher than our peak mm1 value.

The differences in column density distributions results in an abundance distribution (Figure A.7) that varies as well between the two methods, particularly in a flatter LTE profile. Both values peak around 2x10^{-8}. The outer abundances are higher in the non-LTE case, due to the flatter profile we see in the CH_3CN column densities. It is determined that these abundances best fit a fast warm-up time in the Allen *et al.,* 2017 chemical model, producing temperatures of 132 K (comparing to the 139 and 156 K average temperatures) after 25 kyr.

In Figure A.2 the position-velocity diagram for AFGL 4176 is shown. Higher K lines represent weaker emission and thus provide more of a challenge to interpret their analysis. While the shape does not appear to be of the expected "butterfly" pattern, it matches well with the high K-line patterns produced in Johnston *et al.,* 2015, who present lower K-line PV diagrams that are indicative of Keplerian rotation. The luminosity and dynamical derived masses agree at 27 $M_\odot$. This agreement between the two methods is another indication that the PV plot is likely displaying Keplerian rotation

The disk mass (Table 3.4) is derived from the 1.21 mm continuum emission, and is 2.8 $M_\odot$, around 10 % of the central mass. Stability analysis (Figure A.8) results in a highly stable disk around mm1, becoming more unstable at higher radii as we move towards mm2.

Even with the truncated K-ladder, the analysis of this thesis indicates AFGL 4176 is a classic flared disk, stabilized by Keplerian rotation. One difference to note is our adopted disk mass of 2.8 $M_\odot$. This is notably lower than the 8.0 $M_\odot$ determined by Johnston *et al.,* 2020. However it should be noted that the authors used a dust opacity of 0.24 g/cm^{-2} for 1 mm emission, as compared to our value of 1.0 g/cm^{-2}. Sanna *et al.,* 2019 makes the same observation, noting that the lower value may be more appropriate for diffuse clouds, and that if the dust opacity is changed to 1.0, similar disk masses are produced.

Table 3.1: Slopes of Temperature and Velocity Gradius vs Radius Profiles

Name	T vs R	T vs R (Kep)	V_{grad} vs R
AFGL 4176	-0.57 ± 0.25	-0.51 ± 0.09	-0.55 ± 0.04
G23.01 -0.41	-0.52 ± 0.14	-1.48 ± 0.30	-0.43 ± 0.09
G24.78 +0.08 A1	-0.40 ± 0.15	-1.94 ± 0.54	-0.39 ± 0.05
G29.96 -0.02	-0.71 ± 0.11	-1.10 ± 0.57	-0.39 ± 0.08
G34.43 +0.24 MM1	-0.68 ± 0.19	-1.10 ± 0.35	-0.66 ± 0.05
G35.03 +0.35	-0.54 ± 0.22	-0.66 ± 0.13	-0.39 ± 0.16
G35.20 -0.74N A	-0.51 ± 0.17	-1.05 ± 0.19	-0.70 ± 0.10
G37.55 +0.20	-0.94 ± 0.56	-1.62 ± 0.36	-0.43 ± 0.11

Table 3.2: Peak values of Physical Properties

Name	Temperature		CH_3CN Column Density		H_2 Volume Density	H_2 Column Density		Abundances	
	LTE	non-LTE	LTE	non-LTE		LTE	non-LTE	LTE	non-LTE
	(K)	(K)	(10^{16} cm^{-2})	(10^{16} cm^{-2})	(10^6 cm^{-3})	(10^{25} cm^{-2})	(10^{25} cm^{-2})	(10^{-8})	(10^{-8})
AFGL 4176	383	330	3.0	2.0	0.9	0.2	0.2	2.5	1.7
G23.01 -0.41	610	520	1.5	2.2	0.8	2.6	1.5	0.3	0.3
G24.78 +0.08A1	746	600	5.5	4.0	0.6	1.4	1.0	2.8	1.2
G24.78 +0.08A2	729	600	5.6	1.0	0.7	0.8	0.5	3.1	3.8
G29.96 -0.02	696	600	7.0	2.0	0.9	1.7	1.2	1.5	0.6
G34.43 +0.24 MM1	764	600	4.1	2.0	1.0	3.2	1.4	0.8	0.4
G35.03 +0.35	382	460	0.4	0.9	0.9	1.0	0.4	0.2	1.4
G35.20 -0.74N A	576	460	0.7	0.8	6.0	3.6	1.3	0.07	0.2
G35.20 -0.74N B	248	360	0.1	0.5	4.0	1.6	1.1	0.03	0.2
G37.55 +0.20	337	420	1.1	1.0	4.0	0.2	0.2	4.9	6.7

Table 3.3: Average values of physical properties.

	LTE Analysis					non-LTE Analysis				
Source	T	N_{CH_3CN}	N_{H_2}	CH_3CN/H_2	n_{H_2}	T	N_{CH_3CN}	N_{H_2}	CH_3CN/H_2	n_{H_2}
	K	10^{15} cm^{-2}	10^{24} cm^{-2}	10^{-9}	10^7 cm^{-3}	K	10^{15} cm^{-2}	10^{24} cm^{-2}	10^{-9}	10^7 cm^{-3}
AFGL 4176	156	4.1	0.8	5.6	1.0	139	6.0	0.8	8.2	1.0
G23.01	217	3.2	6.6	0.8	9.5	168	8.3	7.0	1.6	10.1
G24.78 A1	374	13.4	3.5	5.4	4.0	331	9.6	3.9	3.4	4.5
G24.78 A2	367	13.7	2.4	6.3	2.8	315	8.0	2.5	4.9	2.9
G29.96	151	6.9	2.9	2.8	2.9	122	6.6	3.4	4.6	3.4
G34.43	202	6.0	5.5	1.2	7.1	165	6.2	5.7	1.2	7.3
G35.03	117	0.9	2.9	0.4	10.0	190	6.1	1.4	5.1	4.9
G35.20 A	119	0.5	7.7	0.1	28.9	184	3.2	4.3	0.8	16.4
G37.55	108	2.2	0.5	10.3	0.2	139	1.9	0.5	12.0	0.2

Table 3.4: Summary of Mass Profiles

Name	Luminosity[1]	Stellar Mass		Disk Mass	M_{disk}/M_*[2]
		Luminosity	Dynamical		
	(10^5 $L_\odot$)	($M_\odot$)	($M_\odot$)	($M_\odot$)	
AFGL 4176	1.7	27	27 ± 3	2.8 ± 0.3	0.10
G23.01 -0.41	0.4	16	26 ± 3	4.9 ± 0.3	0.18 - 0.31
G24.78 +0.08A1	<2.2	<30	45 ± 5	12.3 ± 1.7	0.56[3]
G24.78 +0.08A2	<2.2	<30	18 ± 2	15.0 ± 1.0	0.83
G29.96 -0.02	5.8	<42	34 ± 5	24.4 ± 3.2	0.71
G34.43 +0.24MM1	0.2	12	18 ± 2	15.3 ± 0.8	0.85 - 1.28
G35.03 +0.35	0.1	<10	8 ± 1	0.6 ± 0.1	0.08
G35.20 -0.74N	0.4	<16	10 ± 1	1.2 ± 0.1	0.12
G37.55 +0.20	1.2	24	66 ± 9	17.0 ± 1.2	0.26 - 0.71

Notes:[1]Luminosity values obtained from RMS Database(G24, G29, G35.20, G37.55), Johnston *et al.,* 2015(AFGL), Sanna *et al.,* 2019(G23), Rathborne *et al.,* 2008(G34) and Beltrán *et al.,* 2014(G35.03)

[2]Ranges are given for mass ratios when two valid stellar masses are determined.

[3]Mass ratio for G24.78 A1 uses stellar mass of $22M_\odot$ determined by Beltrán *et al.,* 2011b, due to uncertainties in stellar masses of this study. See Section 3.2 and Section 4.3 for further discussion.

Chapter 4

Discussion

In this section, the individual results of the sample will be compared to each other, in attempts to determine any similarities within the sample, followed by a final classification of the sources. Following the comparative analysis, potential sources of uncertainties of this thesis will be discussed.

4.1 Comparative Results

4.1.1 Kinematics and Structure

To determine the structure of the disks surrounding the sources, and if the disks were in Keplerian rotation, temperature and velocity gradient profiles were produced. The results of the profiles are shown in Table 3.1. All eight of the analyzed sources experience increasing velocity gradients as a function of decreasing radius, i.e. the velocity gradient becomes steeper with increasing K-lines. This is expected for disks in Kepler rotation, gas tracing the hottest regions are closest to the central source and experiencing the fastest velocities. However, CH_3CN can trace velocity gradients from non-Keplerian rotation as well, such as outflows. At this point we can conclude that all sources are undergoing some form of rotation, but more information is needed to confirm Keplerian rotation.

As mentioned in the introduction, a geometrically thin, flat disk produces a temperature-radius profile of $T \propto R^{-3/4}$, while a flared disk has a more shallow profile of $T \propto R^{-1/2}$. Six sources display indications of a flared disk; AFGL 4176, G35.03, G23.01, G24.78(A1 and A2) and G35.20 A, while three present flat disk structures (G29.96, G34.43, and G37.55). G34.43 is somewhat ambiguous, as it is within error of both a flat and a flared disk. It is possible that the structure of G34.43 is somewhere in between that of a flat disk and a classic flared disk, however it will be classified as a flat disk in this study. Similarly, G24.78 is within error of a flared disk, but on the other side of the spectrum, with a lower α value. This is the case for both sources A1 and A2 (α = -0.40 and -0.39, respectively). As seen in the temperature distribution (Figure A.15), both sources have hot temperatures throughout their structures, flattening the temperature profile. The

hot temperatures could be due to new binary systems formed from fragmentation (Klassen *et al.,* 2016). Further imaging into FIR wavelengths would be needed to confirm any sources of UV radiation being absorbed by the surrounding dust. Finally, G37.55 represents the most dubious result, a slope steeper than both models, albeit with an error large enough to fit either. A possible interpretation is that G37 is a flat disk with a more significant cool down in the outer radius, as compared to the other sources in the sample. This cool-down may be in part due to the large radius of the disk, as the internal radiation does not reach the outer measurements. This effect is likely enhanced by the low K-lines available from the G37 data. G37 may be experiencing higher temperatures, but the CH_3CN lines are not able to accurately trace this gas.

From the second temperature profile (see Section 2.3.3), an assumption is made that the disk is in Keplerian rotation. If the assumption is true, the resulting slope should equal that of the initial temperature profile, determined through temperature gradients. The results of this fit are shown in Table 3.1. AFGL 4176 and G35.03 show the clearest agreement between the two methods, while G29, G34 and G37 agree within error (albeit in G29 and G37 cases, this is partially due to large errors of the fits). This leaves G23, G24. and G35.20 where the Keplerian rotation assumption breaks down.

It should be noted that in the T vs. R plots, the majority of line widths measured only trace the inner 100 - 500 AU of the sources, while they all have temperature gradients in the vicinity of 1000 AU. No line widths were measured to extend beyond the inner radius of the disk, which may have flattened the slope. The strength of CH_3CN as a tracer lies in its ability to trace hot gas, thus there is likely higher uncertainties in tracing lower temperatures, such as those needed to trace the outer regions of disks. Further analysis with a more advanced tool such as XCLASS[1](Möller *et al.,* 2017), CASSIS[2](Vastel *et al.,* 2015, or MADCUBA[3](Martín *et al.,* 2019) would be useful, to see if similar results are produced.

Another characteristic of Keplerian rotation is the "butterfly" pattern produced by the PV plot. The majority of PV plots are shown in the Appendix, while G23.01 is shown in the Section 2. No two PV plots in our sample are the same, clearly showing unique kinematics ongoing within the structures of each disk. Purely from visual inspection, G23 provides the best example of a butterfly pattern, while the majority of others showing some aspects. G37 is notable because of its ellipsoidal shape, which may not be the true shape of the PV plot. Cesaroni *et al.,* 2017 were able to produce a similar shape in their source G345.50 , by degrading the angular resolution by a factor of 3.5, altering the original "true" PV diagram. G37 is the poorest resolved within the sample, and thus this alteration must be taken into consideration. However, Silva *et al.,* 2017 found similar patterns with the SMA telescope. It is likely that G37 is experiencing only small levels of rotation, and

[1]XCLASS is available from xclass.astro.uni-koeln.de/

[2]CASSIS is available from cassis.irap.omp.eu/

[3]MADCUBA is available from https://cab.inta-csic.es/madcuba/MADCUBA_IMAGEJ/ImageJMadcuba.html

the PV plots are degraded further by resolution issues.

A more quantified method of viewing the Kepler fits is via the Seifried method, used to determine the mass. The error in respect to the mass can give a quantitative measure of the strength of the fit. G29 and G37 are the two sources with the highest fractional error, indicating the weakest fits of a $V \propto R^{-1/2}$ Keplerian profile. However, these PV plots are at risk of morphology effects due to the physical conditions, such as multiplicity, occurring within the disk or central source. This is further expanded upon in Section 4.1.2.

Overall, what can we say about the structures surrounding our protostars? Are they disks in Keplerian rotation? The velocity gradients indicate that all of our sources are experiencing some sort of rotation, but which of ones are in Keplerian rotation in particular? Based on the above analysis, AFGL 4176 and G35.03 represent flared disks with the strongest indications of Keplerian rotation. G23 and G35.20 also are flared disks, but only show marginal, sub-Keplerian, rotation evidence. It is possible they are in earlier stages of formation, with partial infalling gas and not fully in Keplerian motion. G34 appears to be in the opposite regime. Although signatures of rotation exist, the disk is highly unstable with indications of spiral arm formation. G34 may be past its stable Kepler rotation stage, entering a fragmenting regime. G24 is highly unstable and most likely fragmented. A1 appears to have rotation, but this is presumably due to outward expansion, while A2 shows no signs of rotation. They both present flared structures, but this too may be distorted. G29 shows minimally indications of Keplerian rotation, and is a flat structure. It is likely an older protostar experiencing expansion. Finally, G37 is likely a thin, flat structure experiencing no disk rotation, but possible outward expansion.

4.1.2 Stellar and Disk Mass Profiles

This sample is split into two sub groups; O-type stars (masses >15 $M_\odot$), including AFGL 4176, G23.01, G2478(A1 and A2), G29.96, and G37.55, and B-type stars (masses between 8 - 15 $M_\odot$). The remaining three sources, G34.43, G35.03 and G35.20, fall within this second sub-grouping.

Two methods were used to determine stellar masses, from luminosity values and dynamically through Kepler fitting of PV plots. Both methods have factors affecting the final masses. Luminosity provides accurate masses when there is only a single source. For regions, the mass is the total sum of masses within the region, and can only provide an upper limit as noted in Table 3.4. AFGL 4176, G24.78 A2, G29.96, G34.43, G35.03, and G35.20 represent the subsection where these two methods are in agreement. G23.01, G24.78 A1 and G37.55 represent situations where the Kepler fitting resulted in a mass overestimation, larger than that of the luminosity relation. Cesaroni *et al.,* 2017 provides insight on this situation for G24. The authors note the dual lobed configuration seen in the PV plot (similar to Figure A.12), and how an expected 20 $M_\odot$ Kepler fit would have to ignore one of these lobes completely. Thus, it was concluded that G24 may be multiple sources within one core, distorting the fit. This assumption can then be extrapolated for

G23 as well, as the fits differ by 10 $M_{\odot}$. G23 does present a dual lobe PV plot, albeit much less extreme than the case of G24, and as a result the Kepler fit is not overestimated to the same degree as G24. Therefore, it is possible that G23 contains multiples sources within its core as well, but one core is kinematically dominant over the other(s), minimizing the effect. G37 has the most poorly fitted Kepler fit, and the 66 $M_{\odot}$ is most certainly an overestimation. While it could be due to a multi-stellar core, as remarked previously, this is most likely due to the poor resolution distorting the PV plot, or no rotation is occurring and PV fitting to a Kepler model is an invalid method of determining mass.

Disk mass was computed from the ALMA continuum data. Disk masses ranged from 0.6 - 25 $M_{\odot}$, with the most massive disks commonly found around the most massive stars. Four protostars have disk masses less than 50% of their stellar mass: AFGL 4176, G23.01, G35.03 and G35.20. AFGL and G23.01 are the only O-type stars within this lower disk mass regime. G24.78 (A1 and A2), G29.96, G34.43 and G37.55 all have disk masses greater than 50% of their stellar mass, with all of them being O-type stars. Thus, the sample indicates that larger fractional disk masses are more common in O-type protostars than their B-type counterparts. It is important to note that Keplerian rotation cannot occur when the disk mass exceeds the stellar mass (Cesaroni *et al.,* 2017), as it would be self-gravitating and fragment. G34.43 represents the only structure where this is at risk of occurring.

The stability of the disks is determined through Toomre Q stability plots (Figures A.8(AFGL), A.19(G24.78), A.28(G29.96), A.37(G34.43), A.46(G35.03), A.55 (G35.20), A.64(G37.55) and 2.13(G23.01)). This is important to consider, as many of the models of disk structure and kinematics are based upon steady-state, i.e. stable conditions. The sample is divided into three subsections based on Toomre analysis: stable (AFGL 4176, G35.03), marginally stable (G23.01, G35.20A, G37.55) and unstable (G24.78 A1 and A2, G29.96, G34.43, G35.20 B). The most significant factors in resisting asymmetric instabilities come from hot temperatures and high velocity rotation, often strongest at the core. This is seen in all sources, where the inner most data points represent the most stable regions. It is also likely why the two prime Keplerian candidates, AFGL and G35.03, are also the two most stable sources; a strong Keplerian rotation is stabilizing the disk. Klassen *et al.,* 2016 simulated the formation sequence of high-mass protostars. In all cases the disks eventually reached instability, formed spiral arms and fragmented. This fragmentation then formed a second binary source, approximately 1200 AU away from the central source. While several sources present signatures of instability, this fragmentation process appears most likely in G24.78. The Toomre plots show varying Toomre Q parameters within and beyond the disk structure, including small pockets of stability. Whether binary systems have been formed cannot be confirmed here, but it is supported by the overestimated mass from PV diagram fitting.

4.1.3 Thermal and Physical Properties

The results of the physical property analysis is shown in Table 3.2 (peak values), and Table 3.3 (average values). It should be noted that G35.20 B is not included in the Averages Table, as it is actually multiple cores (Allen *et al.,* 2017), and determining a boundary for each source was challenging and inconsistent. Given this, G35.20 average results are in reference to the main northern core of G35.20 A. Four sources, G29, G24 A1 & A2, and G34, peaked at high temperatures of 700+ K for LTE analysis. It must be noted that at these high temperatures, the population diagrams experienced poor fits, with errors up to 50%. This is possibly due to optical depth effects (see Section 2.4.1), resulting in an overestimation of temperature. However, the non-LTE also produced high temperatures, reaching the maximum 600 K. The collisional excitation rates for CH_3CN from the LAMDA database were determined by Green, 1986 for up to 140 K, and are then extrapolated to higher temperatures. This is generally considered reliable, but our analysis found temperatures reached a maximum cap at 600 K, before the results would start to break down. That being said, this 600 K value is more likely the accurate measurement of peak temperature for the hot sources, compared to the LTE results which suffer from large errors. The remaining sources ranged in the 300 - 500 K for peak temperatures, with relative (within 50-100 K) agreement between LTE and non-LTE analysis. The majority have a temperature peak at the location of the continuum peak emission, or within 0.5" or less. The exception is G24.78, displaying hot temperatures throughout the disk, in both A1 and A2, and in both LTE and non-LTE analysis. This is possibly be due to the external heating mentioned in Section 4.1.2.

Peak column densities within the sample are in the range of 10^{16} cm^{-2}, again often peaking near the continuum peak. G29 has the highest peak column density ($7\text{x}10^{16}$ cm^{-2}), while G24 has the highest column density averaged over the entire source (both A1 and A2 averaging around $1.3\text{x}10^{16}$ cm^{-2}). At the other end of the spectrum, G35.03 has the lowest peak ($4.0\text{x}10^{15}$ cm^{-2}) and G35.20 has the lowest average ($5.4\text{x}10^{14}$ cm^{-2}) CH_3CN column density, noting they are both the lowest mass protostars of the sample. There is a noted difference between the LTE and non-LTE distribution (Figures A.5,(AFGL), A.16(G24.78)), A.25(G29.96), A.34(G34.43), A.43(G35.03), A.52(G35.20), A.61(G37.55) and 2.9(G23.01)). Non-LTE analysis produces much flatter profiles, with higher column densities on the outer edges of the disks. The lower LTE values again may be due to the underestimation of column densities from the lower-K lines. It also may be the LTE assumption does not hold for the outer regions in particular, where the gas is less dense.

H_2 column densities are determined from continuum emission. AFGL 4176 and G37.55 display the lowest H_2 column density peaks and averages, while G23.01 and G35.20 show the highest. Some sources displayed higher column densities at outer regions of the disk (G23, G29) suggesting a build-up of material from shocks or outflows. In conjunction, due to their low H_2 column densities and moderate CH_3CN column densities, AFGL and G37 have the highest abundance

ratios of the sample. Both sources rank among the larger stellar masses for a single object, and likely have sublimated larger abundances of CH_3CN. In the same vein, G35.03 and G35.20 have the lowest stellar masses, and have the lowest fractional abundances, indicating a link between stellar mass and CH_3CN abundance. The links between abundances, temperatures, column densities and stellar masses are further investigated in Figure 4.1:

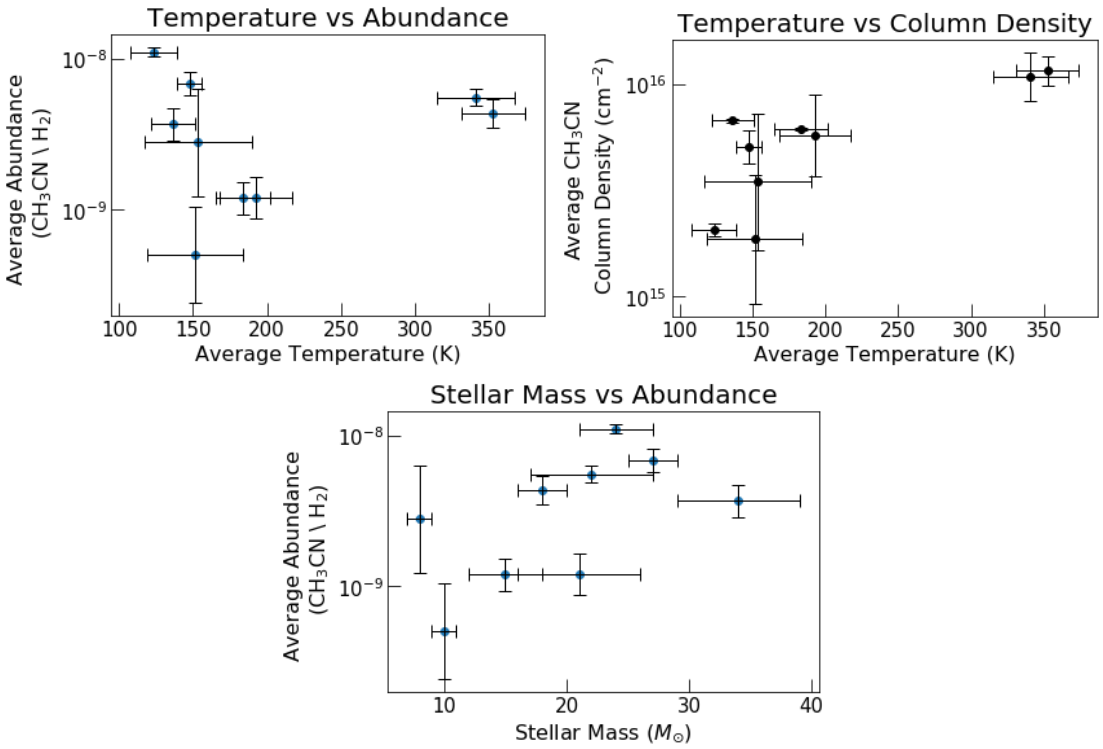

Figure 4.1: *Top Left*: Average temperature vs. average abundances of the sample. *Top Right*: The relation between average temperature and average CH_3CN column density. Uncertainty bars for abundances, temperatures and column densities encompass both LTE and non-LTE results. *Bottom:* Stellar mass vs. average abundances. Stellar mass uncertainties encompass both luminosity and dynamic fits (when valid).

The top left plot of Figure 4.1 indicates a relation between abundances and temperature, albeit only marginally. In general, hotter sources should produce higher CH_3CN abundances via sublimated of the surrounding ice mantles. However this plot is slightly skewed by sources such as G37, which has the lowest H_2 column densities, and thus the highest abundances, despite being one of the cooler sources (Table 3.3). This may indicate that G37 should be warmer, but our analysis was not able to produce higher temperatures due to the low K-transition of G37. In conjunction with this result, a second plot was constructed (top right of Figure 4.1) of CH_3CN column density vs. temperature, as a more direct comparison of CH_3CN and temperature, to see if similar results are produced. The relation appears to more strongly indicate that higher CH_3CN column densities are found

for hotter sources. In the same vein, the bottom plot of Figure 4.1 displays the stellar mass as a function of abundances. B-type stars would be expected to evaporate less grains in the surrounding envelope, producing lower abundances. This appears to be the case in our sample. Overall, these plots indicate the CH_3CN column densities and abundances are a function of stellar mass and temperature of the central source.

Non-LTE modelling also produces H_2 volume density profiles for our sources (Figures A.9(AFGL), 2.10(G23), A.20(G24), A.29(AG29), A.38(G34), A.47(G35.03), A.56(G35.20), and A.65(G37)). The profiles produced are quite flat, in the range of 10^{5-6} cm^{-3}. This is a magnitude of 1-2 lower than expected for densities in disks around high-mass stars (Tan *et al.,* 2014, Table 1.1). Since the densities in all our sample are high enough to thermalize population levels (i.e. higher than the critical densities in Table 2.2), the CH_3CN emission only models the lower limit of the volume density. This is further confirmed by determining volume densities from the continuum derived H_2 column densities (Table 3.3). This method results in average H_2 volume densities of 10^{7-8} cm^{-3} for seven of eight sources. The exception is G37; the average volume density determined from the continuum emission was $2x10^6$ cm^{-3}. The volume density derived from non-LTE modelling peaks at $4x10^6$ cm^{-3} (Table 3.2), with the inner 3.0"x3.0" above 10^6 cm^{-3} (Figure A.65) , within agreement of the continuum method. This suggests the G37 volume density distribution may be of the non-LTE RADEX distribution. However, for all other seven sources, the non-LTE volume density is several magnitudes low. Thus the H_2 distributions would mirror that of the H_2 column density for these sources, and not the H_2 non-LTE volume distribution.

4.1.4 Chemical Modelling and Timescales of CH_3CN

Table 4.1 presents the results of the chemical modelling comparison. The models are described in more detail in the Section 2.5. The range of measured temperatures includes both the average LTE and non-LTE analysis. AFGL 4176, G29.96, G35.03 and G37.55 best fit with fast warm-up models. To fit with our mass estimates, these sources would need episodic accretion rates greater than 10^{-4} $M_{\odot}yr^{-1}$, with G35.03 having the highest accretion rate. G35.03 also partially fit with the Slow Garrod model, but this resulted in higher modelled temperatures. Since it is suspected that measured temperatures are overestimated in some scenarios, in cases of doubt, the lower temperature fit is adopted. G24.78, our hottest cores, was also a closer fit with the slow Garrod model in terms of temperature, producing a modelled temperature of 400 K. However, this model is the result of stellar masses too low (on the order of 1-6 $M_{\odot}$, depending on the accretion rate) compared to those estimated for G24.78 A1 and A2. Again we also preferred to err on the side of lower temperature values (18-22 $M_{\odot}$).

The remaining four sources fit a medium warm-up phase model, all by the Garrod model. The Garrod model generally performs better with hotter sources, as the Allen model produced higher abundances at lower temperatures.

Table 4.1: Results of Chemical model fitting.

Source	$T_{measured}$	Best Fit Model	$t_{warm-up}$	T_{model}	Author
	K		10^4 yr	K	
AFGL 4176	139 - 156	Fast	2.5	109	Allen
G23.01	168 - 217	Medium	19	160	Garrod
G24.78	315 - 367	Medium	21	220	Garrod
G29.96	122 - 151	Fast	2.2	100	Allen
G34.43	165 - 202	Medium	19	160	Garrod
G35.03	117 - 190	Fast	2.3	113	Allen
G35.20	119 - 184	Medium	19	160	Garrod
G37.55	108 - 139	Fast	2.3	113	Allen

Notes: Temperatures ranges encompass average LTE and non-LTE temperatures.

Due to the visual nature of this comparison, it is worth determining the validity of these values. A possible comparison is the dynamical time-scale of associated jets, which is simply the length of the jet divided by its velocity. Beuther *et al.,* 2002 studied 24 HMSFRs and found the time-scales in the range of 0.5-18.4x10^4 yrs, and moderately fits the two subsections we derived. However, all of the sample have some form of outflow observed in previous studies, thus a literature search was completed to obtain specific dynamical time-scales. Values were found for six sources; G34.43 and AFGL 4176 have associated jets, but dynamical timescales are not produced due to the edge-on orientation of the outflows (Johnston *et al.,* 2015, Rathborne *et al.,* 2008). All values fall within the fast warm-up timescale, with the exception of G37; 75 kyr would fall into the medium warm-up phase for the Allen model. It should be noted that for this phase and the derived abundances for G37, this would produce a temperature 98 K, just below the range of our measurements, but still within reason.

McKee *et al.,* 2003 indicates that for turbulent core accretion models, the stellar formation time is weakly related to the mass of the source, $t_{*f} \propto m_{*f}^{1/4}$. This produces time-scales on the order of 1.6-2.4x10^4 yrs for our sample.

Finally, studies show dynamical timescales are of the same order of magnitude as the free-fall timescale (Beuther *et al.,* 2002, Li *et al.,* 2019), although Tan *et al.,* 2014 states dynamical timescales are several times the mean free-fall timescale. For a quick comparison, we determined the free-fall timescale, given by equation 4.1.

$$t_{ff} = \sqrt{\frac{3\pi}{32G\rho}} \tag{4.1}$$

Here ρ is the average gas density, which is determined from the average volume density in table 3.3.

Values of dynamical timescales were found in literature, mass relation, and free-fall timescale in comparison to the chemical model fitted timescales are shown in Table 4.2 below.

The summary of these results indicates that likely all of the sample are a product of a fast warm-up model. Dynamical timescales and mass timescales are almost all on the order of 2.0x10^4 yr, corresponding to the Allen fast warm-up model, with the possible exception of G37. While the Garrod medium warm-up phase allows for higher temperatures, it seems unlikely timescales of that length produce high-mass stars. Further investigation is needed to determine whether this is a result of overestimated temperatures or of initial conditions that are not relevant for our sample. Our results also agree with Tan *et al.,* 2014 with free-fall times several factors lower than the evolution timescale. This is seen in Figure 4.2. Here dynamical timescales from Table 4.2 are plotted against the free-fall timescale. When no dynamical timescale is available (i.e. for AFGL 4176 and G34.43), the mass relation timescale is used. For the sources that have a range of dynamical timescales, the median point was used.

Table 4.2: Comparison of Evolutionary Time-scales

Source	t_{model} [1]	t_{dyn} [2]	t_{mass} [3]	t_{ff}
	10^4 yr	10^4 yr	10^4 yr	10^4 yr
AFGL 4176	2.5	-	2.3	1.1
G23.01	19	2.0[4]	2.0	0.4
G24.78	21	1.8-2.4[5]	2.1	0.7
G29.96	2.2	0.3[6]	2.4	0.6
G34.43	19	-	1.9	0.4
G35.03	2.3	1.3-1.6[7]	1.7	0.5
G35.20	19	0.5-1.1[8]	1.8	0.3
G37.55	2.3	7.5[9]	2.2	2.6

Notes: [1]Values determined from chemical models
[2]Ranges are given to sources with multiple outflows, with varying timescales.
[3]Value determined from timescale-mass relation of Tan *et al.,* 2014
[4]Value from Sanna *et al.,* 2016
[5]Value from Beltrán *et al.,* 2011c
[6]Value from Beltrán *et al.,* 2011a
[7,8]Values from Allen *et al.,* 2017
[9]Value from Beuther *et al.,* 2002

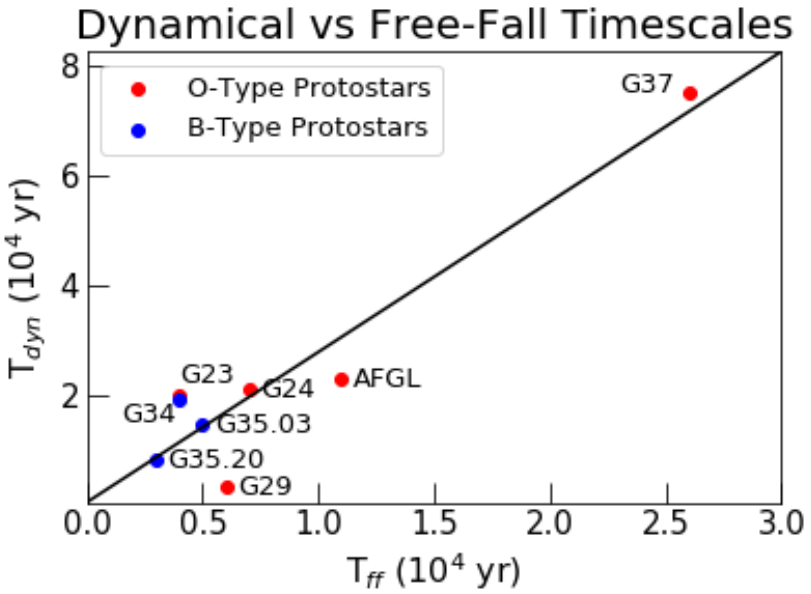

Figure 4.2: Free-fall timescale vs. dynamical timescale. Red points represent O-type protostars, while blue dots represent B-type protostars. The solid line is the linear fit of the sample.

The relationship produced is fairly linear, with t_{dyn} greater than t_{ff} by a factor of 2.5, with the lowest mass protostars at the low end of the relationship. The exception is G29, with a t_{dyn} a factor of 5 below the other O-type protostars. However, this plot may indicate that the mass of G29 has been overestimated, which is certainly plausible; the mass estimate for G29 is based on the PV plot, which can be overestimated if it is a binary system. It can also be noted that our timescale determined from chemical models for G29 would be a closer fit to the relation. G37 has the longest evolutionary timescale, and still fits well with the relation. Thus it may be possible to use the free-fall timescale to determine the evolutionary timescale of the protostar. This plot also corroborates predictions made for our sample; G23 and G35.20 appear to the youngest of the O and B-type stars, respectively, as they were predicted to be in the early stages of Keplerian rotation. Similarly, AFGL 4176 and G35.03, who show strong evidence of being in Keplerian rotation, are more evolved O and B-type sources. Another noteworthy trend is that it appears that evolutionary timescales are different between O-type and B-type stars. In general, O-type stars have longer timescales, such as the cases mentioned above: AFGL and G35.03 are of the same structure, but the larger O-type protostar of AFGL has a greater timescale. Same can be said for the young protostars of G23 and G35.20. The young O-type protostar G23 has a timescale similar to that of a more evolved B-type star (e.g. G34).

Furthermore, the two sources that used the McKee *et al.,* 2003 mass relation are clustered near the linear fit as well, indicating that this relation may provide realistic warm-up timescales. Thus, for the four sources that have the likely unrealistic warm-up scale on the order of 200 Kyr (G23, G24, G34 and G35.20), the mass

relation value is determined as the accepted evolutionary timescale instead.

4.2 Classification of the Sample

From the discussion above, a classification of the sample is made, in order to determine the true nature of the structures surrounding the protostars.

Stable, flared disk in Keplerian rotation

1. AFGL 4176 (O-type)
2. G35.03 +0.35 (B-type)

Marginally stable, flared disk in initial stages of Keplerian rotation

1. G23.01 -0.41 (O-type)
2. G35.20 -0.74N A (B-type)

Unstable, flat disk in final stages of Keplerian rotation

1. G34.43 +0.35 MM1 (B-type)

Unstable, flared disks experiencing fragmentation

1. G24.78 +0.08 A1 (O-type)
2. G24.78 +0.08 A2 (O-type)

Marginally stable, expanding flat/ambiguous structure

1. G37.55 +0.20 (O-type)

Unstable, flat structure with outflow rotation

1. G29.96 -0.02 (O-type)

It is interesting to note that several classifications contain both O and B-type stars, suggesting the two subsections are susceptible to the same evolutionary sequence. This is a positive sign that O-type stars also form Keplerian-like disks. B-type stars have been more successful in Keplerian disk detections, thus a link between the two sub-samples is noteworthy. Of the O-type stars, only AFGL and G23.01 show strong signatures of Keplerian rotation, while all three B-type show strong or partial Keplerian rotation (G35.03, G35.20 and G34.43). G24.78, G29.96 and G37.55 show minimal Keplerian rotation signatures, and any rotational evidence is most likely due to outflows/expansion.

4.3 Mass Selection Criteria

For several calculations, such as Toomre Stability and Kepler velocities, a single mass must be used for stellar mass. Below lists the criteria for which mass was selected, and the final masses:

1. Luminosity and dynamical masses agree, use luminosity value.
   (a) AFGL 4176: 27 $M_\odot$
   (b) G34.43: 12 $M_\odot$
2. Dynamical value agrees within luminosity upper limit, use dynamical value.
   (a) G24.78A: 18 $M_\odot$
   (b) G29.96: 34 $M_\odot$
   (c) G35.03: 8 $M_\odot$
   (d) G35.20: 10 $M_\odot$
3. Dynamical mass overestimated, use luminosity mass.
   (a) G23.01: 16 $M_\odot$
   (b) G37.55: 24 $M_\odot$
4. Dynamical mass overestimated, luminosity only provides upper limit, use value from literature
   (a) G24.78 A1: 22 $M_\odot$ (Beltrán *et al.,* 2011b)

4.4 Uncertainties of the Analysis

Several uncertainty factors must be taken into consideration when interpreting the results of this thesis. For LTE analysis, as mentioned in Section 2.4.1, population diagrams are at risk of overestimation of temperatures and underestimation of column densities. It was often the case, particularly in the hotter sources, the peak temperatures were higher than what was reported in the literature, and to have errors in excess of 50%. Hence, some reservation must be taken in assessing these values. Furthermore, population diagrams are more accurate with more available K-lines. In the available spectra, at most 10 lines are available, and in some cases as few as 4. Obtaining K-ladders from other J-transitions would remove some degeneracies, but this is not always possible for every source, it heavily depends on the data available in the ALMA archive.

In some cases, CH_3CN emission lines were blended with other species, or even with other CH_3CN K-lines. For example, K=0 and 1 were often found to be blended together. While attempts were made to obtain accurate intensities from the blended lines, it cannot be ignored that this may have had an effect on the results.

Intensities derived from blended lines may have similar consequences in non-LTE methods, particularly during the χ^2 fitting. If a measured intensity is higher than reality, the χ^2 will fit it with a similarly high modelled intensity, producing higher temperatures, column densities, etc. Overall, the peak temperatures in non-LTE were more conservative, and likely to be less effected.

A final uncertainty that has already been touched upon, involves determining the disk mass. The disk mass error in Table 3.4 is based of the flux error, however, other sources of error include assumed dust temperatures and dust opacities. We have assumed dust temperatures to be equal to the gas temperatures. While this is expected for LTE scenarios such as dense regions around a protostar, Koumpia *et al.,* 2015 found gas temperatures to be 5-15° warmer even in dense regions. Thus some uncertainty remains in this regard. The greatest source of uncertainty comes from the definition of the outer edge of the disk. In this thesis, the disk is represented by the 10% peak continuum contour, for consistency across all sources. G37 represents a useful example of the caution needed in taking this into account. With our current definition of disk radius, G37.55 disk mass is 17 $M_{\odot}$. But CH_3CN does not trace the entire contoured area. If we assume the disk is the area traced by the molecule, this mass is reduced by a factor of a half. This is object dependent though, as in G34, who's disk mass is potentially greater than that of the stellar mass. Reducing the radius to the 30% contour only reduces the mass by 20%, and still results in a disk mass equal to that of stellar mass. We are satisfied with our definition of disk area, but a more consistent approach is worth investigation.

4.5 Analysis comparison to AFGL 4176

As mentioned in Section 3.8, AFGL 4176 represents a curious case where the ALMA archive data provided only a partial spectrum of CH_3CN, excluding the K = 0-4 lines. These lines are particularly crucial for tracing cooler gas. However, since the goal of this thesis is to determine disk properties, which are usually higher densities and temperature, the higher K-lines provided may still allow for accurate results. To determine the accuracy of AFGL's physical properties, a comparison was made with two other sources; G34.43 and G35.03. G35.03 was selected as it is similar to AFGL in terms of temperature and density structure. In contrast, G34.43 has a higher temperature and density profile. There were no other 13-12 J-transitions amongst the sample, so both sources represent two other J-transitions (J=12-11 and J=19-18, for G34 and G35.03, respectively). For both sources four consecutive K-lines were chosen that mirrored the temperature range presented by AFGL (258 - 537 K). Table 4.3 presents the results of the analysis.

Table 4.3: Comparison of peak values of full spectrum and partial spectrum analysis of G34.43 and G35.03.

	G34.43		G35.03	
CH_3CN Transitions	J = 12-11, K=5-8		J = 19-18, K=4-7	
E_u Range (K)	247 - 525		282 - 517	
	Full	Partial	Full	Partial
LTE Temp (K)	764	1000+	382	405
non-LTE Temp (K)	600	200	460	420
LTE Col Dens (10^{16} cm^{-2})	4.1	40	0.4	0.7
non-LTE Col Dens (10^{16} cm^{-2})	2.0	9.0	0.9	1.0
H_2 Vol Dens (10^6 cm^{-3})	1.0	1.0	0.9	1.0

The analysis results in two scenarios on opposite ends of the spectrum. G34.43 is severely effected by the partial spectrum analysis. The LTE population diagrams produces peak temperatures well above 1000 K. As mentioned in the physical properties section, hotter sources such as G34 suffer from overestimation effects in temperature from the population diagrams. This effect is further enhanced in this scenario. The effect is noticeable in column densities as well, peaking at 4.0x10^{17} cm^{-2}, a magnitude higher than any column densities measured in the sample. The non-LTE analysis was also strongly affected, but in the opposite regard. Estimated temperatures were lower than the full spectrum analysis, peaking at less than half the original value. G34.43 clearly proves that only including higher K-lines can strongly skew analytical results.

Alternatively, G35.03 presents the opposite case of G34.43. It displays results in agreement with the original analysis, in both LTE and non-LTE scenarios for both temperature and column density.

A final alteration that occurs with the limited spectrum is the reduction of data points. Many data points that trace the cooler region of the edges of the disks are lost, as they lack sufficient, or do not contain any, higher K-lines. This is not an issue for a source such as G34, where the CH_3CN traces beyond our definition of the disk edge, but could be an issue for G35.03, which loses its outside data points.

With this comparison complete, can we accept the data provided by AFGL 4176? It clearly shows that choosing the right K-ladder is vital for determining properties in these methods. It also shows the results depend heavily on the particular source. However, the case of G34 suggests that faulty data would present as inflated, unrealistic variations between the LTE and non-LTE methods. As AFGL has agreeing property estimations in both LTE and non-LTE analysis, this indicates the results are reasonably close to the true values, as in the case of G35.03. Although this means that the radius of gas traced by CH_3CN is less than it is in reality, this is not an issue for our analysis, as the data points available still cover the area of the disk. For these reasons, the data for AFGL 4176 is chosen to

be included in this study. Further analysis is still highly recommended, either by obtaining the entire spectrum, or by using previously mentioned programs such as XCLASS or CASSIS.

Chapter 5

Conclusions

5.1 Summary and Conclusions

This thesis presents measurements of the properties and structures around nine high-mass protostars. Below are the results of each source. With open questions regarding to the formation process of high-mass stars, we utilized ALMA archive data to determine the kinematics, structure, stability, and property distribution of eight high-mass star forming regions, encompassing nine high-mass stellar objects studied in total. A classification is made for the structures, to determine if there are disks around high-mass stars, and if they are in Keplerian rotation.

- **AFGL 4176** is an O-type protostar of 27 $M_{\odot}$ with a disk mass of 3 $M_{\odot}$. It displays strong signatures of Keplerian rotation around a stable, flared disk. Temperatures peak at 383 K and CH_3CN column densities at 3.0x10^{16} cm^{-2}. CH_3CN abundances peak at 2.5x10^{-8}, and the source has a chemical age of 25 Kyr.
- **G23.01 -0.41** is an O-type protostar in the range of 16-26 $M_{\odot}$ with a disk mass of 5 $M_{\odot}$. It is surrounded by a marginally stable, flared disk, with moderate signatures of Keplerian rotation. G23.01 is possibly a young protostar in early stages of Keplerian rotation, with infalling gas still occurring as well. Temperatures peak at 610 K and CH_3CN column densities at 2.2x10^{16} cm^{-2}. CH_3CN abundances peak at 3.0x10^{-9}, and the source has a chemical age of 20 Kyr.
- **G24.78 +0.08** contains two O-type protostars of 22 $M_{\odot}$(A1) and 18 $M_{\odot}$(A2), with a disk masses of 12 $M_{\odot}$ and 15 $M_{\odot}$, respectively. Both cores display unstable flared disks possibly experiencing fragmentation and formation of binaries. A1 has rotation most likely due to outward expansion, and A2 does not display rotation signatures. Both cores are hot, peaking at 700+ K, and column densities in excess of 5x10^{16} cm^{-2}. CH_3CN abundances peak at 3.0x10^{-8} for both A1 and A2, while the region has a chemical age of 21 Kyr.

- **G29.96 -0.02** is an O-type protostar of 34 $M_\odot$ with a disk mass of 24 $M_\odot$. It is surrounded by an unstable, flat structure, most likely an outflow. G29.96 is likely a more evolved protostar, with multiple smaller protostars in the vicinty. Temperatures peak at 696 K and column densities at 7x10^{16} cm^{-2}. CH_3CN abundances peak at 1.5x10^{-8}, while the source has a chemical age of 22 Kyr.
- **G34.43 +0.24 MM1** is a B-type protostar of 12-18 $M_\odot$ with a disk mass of 15 $M_\odot$. The structure surrounding the source is flat, and of the same mass or larger, and thus highly unstable. Marginal rotation signatures, combined with instability indicate it is likely evolved past its stable Keplerian rotation phase and is now in the midst of forming spiral arms. It contains a hot core with temperatures peaking at 764 K and column densities at 4.1x10^{16} cm^{-2}. CH_3CN abundances peak at 8.0x10^{-9}, while the source has a chemical age of 19 Kyr.
- **G35.03 +0.35** is a B-type protostar of 8 $M_\odot$ with a disk mass of 0.6 $M_\odot$. It has a stable, flared disk with strong signatures of Keplerian rotation. Temperatures peak at 460 K and column densities at 9x10^{15} cm^{-2}. CH_3CN abundances peak at 1.4x10^{-8}, while the source has a chemical age of 23 Kyr.
- **G35.20 -0.74N** is a high-mass star forming region contains one high-mass B-type protostar, and a secondary core with multiple smaller protostars. Core A is of mass 10 $M_\odot$ with a disk mass of 1.2 $M_\odot$, while B constitutes of multiple cores ranging between 1-4 $M_\odot$. Core A displays signatures of a marginally stable flared disk, with moderate signatures of Keplerian rotation, likely a young protostar in initial stages of Keplerian rotation. Core B also shows signatures of rotation but most likely due to an outflow, originating from A. Core B is also unstable, resulting in fragmentation and multiple cores. Core A temperatures peak at 576 K and column densities at 8x10^{15} cm^{-2}, while core B peaks at 360 K and 5x10^{15} cm^{-2}. CH_3CN abundances peak at 2.0x10^{-9} for both A and B, while the region has a chemical age of 18 Kyr.
- **G37.55 +0.20** is an O-type protostar of 24 $M_\odot$ with a disk mass of 17 $M_\odot$. The structure around the core is ambiguous, both in shape and rotation. It is likely an older, expanding structure, however, further investigations with high resolution observations (higher than the 0.99" used in this data) are required to make a determination. Temperatures peak at 420 K and column densities at 1.1x10^{16} cm^{-2}. CH_3CN abundances peak at 6.7x10^{-8}, while the source has a chemical age of 23 Kyr.

5.2 Moving Forward

This thesis is only the tip of the iceberg for determining and classifying disks around high-mass stars. The first step in moving forward is minimizing the uncertainties within the current data (as mentioned in Section 4.4). A follow-up analysis

using programs such as XCLASS to determine temperatures and column densities with the current source population is recommended. Following that, a larger sample size would tell us the relative number of sources for each class. This study alone proves that apparent disks can take many shapes and forms, and additional data would improve the ability in determining what structures surround high-mass protostars. With a larger population, trends would likely be more readily identifiable. Furthermore, the objects that are identified as disks could be compared to their lower-mass counterparts, to determine similarities or differences between the two. A second sample of 5-10 sources would provide a comprehensive overview of disks around high-mass protostars, and determine the distribution of protostellar disks for each classification established in this thesis.

Fortunately, the quality of observational data of these objects has never been higher. ALMA and other high-resolution interferometers have spurred a plethora of studies in high-mass star formation. The list of potential targets is growing (such as G17.64 (Maud *et al.,* 2018,), G31.41, G345.49 and G345.50 (Cesaroni *et al.,* 2017)), thus the data is expected to be available to continue this study further.

This paper uses data from the following ALMA project data sets: 2012.1.00469.S (AFGL 4176), 2013.1.00489.S (G24.78), 2015.1.00600.S (G35.03,G35.20), 2015.1.00615.S (G23.01), 2016.1.01036.S (G29.96, G34.43) & 2016.1.00345.S (G37.55)

Appendix A

Appendix

Appendix A: Source plots, maps and models of remaining 7 sources.

A.1 AFGL 4176 Plots

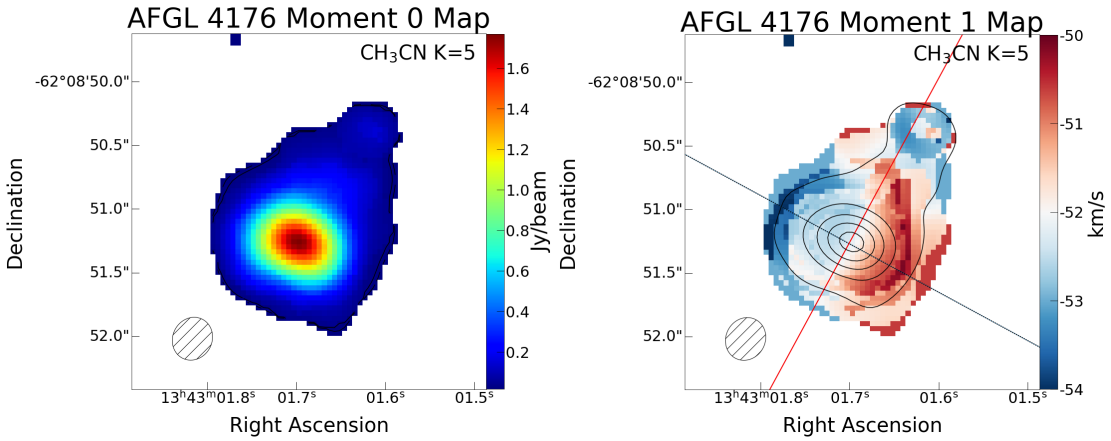

Figure A.1: *Left:* Moment 0 map for AFGL 4176. *Right:* Moment 1 map of AFGL 4176, including PV cut position angle of 62.5° (black line) and approximate outflow direction from Johnston *et al.*, 2015 (red line). Contours in both plots represent 10, 30, 50, 70 & 90 % peak flux.

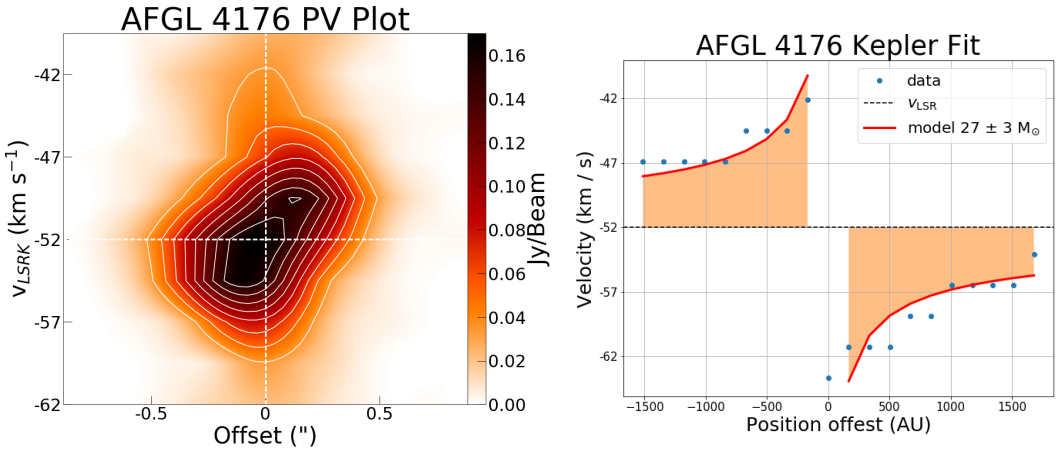

Figure A.2: *Left:* PV diagram of AFGL 4176. Contours represent 20, 30,.. 90 % peak flux. White dashed lines indicate V_{LSR} (horizontal) and central offset position (vertical). *Right:* Seifried Kepler fit of AFGL 4176.

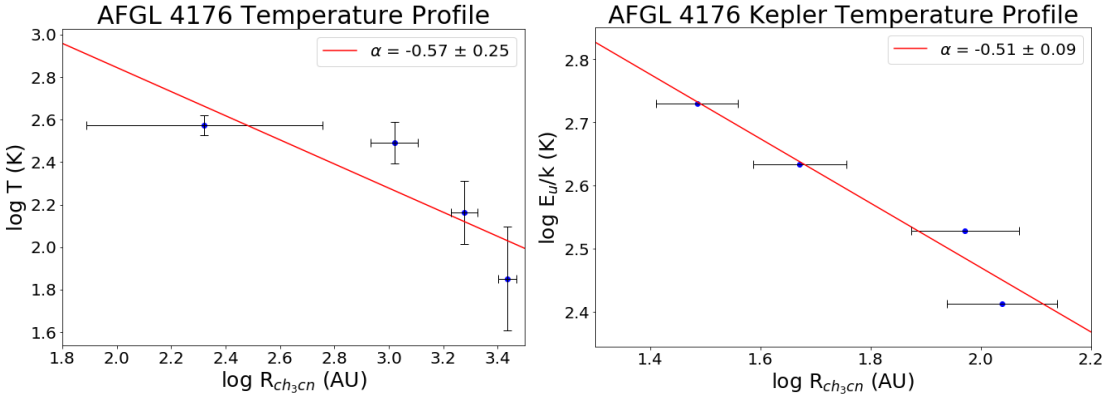

Figure A.3: *Left:* Temperature vs Radius profile of AFGL 4176. *Right:* Temperature profile of AFGL 4176 assuming Kepler rotation.

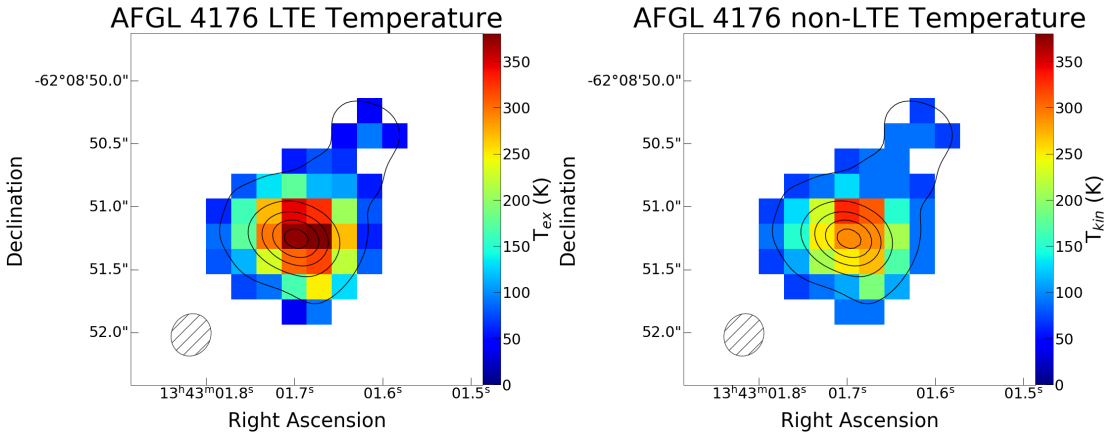

Figure A.4: *Left:* AFGL 4176 LTE temperature map produced by population diagrams. *Right:* Non-LTE temperature map produced by RADEX grids. Contours on both plots represent 10, 30, 50, 70 & 90 % peak flux.

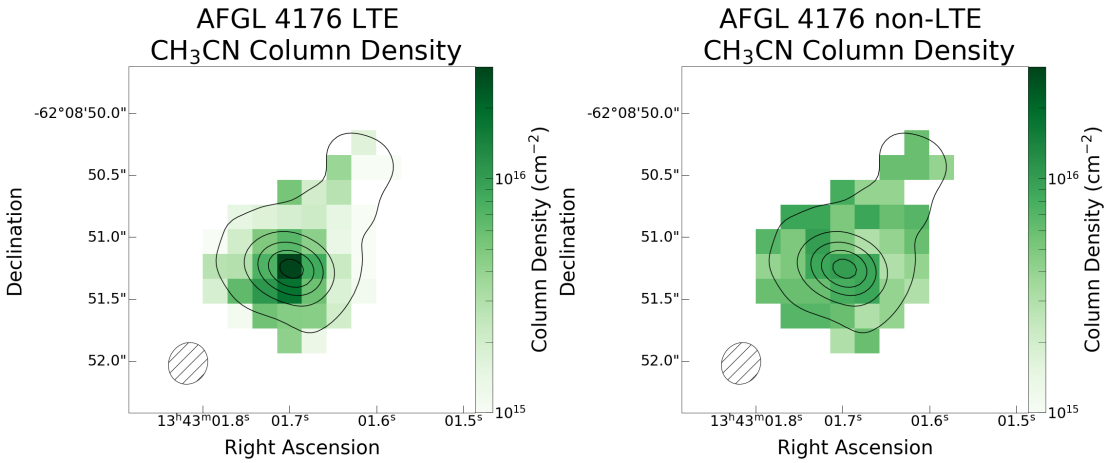

Figure A.5: *Left:* AFGL 4176 LTE CH_3CN column density map produced by population diagrams. *Right:* Non-LTE CH_3CN column density map produced by RADEX grids. Contours on both plots represent 10, 30, 50, 70 & 90 % peak flux.

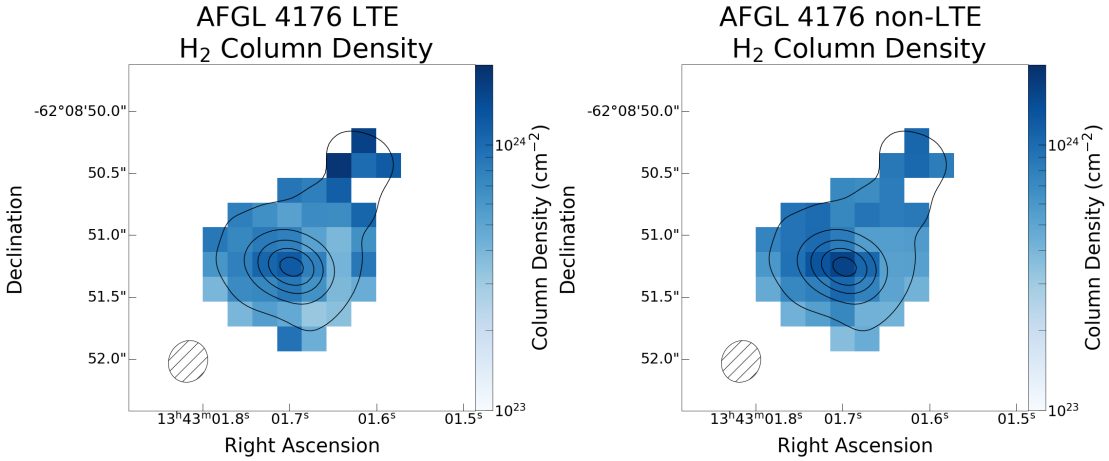

Figure A.6: *Left:* AFGL 4176 LTE H_2 column density map produced from continuum emission, using LTE temperatures. *Right:* Non-LTE H_2 column density map except using temperatures from non-LTE analysis. Contours on both plots represent 10, 30, 50, 70 & 90 % peak flux.

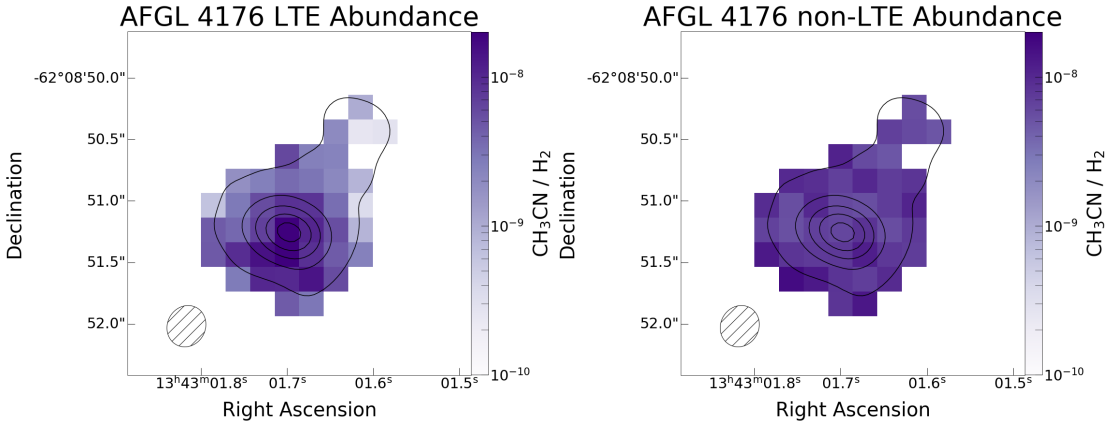

Figure A.7: *Left:* AFGL 4176 LTE abundance map produced from ratio of LTE CH_3CN column density to LTE H_2 column density. *Right:* Ratio of CH_3CN column density to H_2 column density using non-LTE results. Contours on both plots represent 10, 30, 50, 70 & 90 % peak flux.

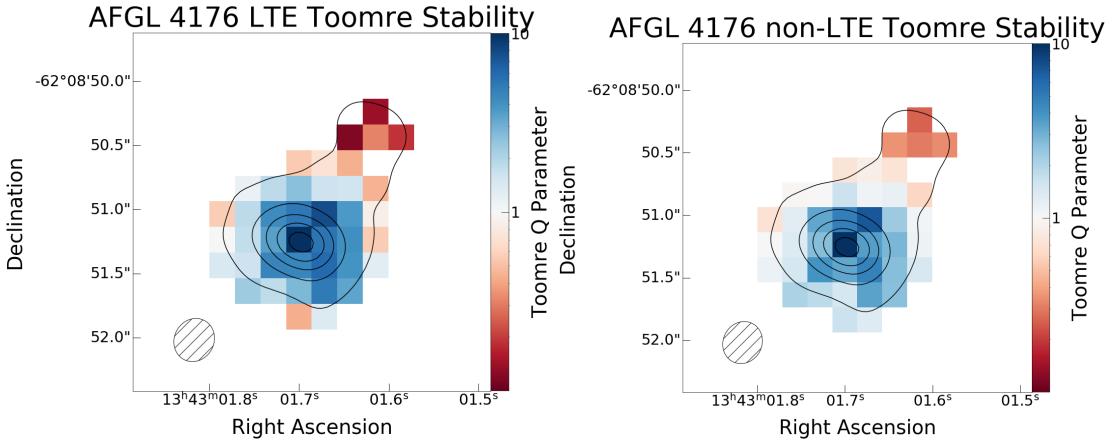

Figure A.8: *Left:* Toomre stability plot of AFGL 4176 using LTE temperatures and H_2 column densities. *Right:* Same as left but with non-LTE parameters. Contours on both plots represent 10, 30, 50, 70 & 90 % peak flux.

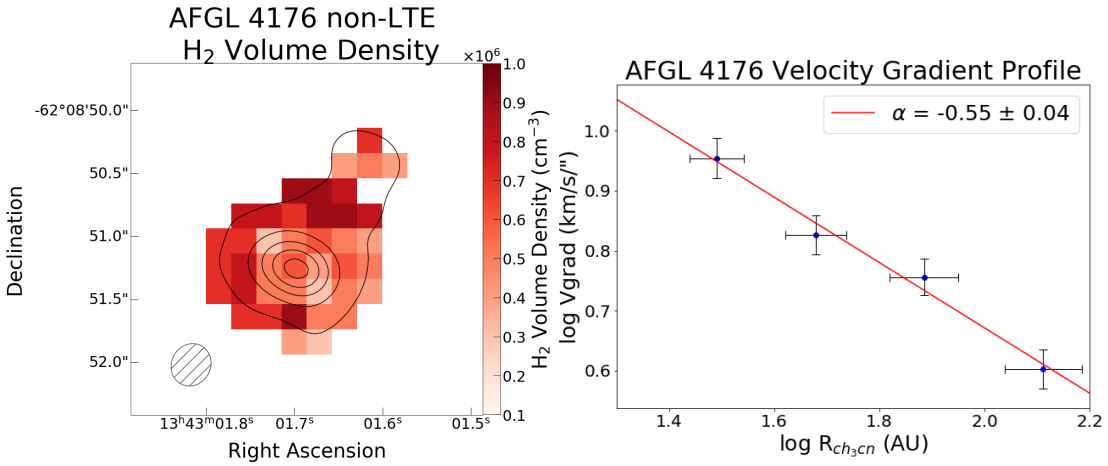

Figure A.9: *Left:* AFGL 4176 H_2 volume density map produced by RADEX non-LTE analysis. Contours on represent 10, 30, 50, 70 & 90 % peak flux. *Right:* AFGL 4176 velocity gradient profile.

A.2 G23.01 Plots

Unused plots of G23.01. Remaining plots can be found in Section 2.

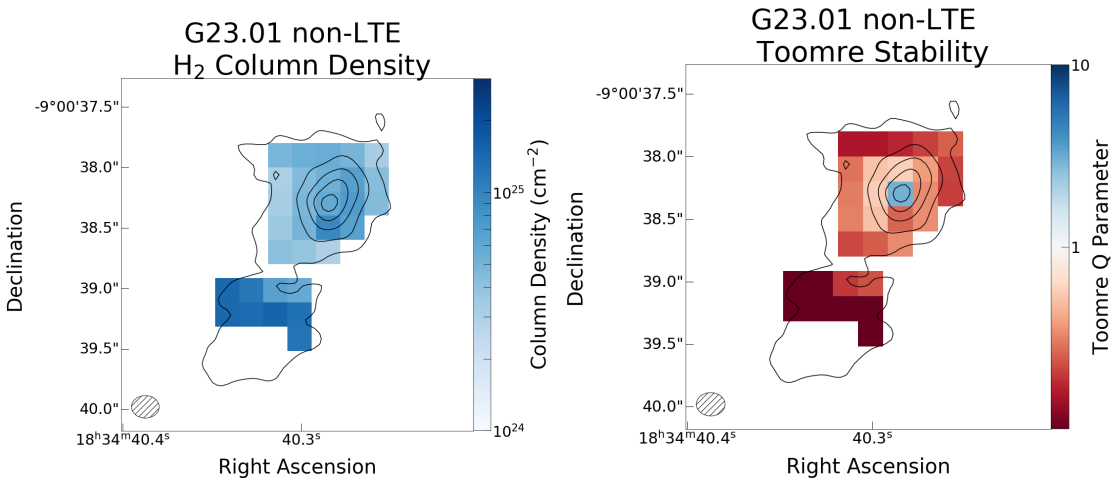

Figure A.10: *Left:* H_2 column densities of G23.01, using non-LTE temperatures. *Right:* G23.01 Toomre Stability plot using non-LTE temperatures. Contours on both plots represent 10, 30, 50, 70 & 90 % peak flux.

A.3 G24.78 Plots

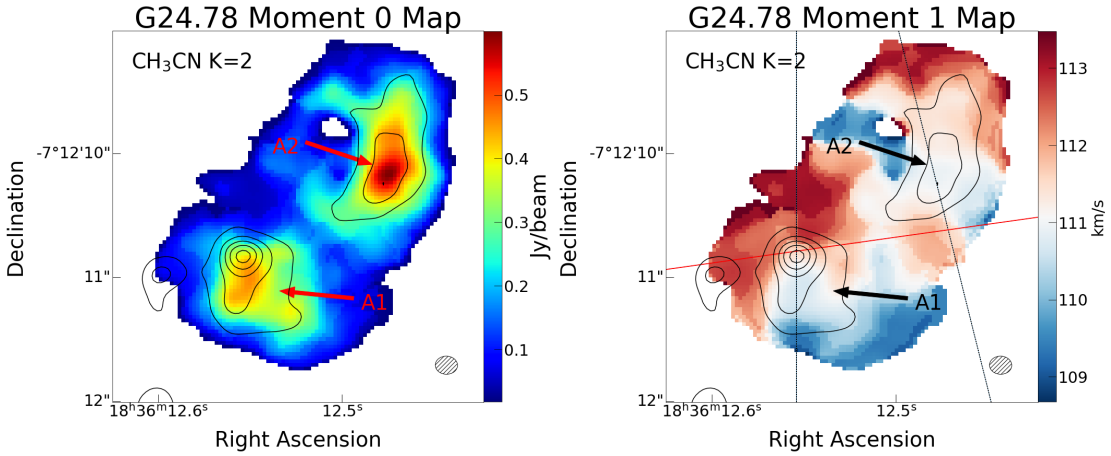

Figure A.11: *Left:* Moment 0 map for G24.78. *Right:* Moment 1 map of G24.78. Black lines are PV cuts for A1 (PA=0°) and A2 (PA=14°). Red line indicates approximate direction of molecular outflow determined by Cesaroni *et al.*, 2017. Contours in both plots represent 10, 30, 50, 70 & 90 % peak flux.

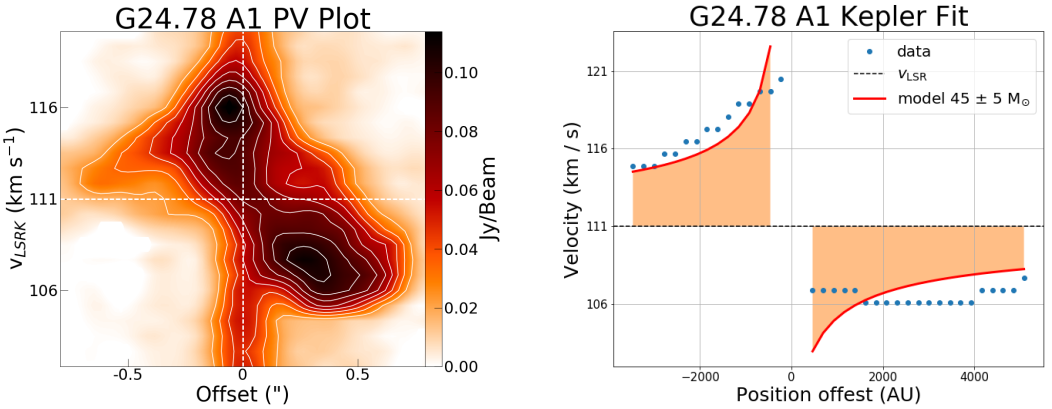

Figure A.12: *Left:* PV diagram of G24.78 A1. Contours represent 20, 30,... 90 % peak flux. White dashed lines indicate V_{LSR} (horizontal) and central offset position (vertical). *Right:* Seifried Kepler fit of G24.78 A1.

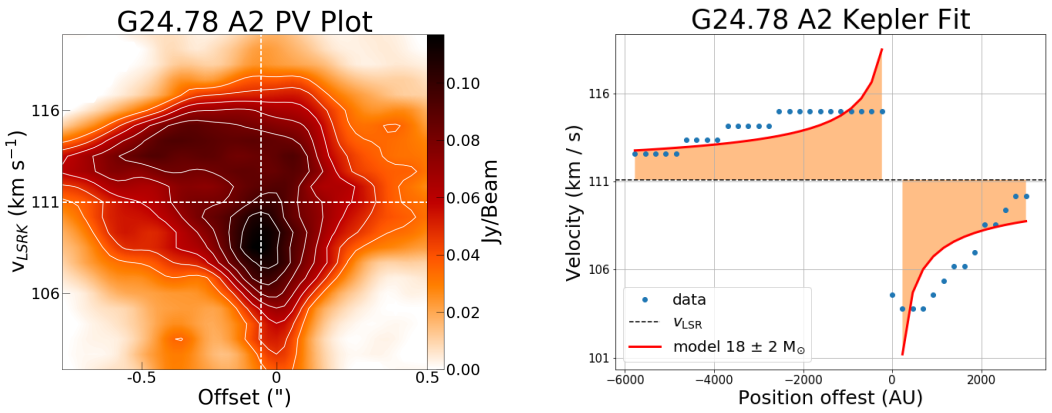

Figure A.13: *Left:* PV diagram of G24.78 A2. Contours represent 20, 30,... 90 % peak flux. White dashed lines indicate V_{LSR} (horizontal) and central offset position (vertical). *Right:* Seifried Kepler fit of G24.78 A2.

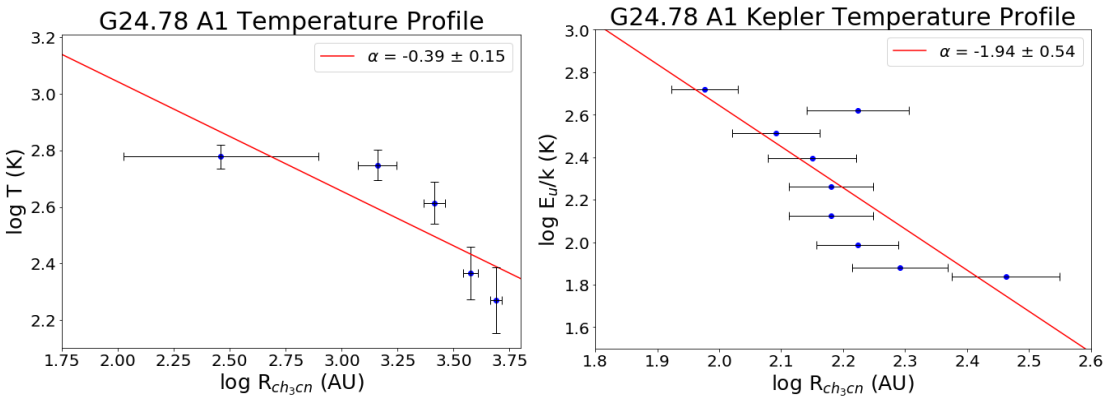

Figure A.14: *Left:* Temperature vs Radius profile of G24.78 A1. *Right:* Temperature profile of G24.78 A1 assuming Kepler rotation.

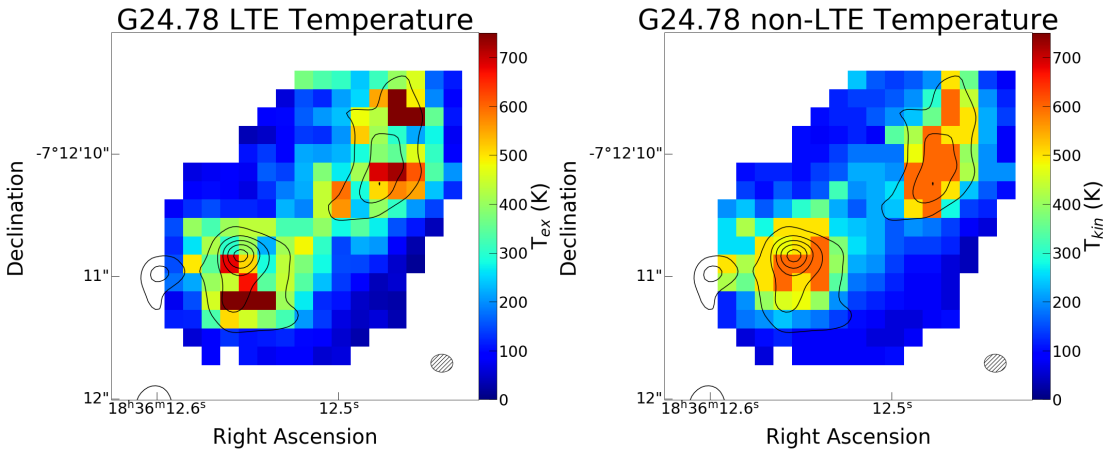

Figure A.15: *Left:* G24.78 LTE temperature map produced by population diagrams. *Right:* Non-LTE temperature map produced by RADEX grids. Contours on both plots represent 10, 30, 50, 70 & 90 % peak flux.

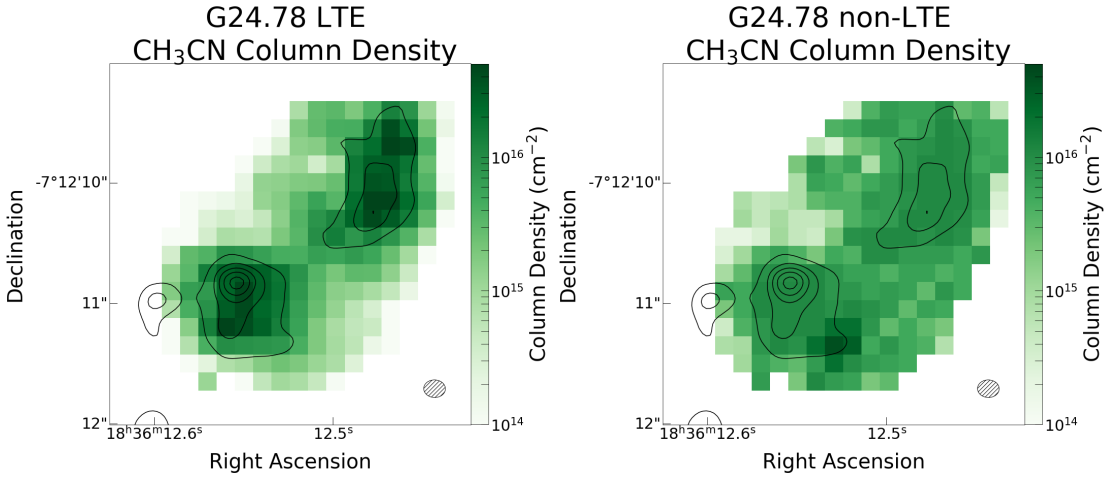

Figure A.16: *Left:* G24.78 LTE CH_3CN column density map produced by population diagrams. *Right:* Non-LTE CH_3CN column density map produced by RADEX grids. Contours on both plots represent 10, 30, 50, 70 & 90 % peak flux.

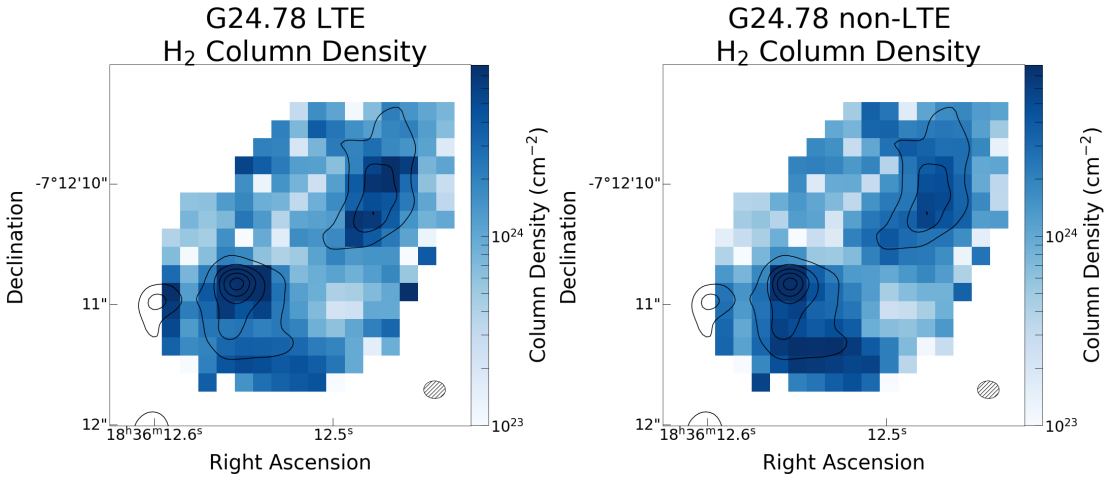

Figure A.17: *Left:* G24.78 LTE H_2 column density map produced from continuum emission, using LTE temperatures. *Right:* Non-LTE H_2 column density map except using temperatures from non-LTE analysis. Contours on both plots represent 10, 30, 50, 70 & 90 % peak flux.

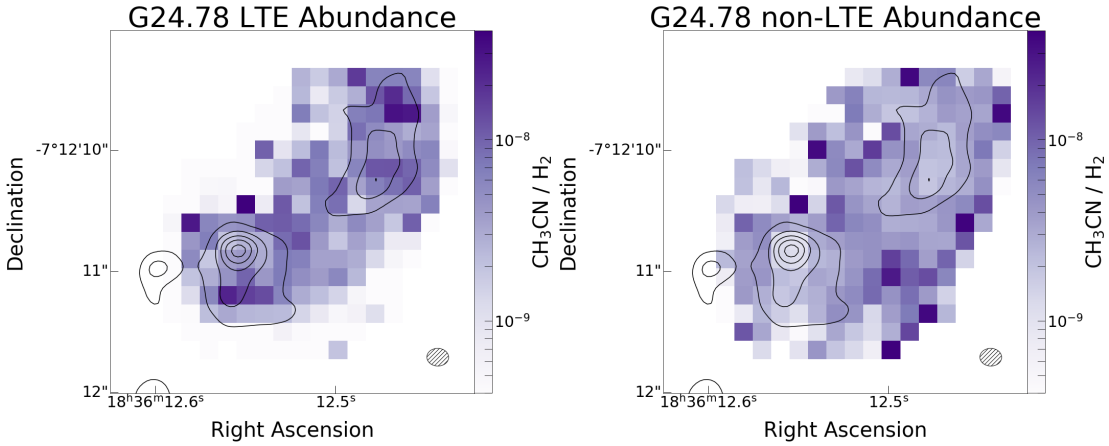

Figure A.18: *Left:* G24.78 LTE abundance map produced from ratio of LTE CH_3CN column density to LTE H_2 column density. *Right:* Ratio of CH_3CN column density to H_2 column density using non-LTE results. Contours on both plots represent 10, 30, 50, 70 & 90 % peak flux.

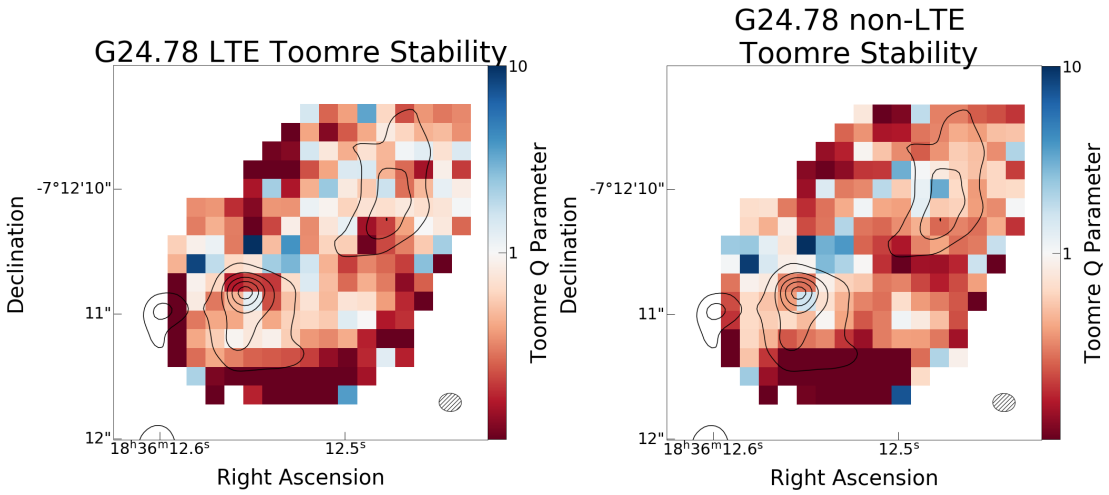

Figure A.19: *Left:* Toomre stability plot of G24.78 using LTE temperatures and H_2 column densities. *Right:* Same as left but with non-LTE parameters.

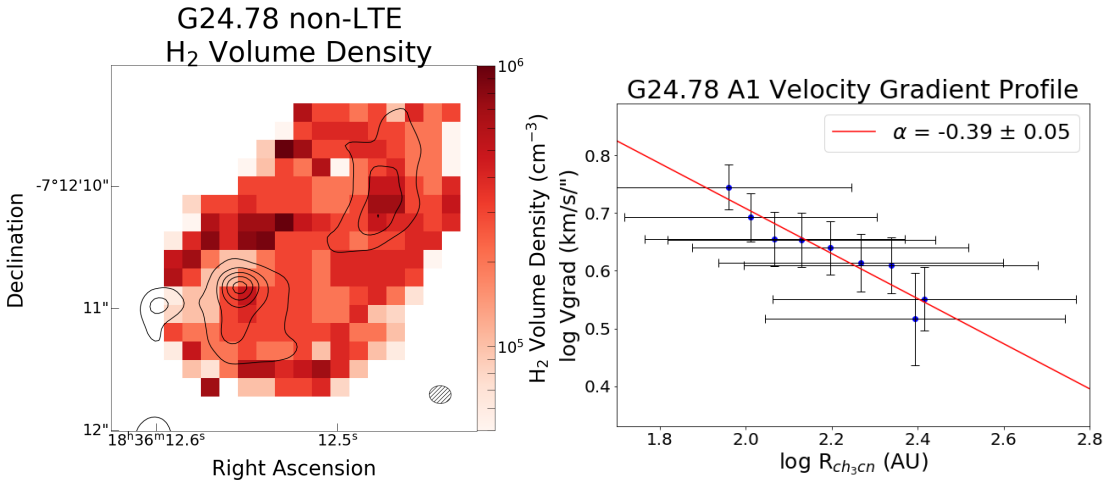

Figure A.20: *Left:* G24.78 H_2 volume density map produced by RADEX non-LTE analysis. *Right:* G24.78 A1 velocity gradient profile.

A.4 G29.96 Plots

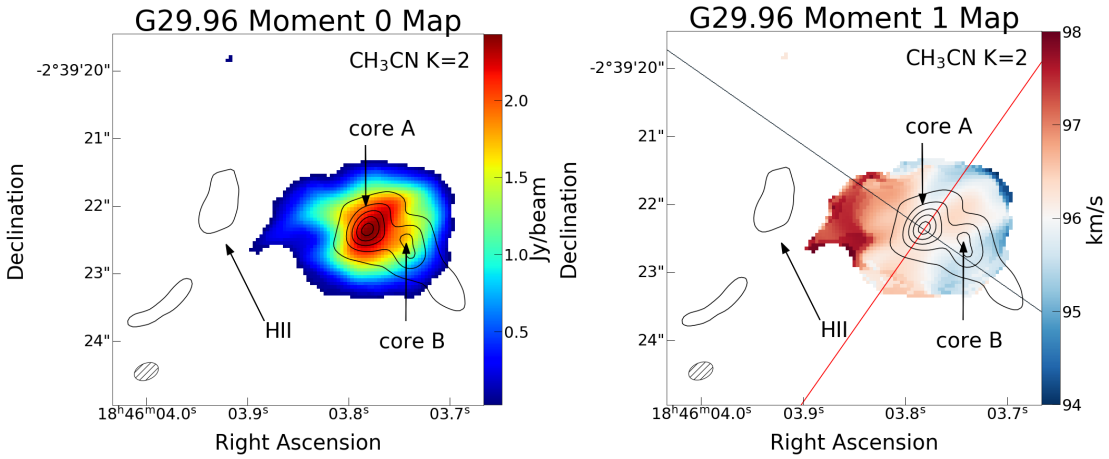

Figure A.21: *Left:* Moment 0 map for G29.96. *Right:* Moment 1 map of G29.96, including pv cut position angle of 55° E of N (black line), and approximate direction of molecular outflow (red line), determined by Cesaroni *et al.*, 2017. Contours in both plots represent 10, 30, 50, 70 & 90 % peak flux.

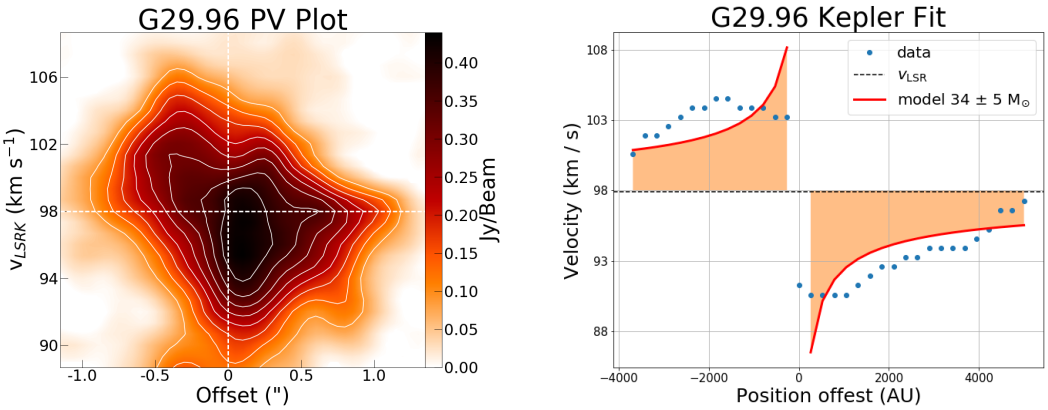

Figure A.22: *Left:* PV diagram of G29.96. Contours represent 20, 30,... 90 % peak flux. White dashed lines indicate V_{LSR} (horizontal) and central offset position (vertical). *Right:* Seifried Kepler fit of G29.96.

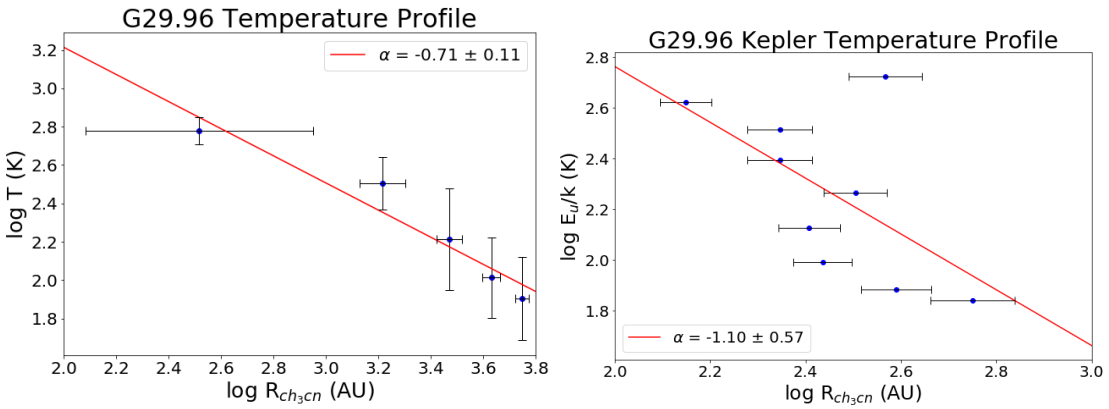

Figure A.23: *Left:* Temperature vs Radius profile of G29.96. *Right:* Temperature profile of G29.96 assuming Kepler rotation.

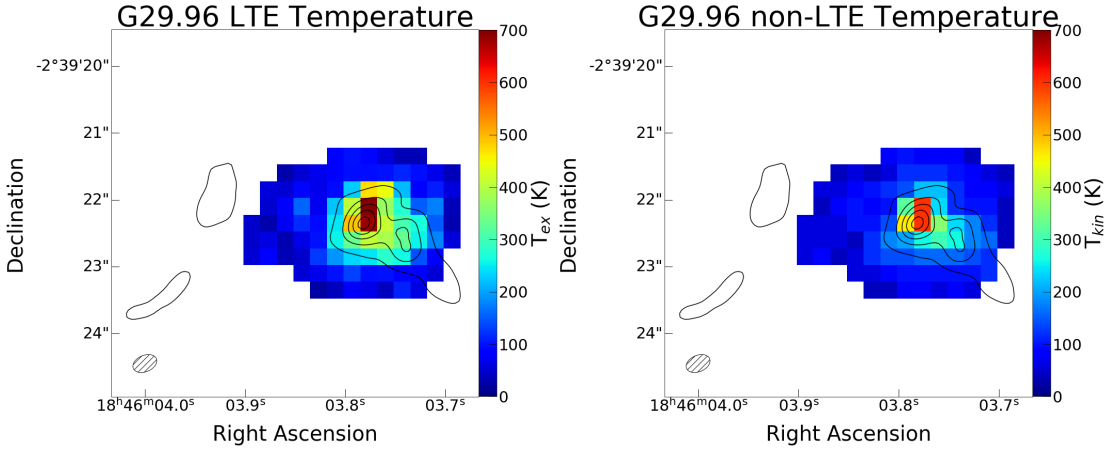

Figure A.24: *Left:* G29.96 LTE temperature map produced by population diagrams. *Right:* Non-LTE temperature map produced by RADEX grids. Contours on both plots represent 10, 30, 50, 70 & 90 % peak flux.

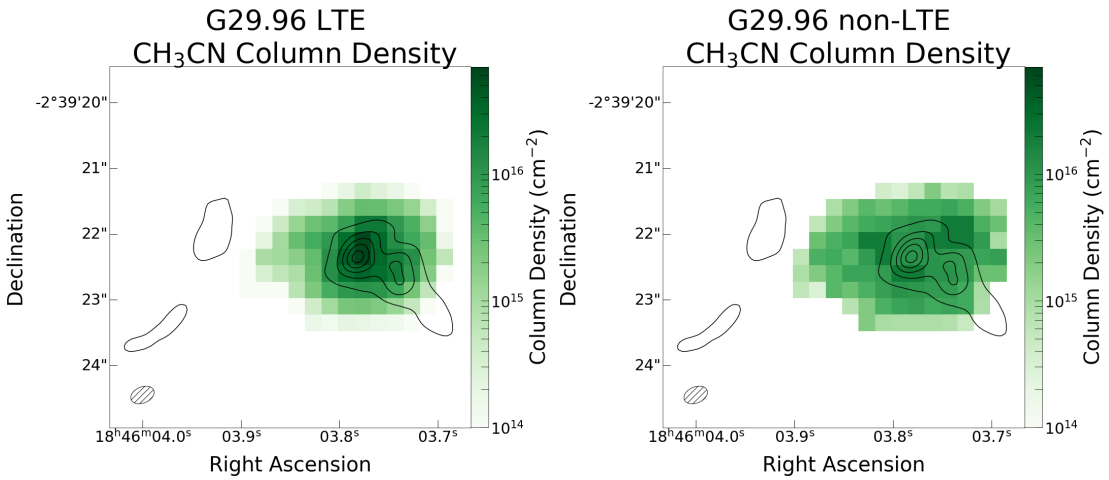

Figure A.25: *Left:* G29.96 LTE CH_3CN column density map produced by population diagrams. *Right:* Non-LTE CH_3CN column density map produced by RADEX grids. Contours on both plots represent 10, 30, 50, 70 & 90 % peak flux.

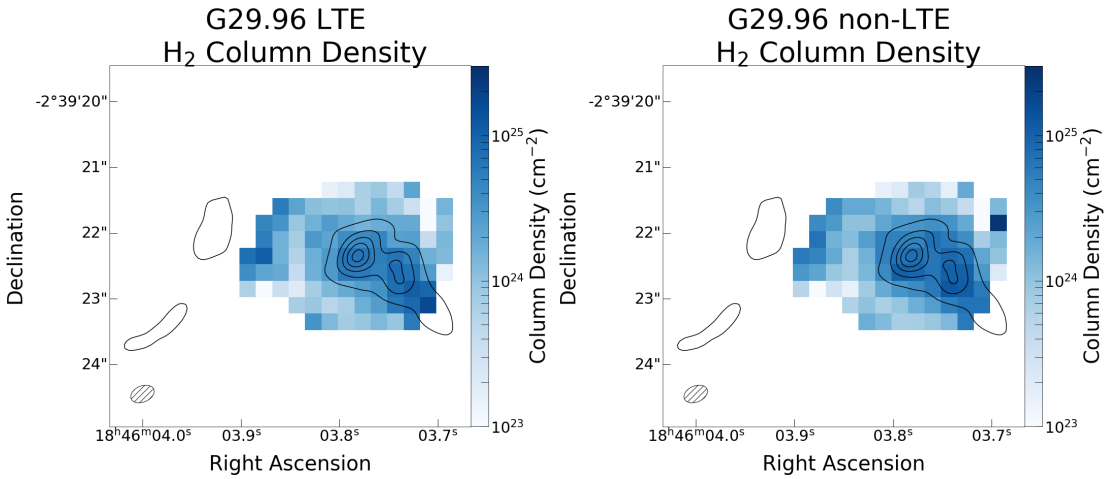

Figure A.26: *Left:* G29.96 LTE H_2 column density map produced from continuum emission, using LTE temperatures. *Right:* Non-LTE H_2 column density map except using temperatures from non-LTE analysis. Contours on both plots represent 10, 30, 50, 70 & 90 % peak flux.

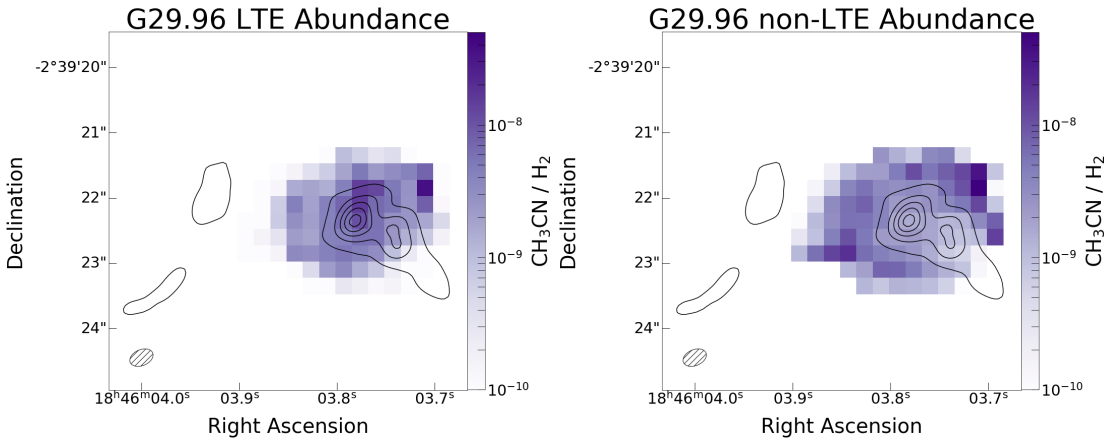

Figure A.27: *Left:* G29.96 LTE abundance map produced from ratio of LTE CH_3CN column density to LTE H_2 column density. *Right:* Ratio of CH_3CN column density to H_2 column density using non-LTE results. Contours on both plots represent 10, 30, 50, 70 & 90 % peak flux.

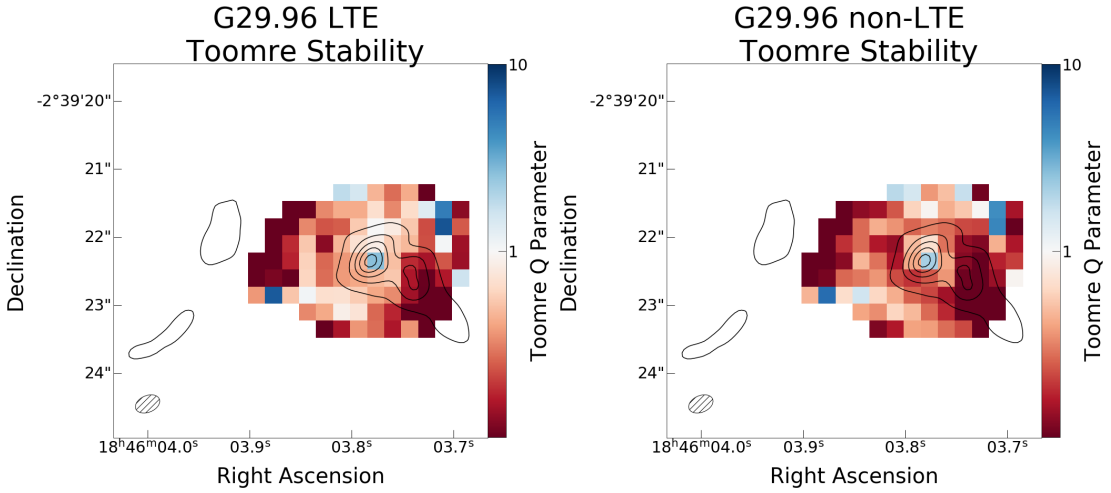

Figure A.28: *Left:* Toomre stability plot of G29.96 using LTE temperatures and H_2 column densities. *Right:* Same as left but with non-LTE parameters.

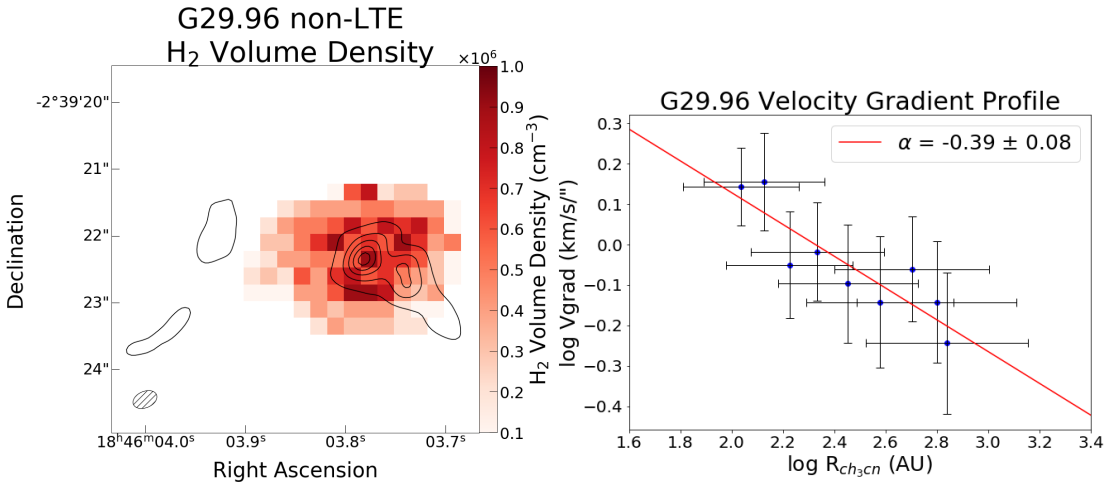

Figure A.29: *Left:* G29.96 H_2 volume density map produced by RADEX non-LTE analysis. *Right:* G29.96 velocity gradient profile.

A.5 G34.43 Plots

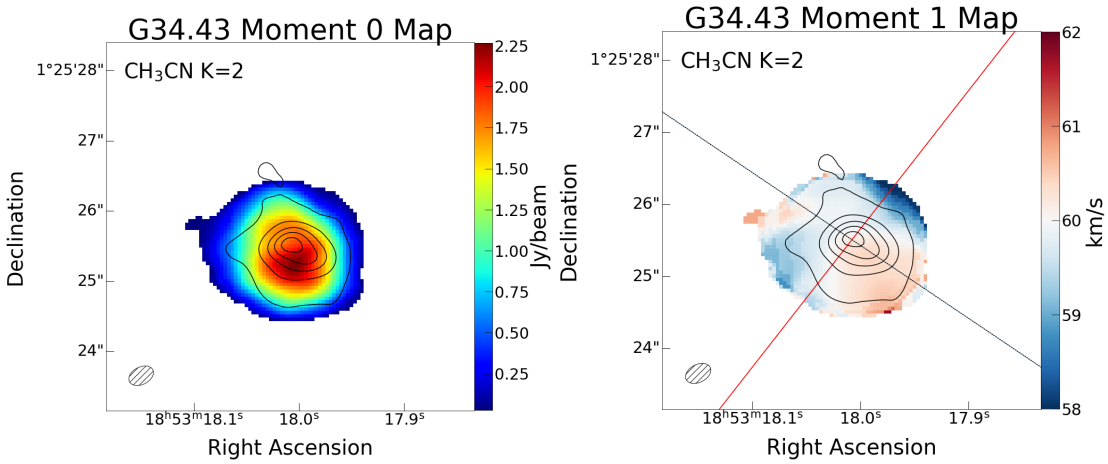

Figure A.30: *Left:* Moment 0 map for G34.43. *Right:* Moment 1 map of G34.43, including PV cut position angle of 55° E of N (black line), and approximate direction of molecular outflow (red line), determined by Shepherd *et al.*, 2007. Contours in both plots represent 10, 30, 50, 70 & 90 % peak flux.

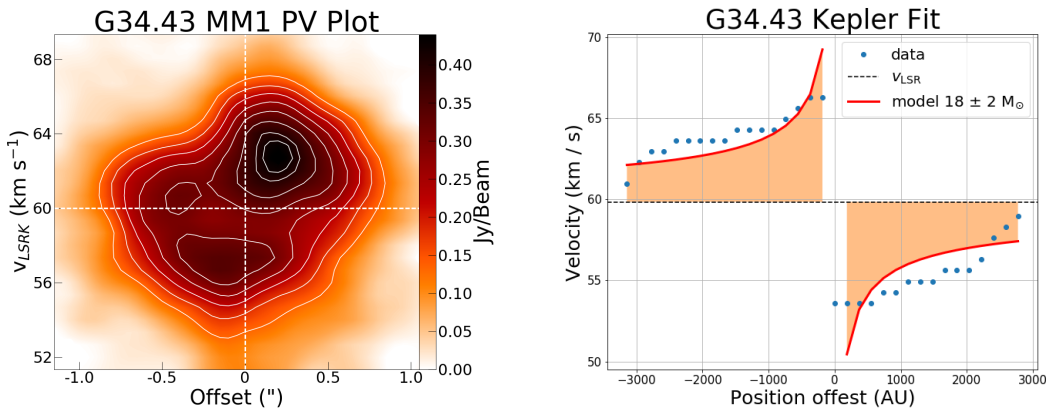

Figure A.31: *Left:* PV diagram of G34.43. Contours represent 20, 30,... 90 % peak flux. White dashed lines indicate V_{LSR} (horizontal) and central offset position (vertical). *Right:* Seifried Kepler fit of G34.43.

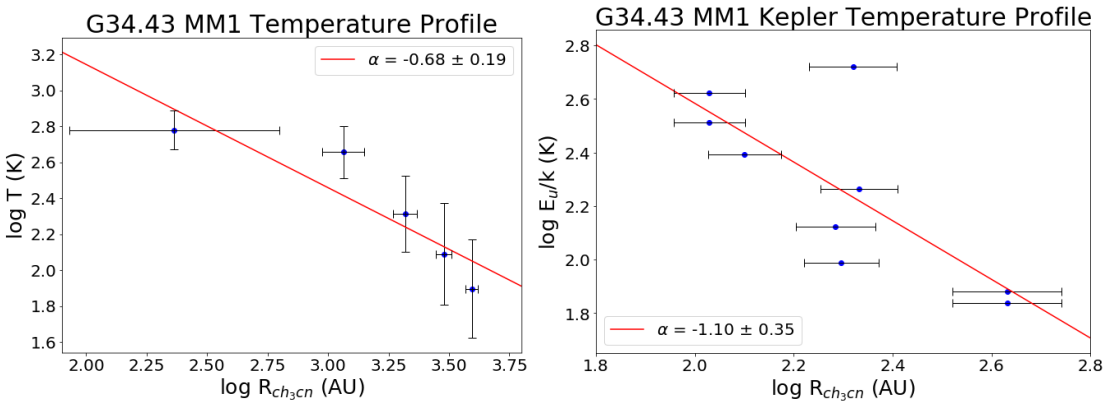

Figure A.32: *Left:* Temperature vs Radius profile of G34.43. *Right:* Temperature profile of G34.43 assuming Kepler rotation.

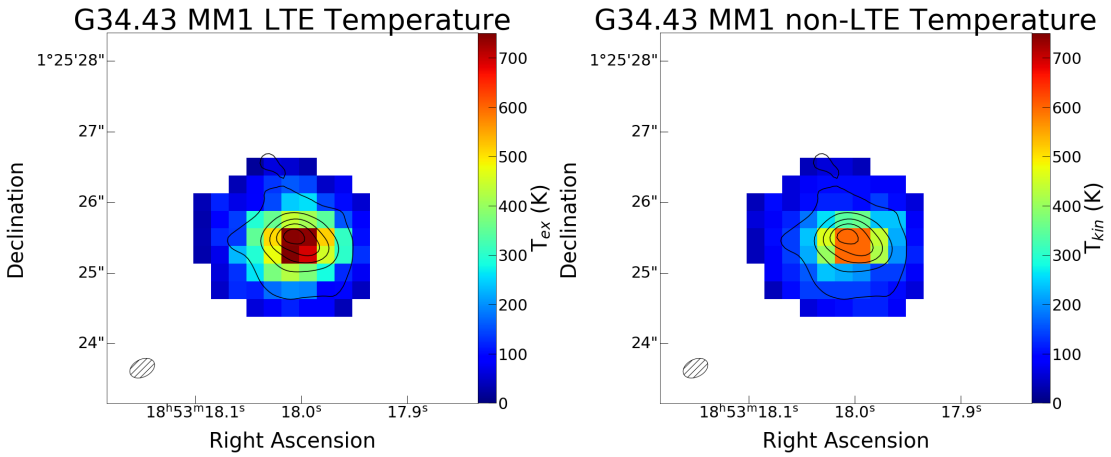

Figure A.33: *Left:* G34.43 LTE temperature map produced by population diagrams. *Right:* Non-LTE temperature map produced by RADEX grids. Contours on both plots represent 10, 30, 50, 70 & 90 % peak flux.

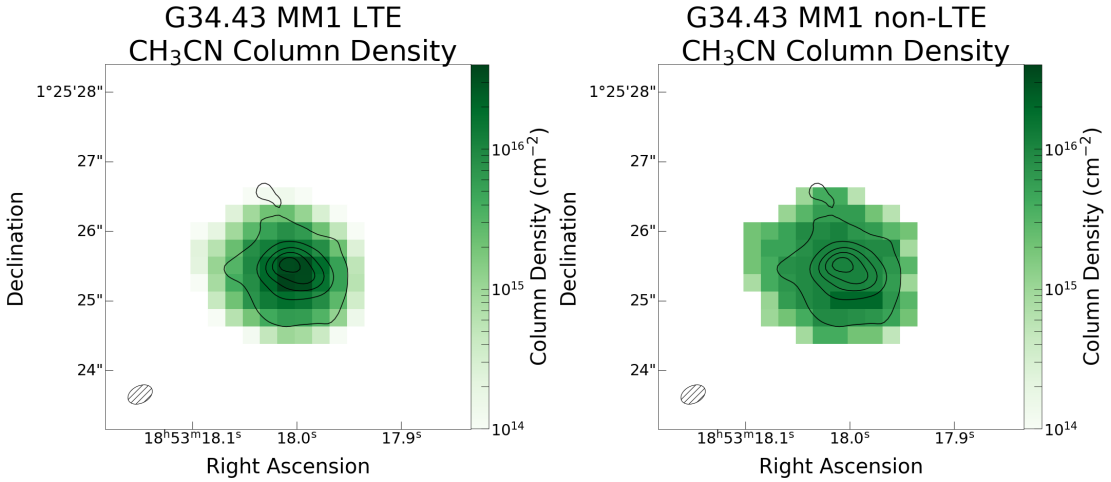

Figure A.34: *Left:* G34.43 LTE CH_3CN column density map produced by population diagrams. *Right:* Non-LTE CH_3CN column density map produced by RADEX grids. Contours on both plots represent 10, 30, 50, 70 & 90 % peak flux.

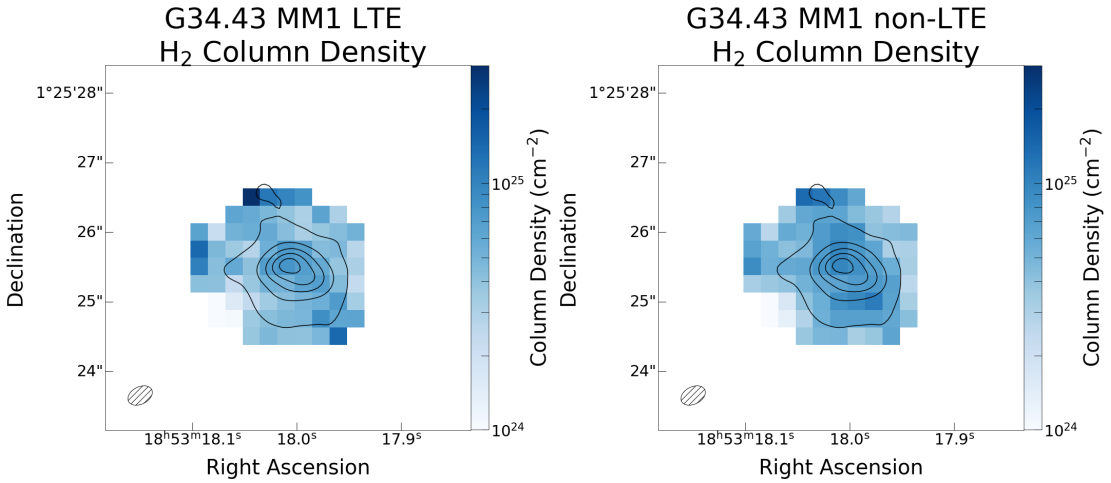

Figure A.35: *Left:* G34.43 LTE H_2 column density map produced from continuum emission, using LTE temperatures. *Right:* Non-LTE H_2 column density map except using temperatures from non-LTE analysis. Contours on both plots represent 10, 30, 50, 70 & 90 % peak flux.

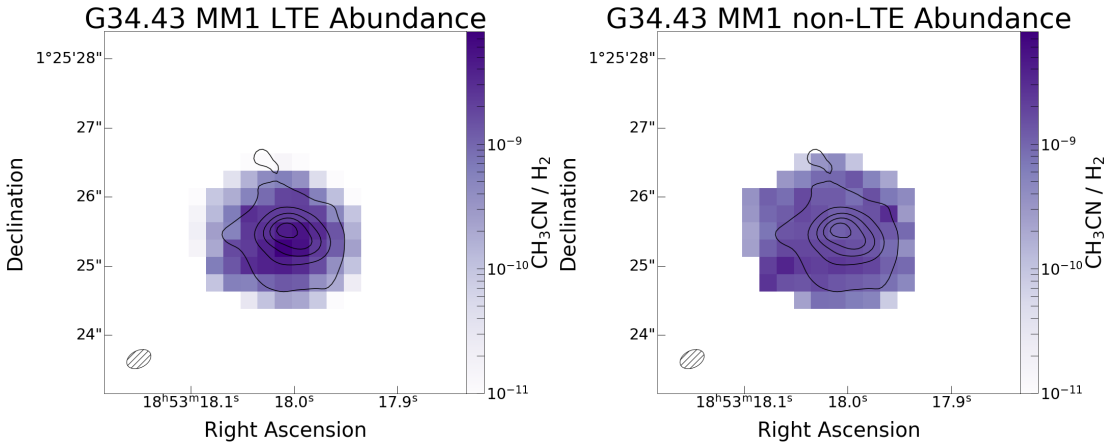

Figure A.36: *Left:* G34.43 LTE abundance map produced from ratio of LTE CH_3CN column density to LTE H_2 column density. *Right:* Ratio of CH_3CN column density to H_2 column density using non-LTE results. Contours on both plots represent 10, 30, 50, 70 & 90 % peak flux.

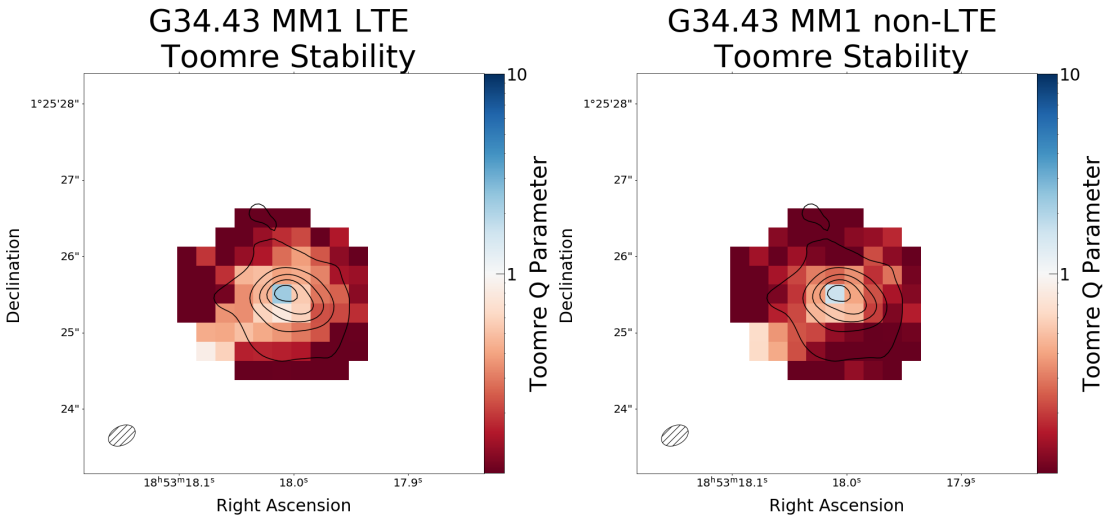

Figure A.37: *Left:* Toomre stability plot of G34.43 using LTE temperatures and H_2 column densities. *Right:* Same as left but with non-LTE parameters.

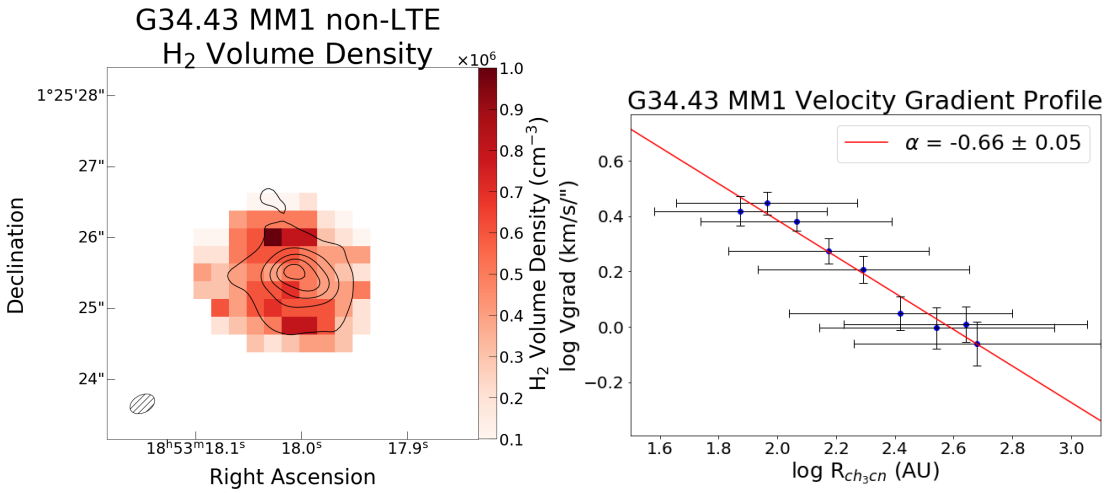

Figure A.38: *Left:* G34.43 H_2 volume density map produced by RADEX non-LTE analysis. *Right:* G34.43 velocity gradient profile.

A.6 G35.03 Plots

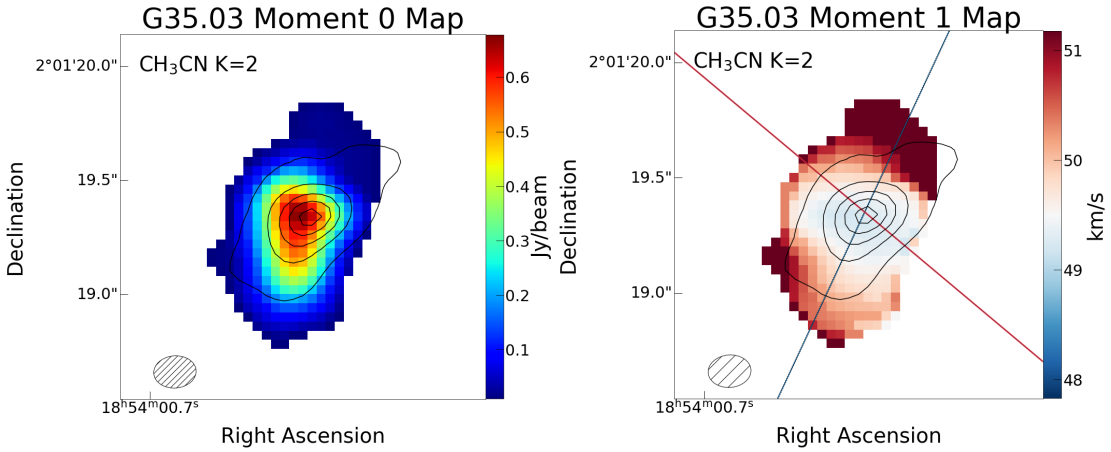

Figure A.39: *Left:* Moment 0 map for G35.03. *Right:* Moment 1 map of G35.03, including pv cut position angle of 50° (black line), and approximate direction of molecular outflow, as determined by Beltrán *et al.*, 2014 (red line). Contours in both plots represent 10, 30, 50, 70 & 90 % peak flux.

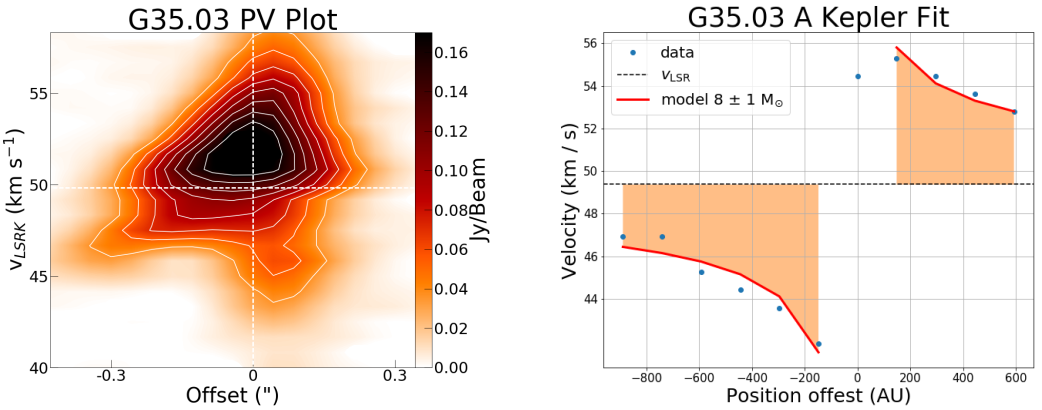

Figure A.40: *Left:* PV diagram of G35.03. Contours represent 20, 30,... 90 % peak flux. White dashed lines indicate V_{LSR} (horizontal) and central offset position (vertical). *Right:* Seifried Kepler fit of G35.03.

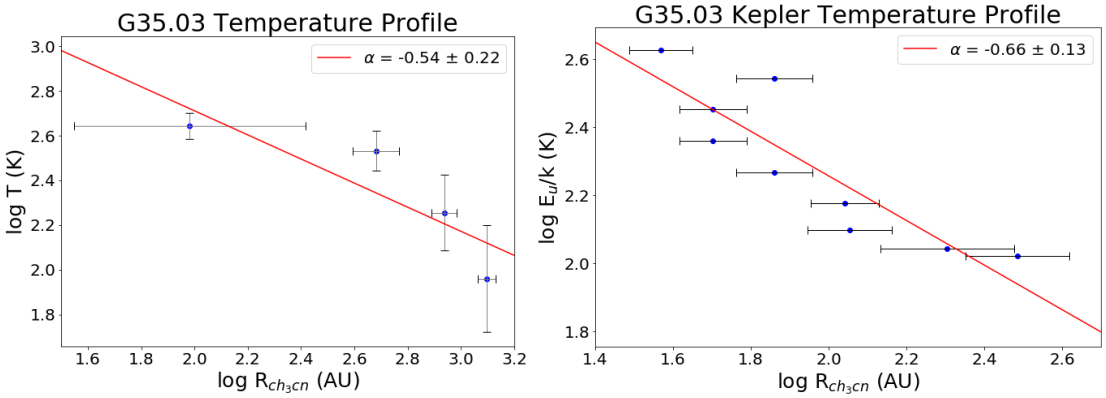

Figure A.41: *Left:* Temperature vs Radius profile of G35.03. *Right:* Temperature profile of G35.03 assuming Kepler rotation.

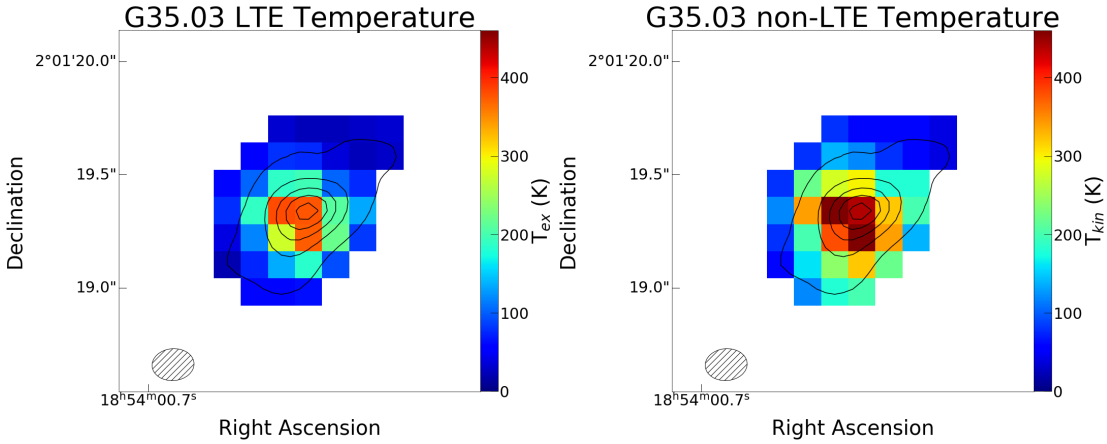

Figure A.42: *Left:* G35.03 LTE temperature map produced by population diagrams. *Right:* Non-LTE temperature map produced by RADEX grids. Contours on both plots represent 10, 30, 50, 70 & 90 % peak flux.

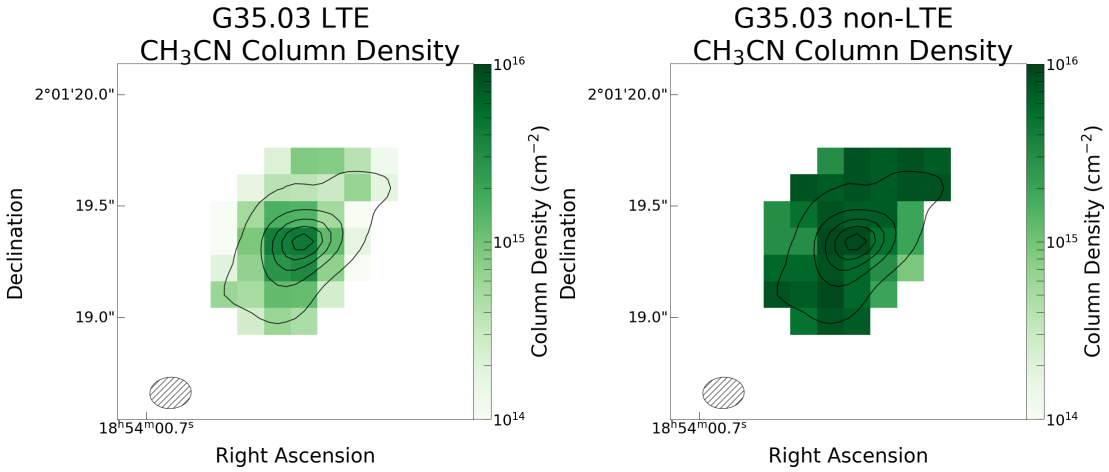

Figure A.43: *Left:* G35.03 LTE CH_3CN column density map produced by population diagrams. *Right:* Non-LTE CH_3CN column density map produced by RADEX grids. Contours on both plots represent 10, 30, 50, 70 & 90 % peak flux.

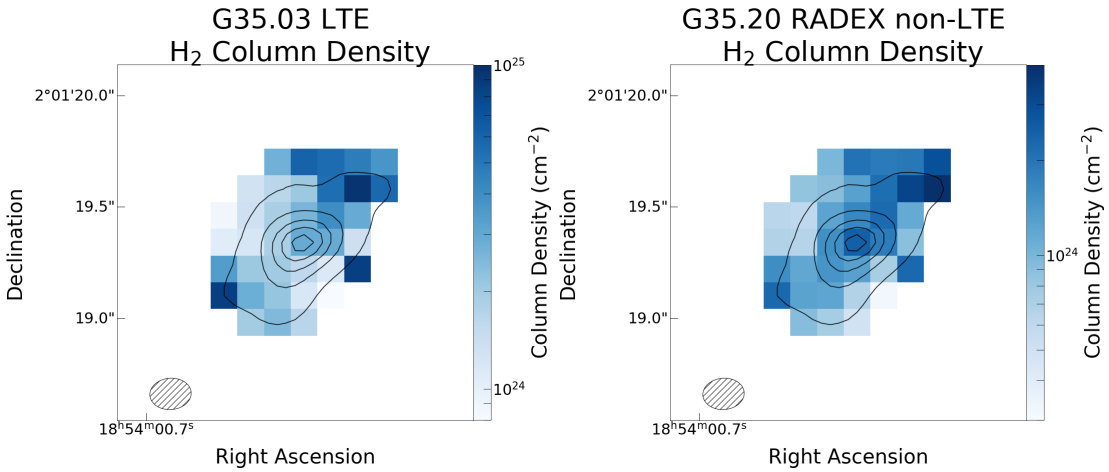

Figure A.44: *Left:* G35.03 LTE H_2 column density map produced from continuum emission, using LTE temperatures. *Right:* Non-LTE H_2 column density map except using temperatures from non-LTE analysis. Contours on both plots represent 10, 30, 50, 70 & 90 % peak flux.

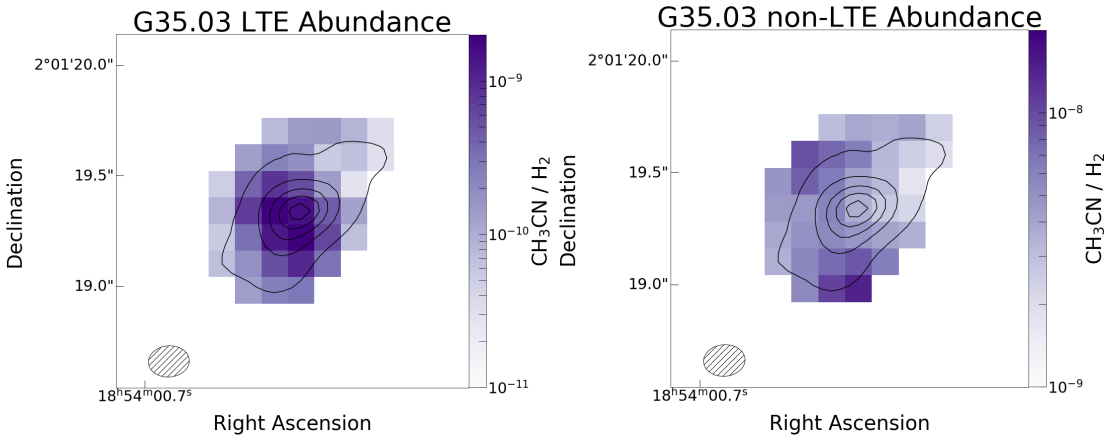

Figure A.45: *Left:* G35.03 LTE abundance map produced from ratio of LTE CH_3CN column density to LTE H_2 column density. *Right:* Ratio of CH_3CN column density to H_2 column density using non-LTE results. Contours on both plots represent 10, 30, 50, 70 & 90 % peak flux.

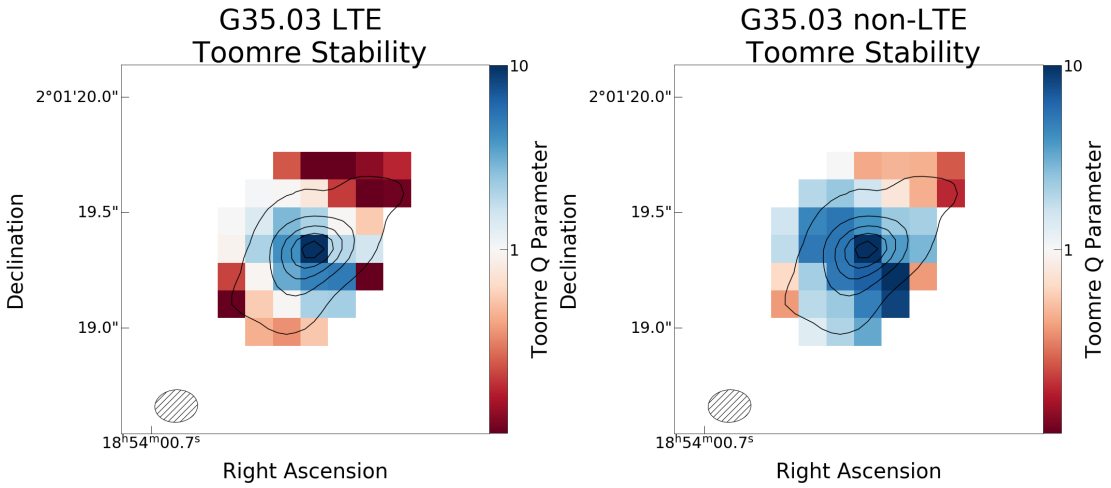

Figure A.46: *Left:* Toomre stability plot of G35.03 using LTE temperatures and H_2 column densities. *Right:* Same as left but with non-LTE parameters.

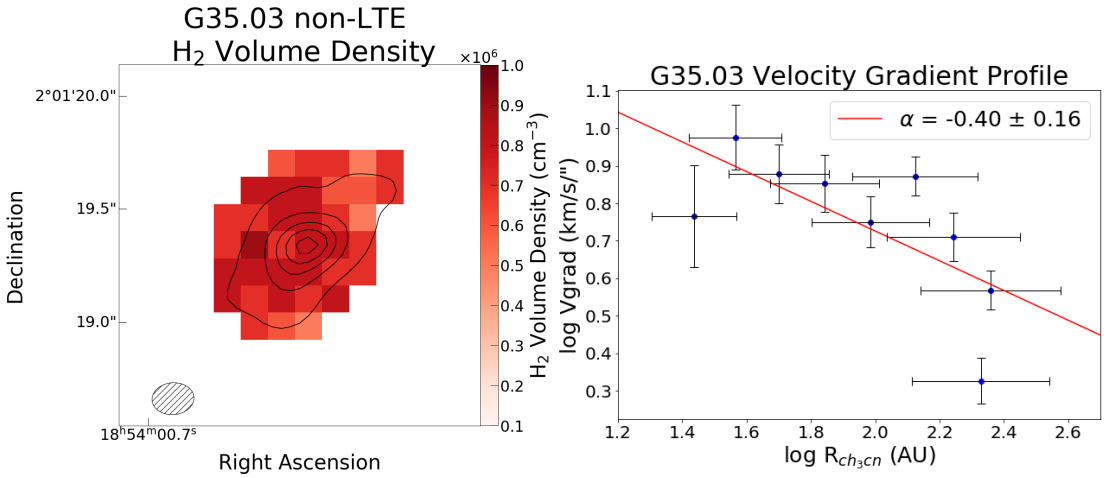

Figure A.47: *Left:* G35.03 H_2 volume density map produced by RADEX non-LTE analysis. *Right:* G35.03 velocity gradient profile.

A.7 G35.20 Plots

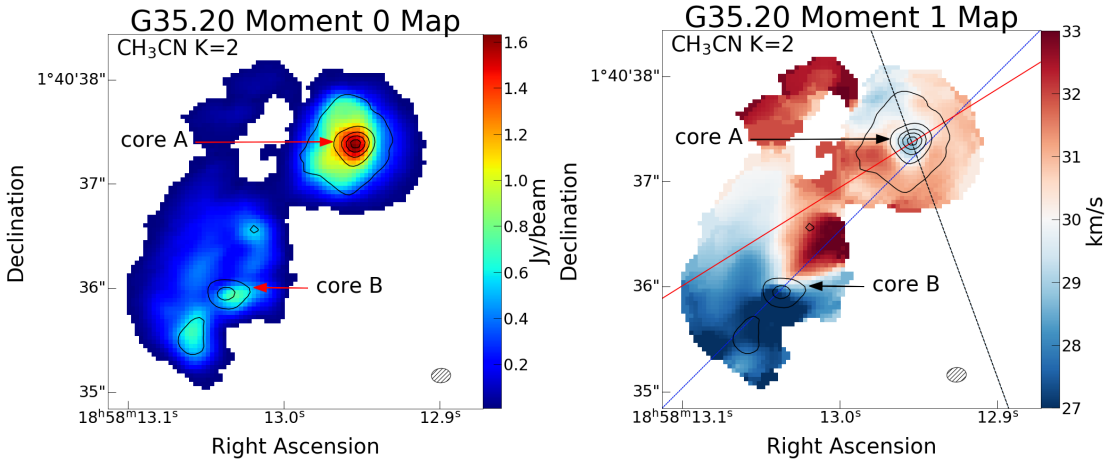

Figure A.48: *Left:* Moment 0 map for G35.20. *Right:* Moment 1 map of G35.20, including pv cut position angles of 20° for core A (black line), and -45° for core B (blue line). Approximate direction of the molecular outflow is shown as the red line, as determined by Gibb *et al.*, 2003. Contours in both plots represent 10, 30, 50, 70 & 90 % peak flux.

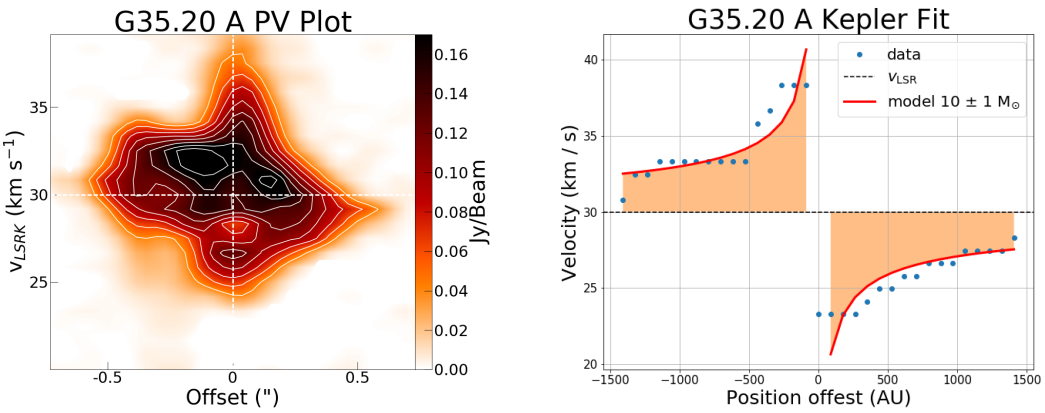

Figure A.49: *Left:* PV diagram of G35.20. Contours represent 20, 30,... 90 % peak flux. White dashed lines indicate V_{LSR} (horizontal) and central offset position (vertical). *Right:* Seifried Kepler fit of G35.20.

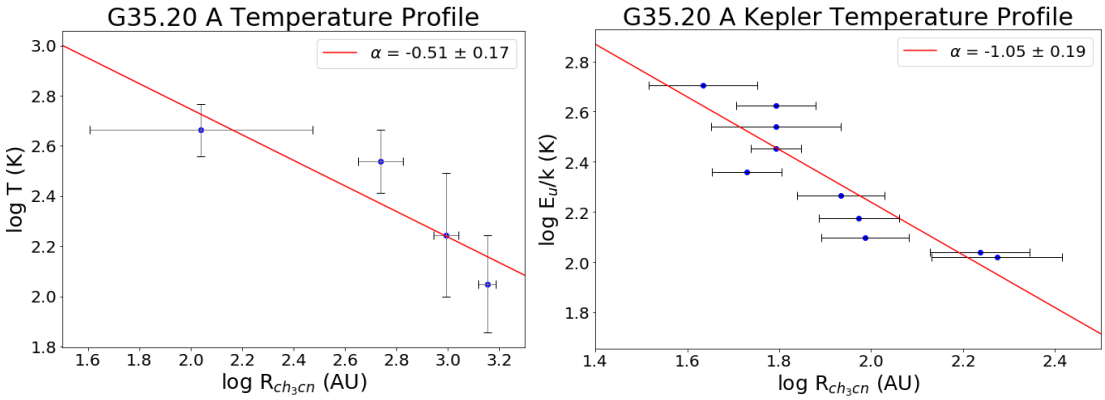

Figure A.50: *Left:* Temperature vs Radius profile of G35.20. *Right:* Temperature profile of G35.20 assuming Kepler rotation.

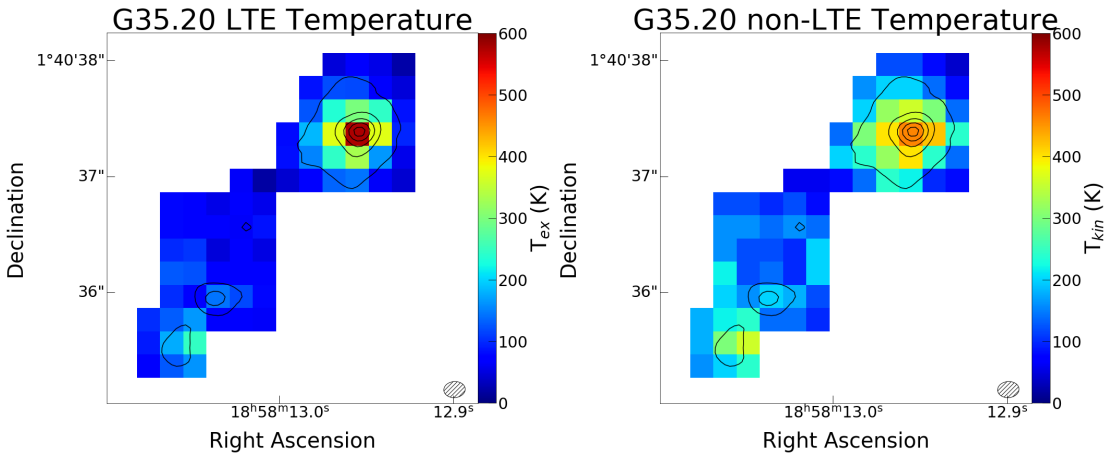

Figure A.51: *Left:* G35.20 LTE temperature map produced by population diagrams. *Right:* Non-LTE temperature map produced by RADEX grids. Contours on both plots represent 10, 30, 50, 70 & 90 % peak flux.

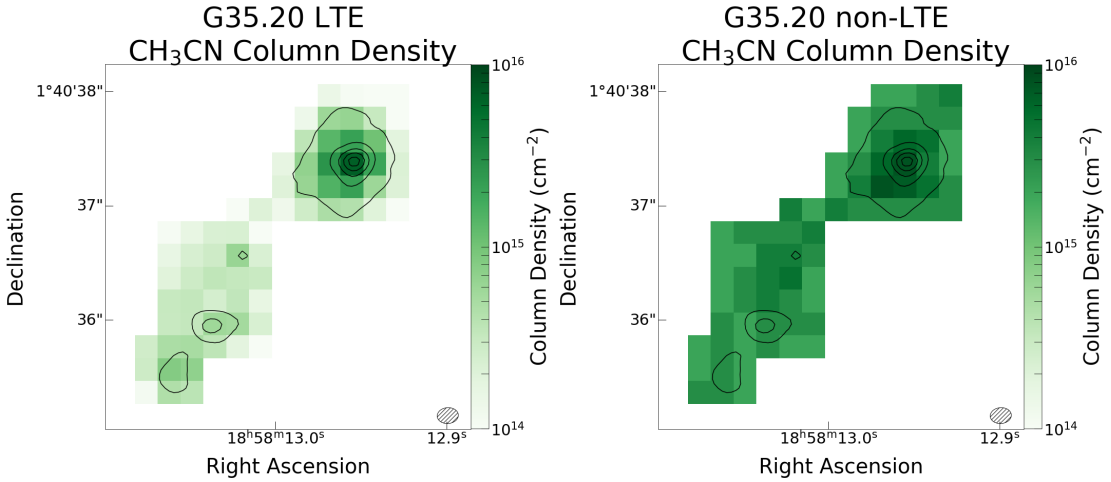

Figure A.52: *Left:* G35.20 LTE CH_3CN column density map produced by population diagrams. *Right:* Non-LTE CH_3CN column density map produced by RADEX grids. Contours on both plots represent 10, 30, 50, 70 & 90 % peak flux.

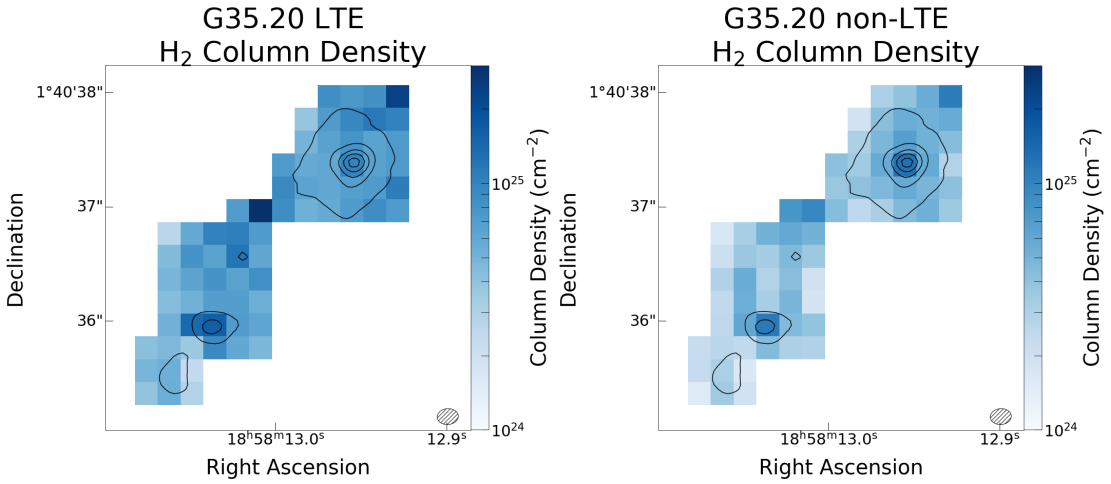

Figure A.53: *Left:* G35.20 LTE H_2 column density map produced from continuum emission, using LTE temperatures. *Right:* Non-LTE H_2 column density map except using temperatures from non-LTE analysis. Contours on both plots represent 10, 30, 50, 70 & 90 % peak flux.

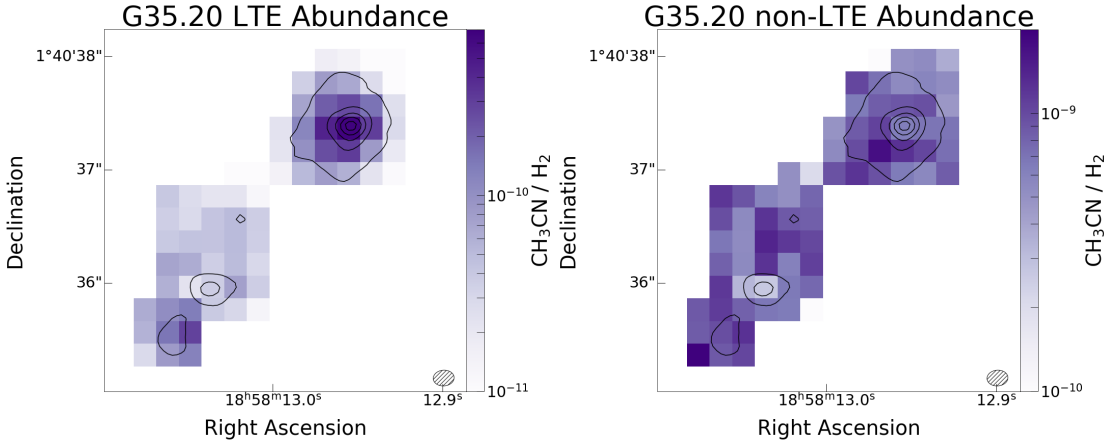

Figure A.54: *Left:* G35.20 LTE abundance map produced from ratio of LTE CH_3CN column density to LTE H_2 column density. *Right:* Ratio of CH_3CN column density to H_2 column density using non-LTE results. Contours on both plots represent 10, 30, 50, 70 & 90 % peak flux.

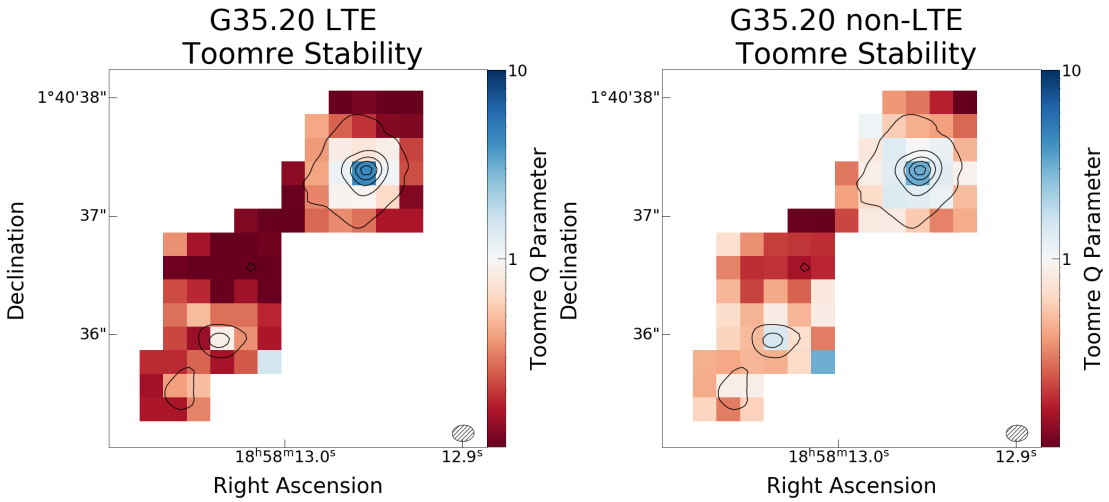

Figure A.55: *Left:* Toomre stability plot of G35.20 using LTE temperatures and H_2 column densities. *Right:* Same as left but with non-LTE parameters.

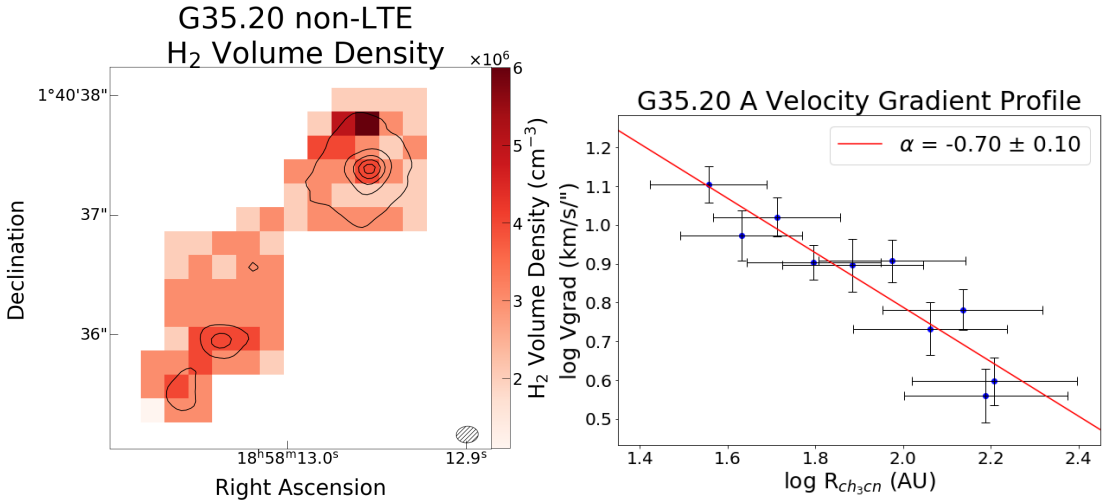

Figure A.56: *Left:* G35.20 H_2 volume density map produced by RADEX non-LTE analysis. *Right:* G35.20 velocity gradient profile.

A.8 G37.55 Plots

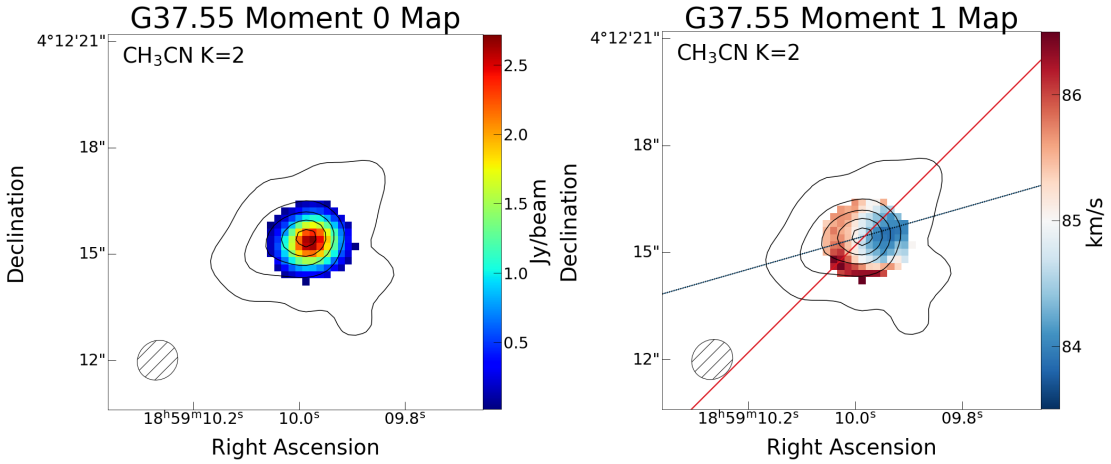

Figure A.57: *Left:* Moment 0 map for G37.55. *Right:* Moment 1 map of G37.55, including pv cut position angle of 106° (black line), and approximate direction of molecular outflow, as determined by Zhang *et al.*, 2007 (red line). Contours in both plots represent 10, 30, 50, 70 & 90 % peak flux.

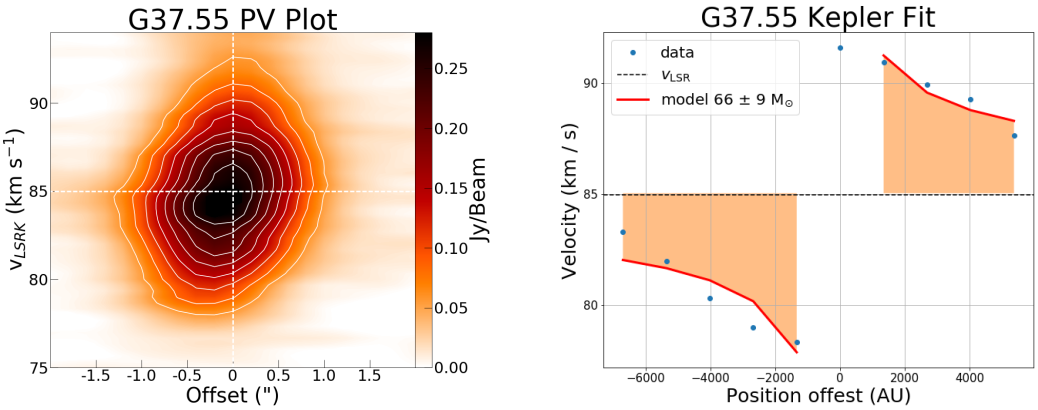

Figure A.58: *Left:* PV diagram of G37.55. Contours represent 20, 30,... 90 % peak flux. White dashed lines indicate V_{LSR} (horizontal) and central offset position (vertical). *Right:* Seifried Kepler fit of G37.55.

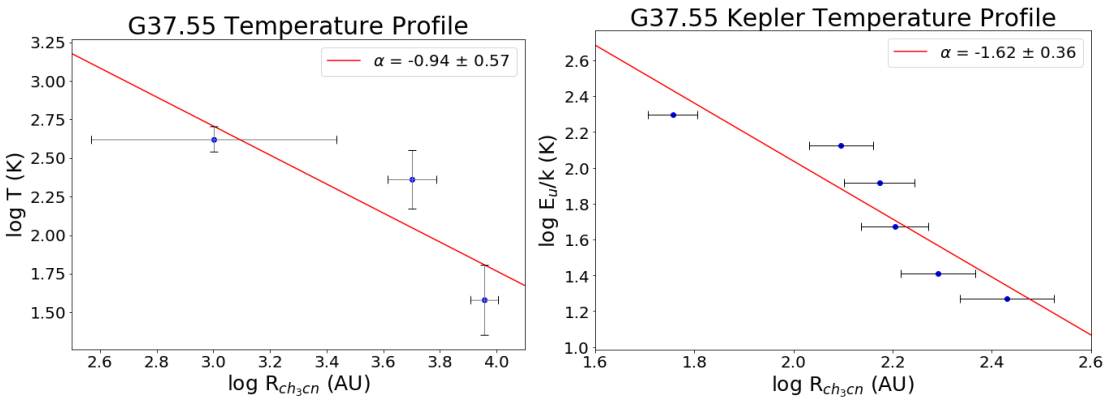

Figure A.59: *Left:* Temperature vs Radius profile of G37.55. *Right:* Temperature profile of G37.55 assuming Kepler rotation.

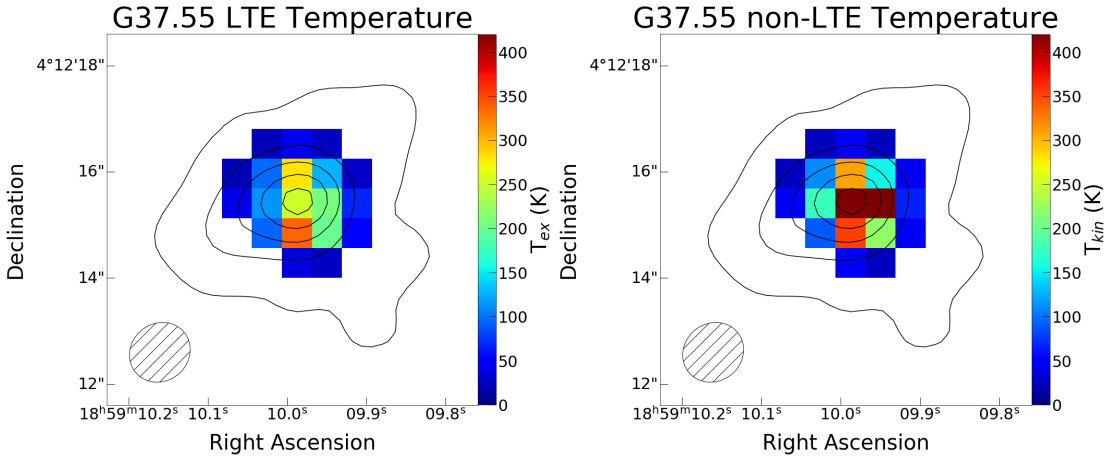

Figure A.60: *Left:* G37.55 LTE temperature map produced by population diagrams. *Right:* Non-LTE temperature map produced by RADEX grids. Contours on both plots represent 10, 30, 50, 70 & 90 % peak flux.

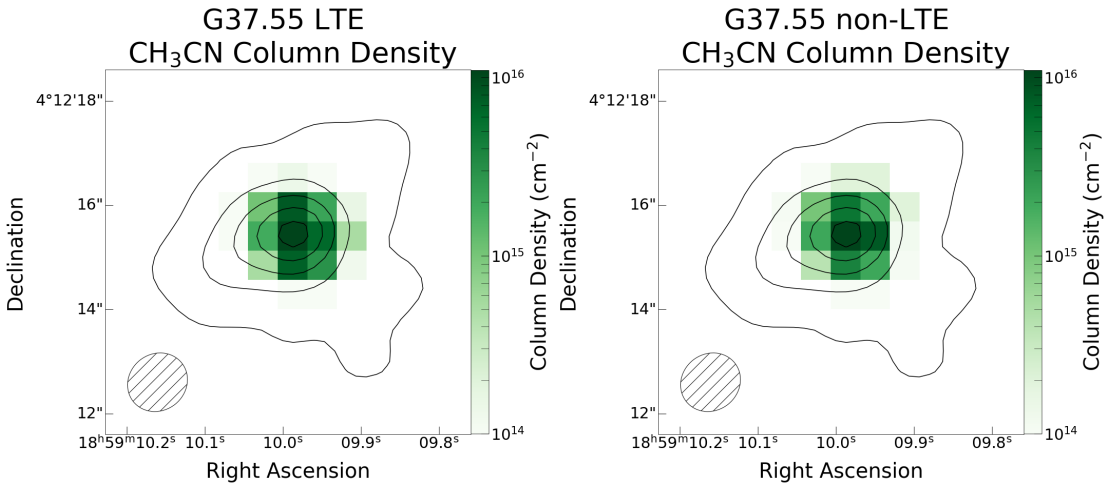

Figure A.61: *Left:* G37.55 LTE CH_3CN column density map produced by population diagrams. *Right:* Non-LTE CH_3CN column density map produced by RADEX grids. Contours on both plots represent 10, 30, 50, 70 & 90 % peak flux.

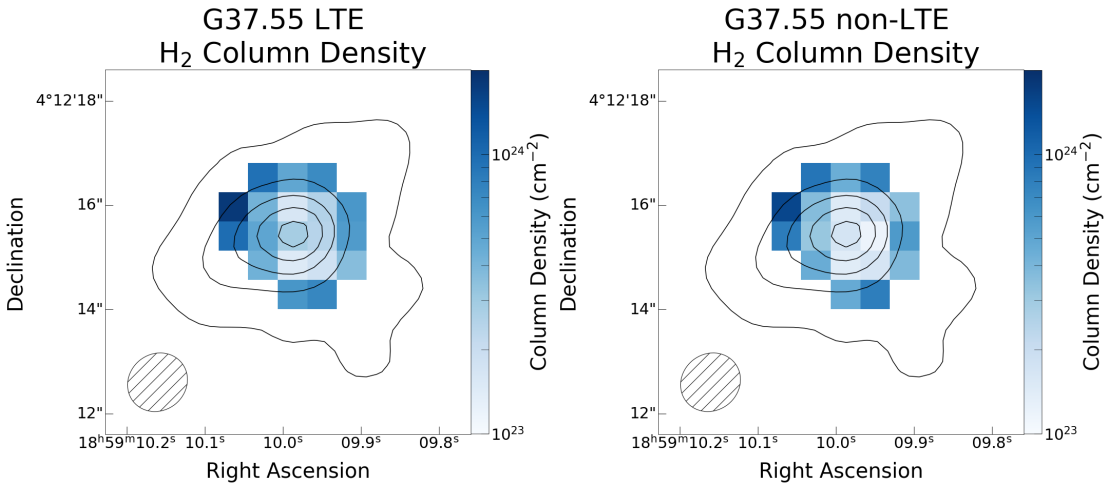

Figure A.62: *Left:* G37.55 LTE H_2 column density map produced from continuum emission, using LTE temperatures. *Right:* Non-LTE H_2 column density map except using temperatures from non-LTE analysis. Contours on both plots represent 10, 30, 50, 70 & 90 % peak flux.

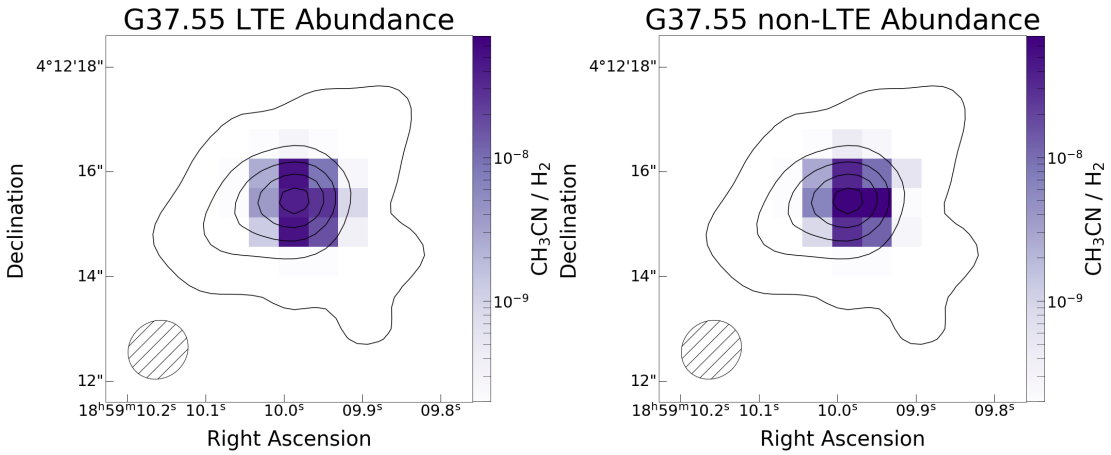

Figure A.63: *Left:* G37.55 LTE abundance map produced from ratio of LTE CH_3CN column density to LTE H_2 column density. *Right:* Ratio of CH_3CN column density to H_2 column density using non-LTE results. Contours on both plots represent 10, 30, 50, 70 & 90 % peak flux.

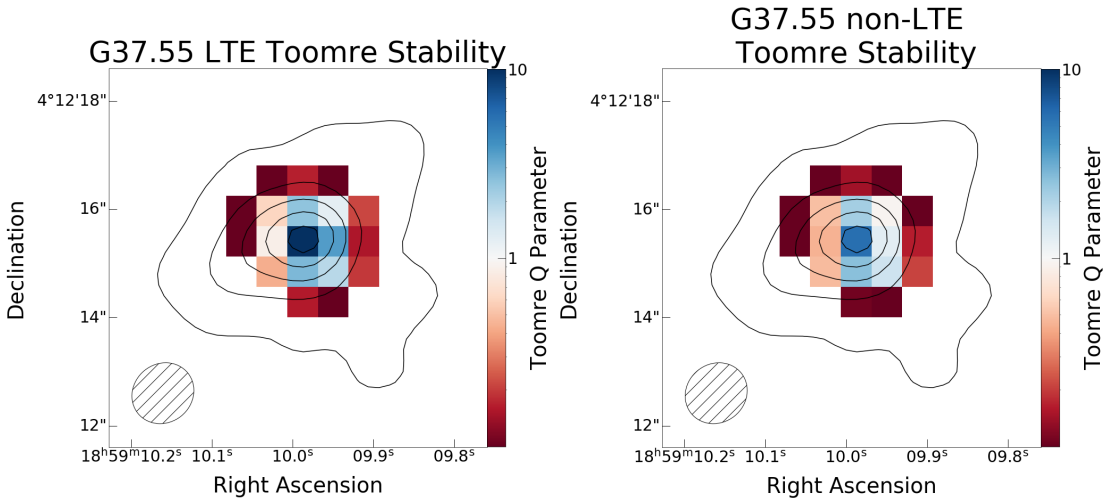

Figure A.64: *Left:* Toomre stability plot of G37.55 using LTE temperatures and H_2 column densities. *Right:* Same as left but with non-LTE parameters.

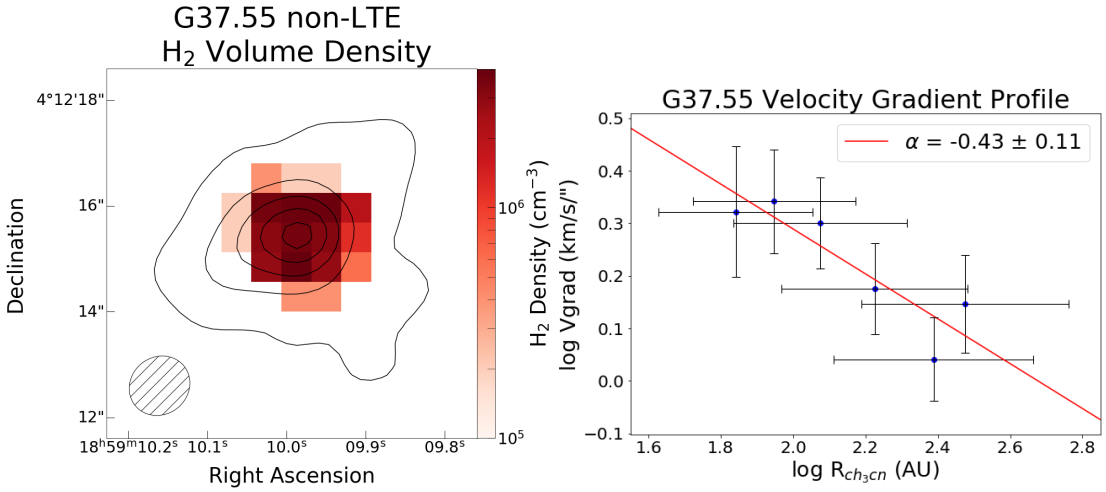

Figure A.65: *Left:* G37.55 H_2 volume density map produced by RADEX non-LTE analysis. *Right:* G37.55 velocity gradient profile.

A.9 CH_3CN Spectral Windows

AFGL 4176

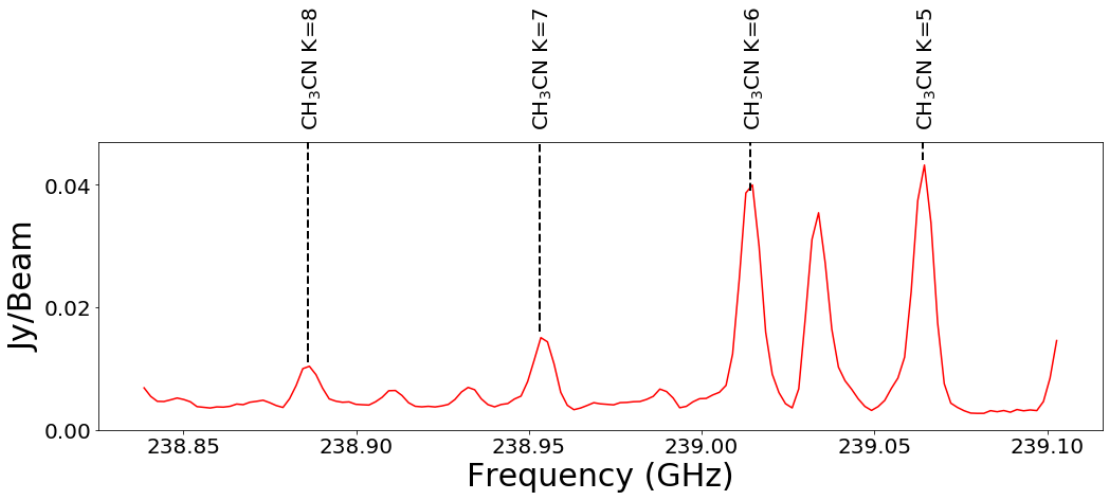

Figure A.66: Spectral window containing AFGL 4176 CH_3CN J=13-12 lines.

G23.01

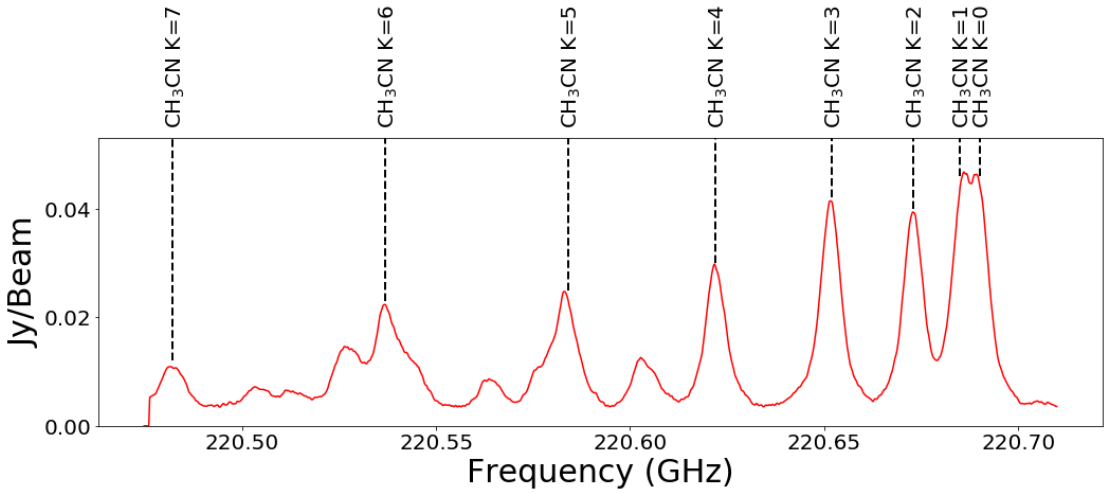

Figure A.67: Spectral window containing G23.01 CH_3CN J=12-11 lines.

G24.78

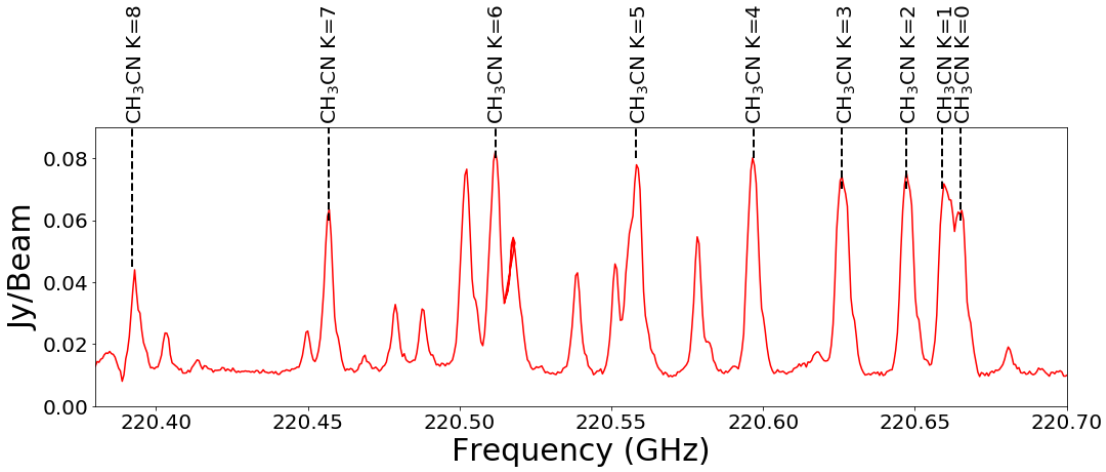

Figure A.68: Spectral window containing G24.78 CH_3CN J=12-11 lines.

G29.96

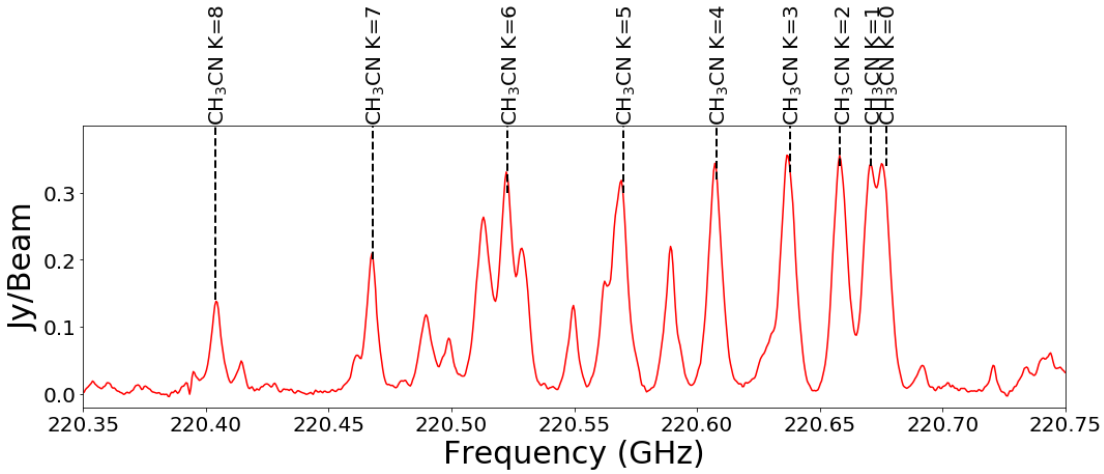

Figure A.69: Spectral window containing G29.96 CH_3CN J=12-11 lines.

G34.43

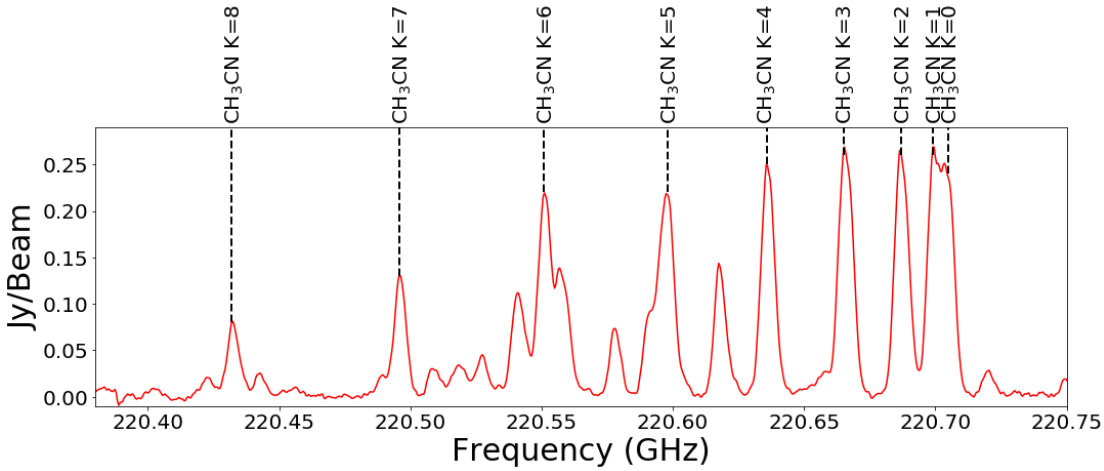

Figure A.70: Spectral window containing G34.43 CH_3CN J=12-11 lines.

G35.03

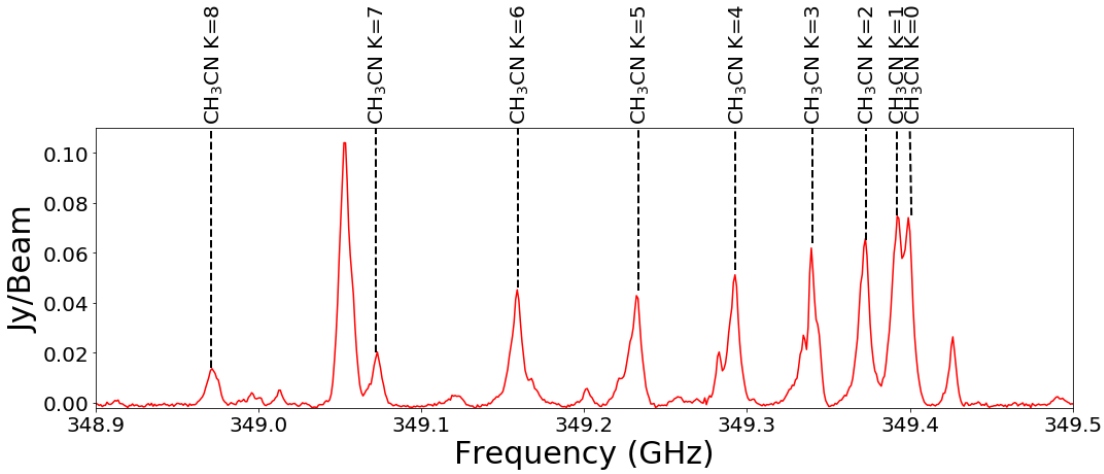

Figure A.71: Spectral window containing G35.03 CH_3CN J=19-18 lines.

G35.20

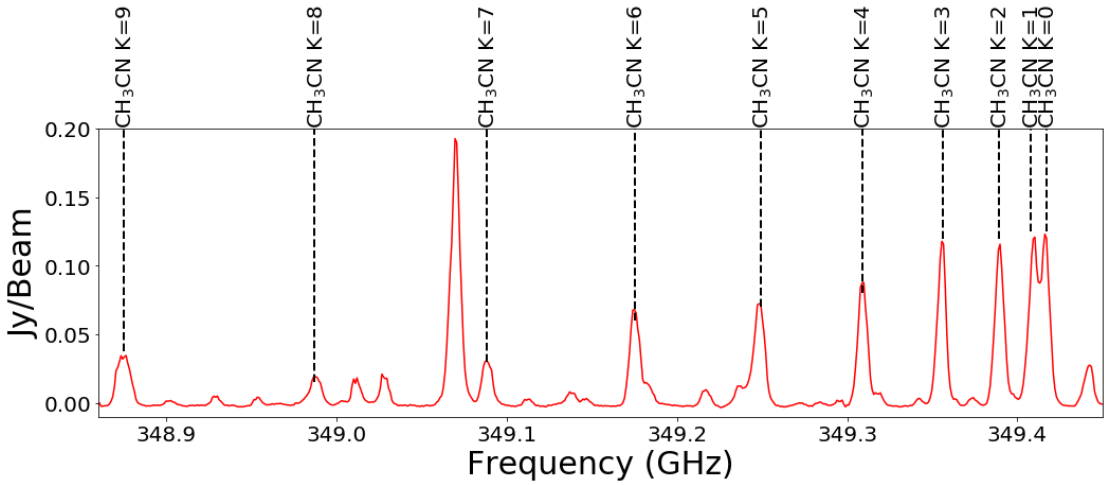

Figure A.72: Spectral window containing G35.20 CH_3CN J=19-18 lines.

G37.55

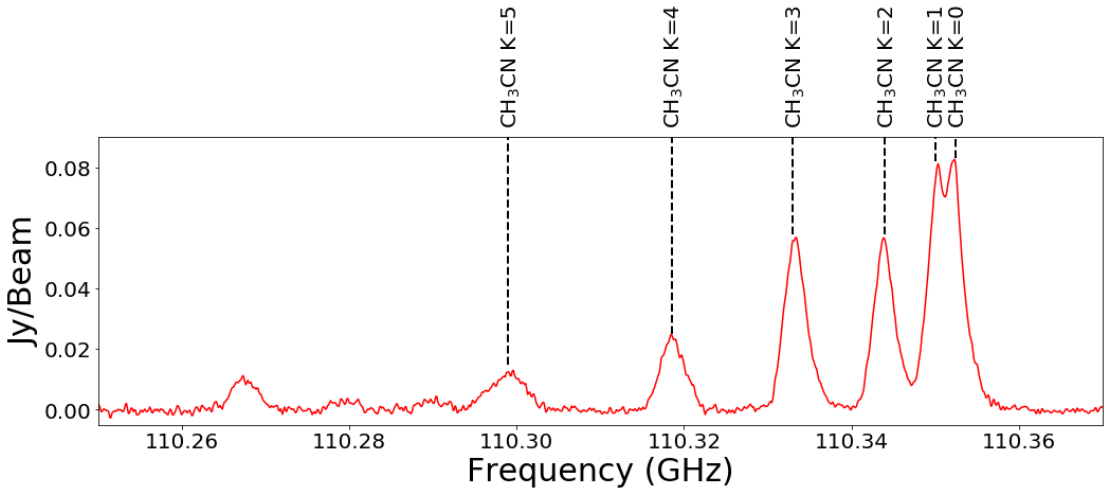

Figure A.73: Spectral window containing G37.55 CH_3CN J=6-5 lines.

Bibliography

1. Adam, R *et al.* Planck intermediate results-XXXII. The relative orientation between the magnetic field and structures traced by interstellar dust. *Astronomy & Astrophysics* **586,** A135 (2016).
2. Ade, P. *et al.* Planck intermediate results-XXXV. Probing the role of the magnetic field in the formation of structure in molecular clouds. *Astronomy & Astrophysics* **586,** A138 (2016).
3. Ahmadi, A. *et al.* Core fragmentation and Toomre stability analysis of W3(H_2O). A case study of the IRAM NOEMA large program CORE. *A&A* **618,** A46. arXiv: 1808.00472 [astro-ph.GA] (Oct. 2018).
4. Allen, V., van der Tak, F. F. S., Sánchez-Monge, Á., Cesaroni, R. & Beltrán, M. T. Chemical segregation in hot cores with disk candidates. An investigation with ALMA. *A&A* **603,** A133. arXiv: 1705.06346 [astro-ph.SR] (July 2017).
5. André, P. Interstellar filaments and star formation. *Comptes Rendus Geoscience* **349,** 187 –197. ISSN: 1631-0713. http://www.sciencedirect.com/science/article/pii/S1631071317300901 (2017).
6. Aso, Y. *et al.* ALMA Observations of the Protostar L1527 IRS: Probing Details of the Disk and the Envelope Structures. *ApJ* **849,** 56. arXiv: 1707.08697 [astro-ph.SR] (Nov. 2017).
7. Bell, T. A. *et al.* Extended warm gas in Orion KL as probed by methyl cyanide. *A&A* **564,** A114. arXiv: 1402.2842 [astro-ph.GA] (Apr. 2014).
8. Beltrán, M. T., Cesaroni, R., Moscadelli, L. & Codella, C. The hyperyoung H ii region in G24.78+0.08 A1. *A&A* **471,** L13–L16. arXiv: 0706.2567 [astro-ph] (Aug. 2007).
9. Beltrán, M. T., Cesaroni, R., Neri, R. & Codella, C. Rotating toroids in G10.62-0.38, G19.61-0.23, and G29.96-0.02. *A&A* **525,** A151. arXiv: 1010.0843 [astro-ph.GA] (Jan. 2011).
10. Beltrán, M. T. & de Wit, W. J. Accretion disks in luminous young stellar objects. *A&ARv* **24,** 6. arXiv: 1509.08335 [astro-ph.GA] (Jan. 2016).
11. Beltrán, M. T. *et al.* A detailed study of the rotating toroids in G31.41+0.31 and G24.78+0.08. *A&A* **435,** 901–925. arXiv: astro-ph/0502071 [astro-ph] (June 2005).
12. Beltrán, M. T. *et al.* Filamentary structure and Keplerian rotation in the high-mass star-forming region G35.03+0.35 imaged with ALMA. *A&A* **571,** A52 (Nov. 2014).

13. Beltrán, M. T. *et al.* Molecular outflows and hot molecular cores in G24.78+0.08 at sub-arcsecond angular resolution. *A&A* **532,** A91. arXiv: 1107.0314 [astro-ph.GA] (Aug. 2011).
14. Beltrán, M. T. *et al.* Molecular outflows and hot molecular cores in G24.78+0.08 at sub-arcsecond angular resolution. *A&A* **532,** A91. arXiv: 1107.0314 [astro-ph.GA] (Aug. 2011).
15. Bernasconi, P. A. & Maeder, A. About the absence of a proper zero age main sequence for massive stars. *A&A* **307,** 829–839 (Mar. 1996).
16. Beuther, H. *et al. Massive Molecular Outflows* in *Hot Star Workshop III: The Earliest Phases of Massive Star Birth* (ed Crowther, P.) **267** (Oct. 2002), 341. arXiv: astro-ph/0112508 [astro-ph].
17. Bøgelund, E. G. *et al.* Molecular complexity on disc scales uncovered by ALMA. Chemical composition of the high-mass protostar AFGL 4176. *A&A* **628,** A2. arXiv: 1906.06156 [astro-ph.SR] (Aug. 2019).
18. Boley, P. A. *et al.* On the massive young stellar object AFGL 4176. High-spatial-resolution multi-wavelength observations and modeling. *A&A* **547,** A88. arXiv: 1209.3583 [astro-ph.SR] (Nov. 2012).
19. Bonnell, I. A., Bate, M. R., Clarke, C. J. & Pringle, J. E. Competitive accretion in embedded stellar clusters. *MNRAS* **323,** 785–794. arXiv: astro-ph/0102074 [astro-ph] (May 2001).
20. Bonnell, I. *Competitive Accretion* in *Star Formation, Then and Now* (Aug. 2007), 25.
21. Bosco, F. *et al.* Fragmentation, rotation, and outflows in the high-mass star-forming region IRAS 23033+5951. A case study of the IRAM NOEMA large program CORE. *A&A* **629,** A10. arXiv: 1907.04225 [astro-ph.SR] (Sept. 2019).
22. Cesaroni, R., Galli, D., Lodato, G., Walmsley, C. M. & Zhang, Q. *Disks around Young O-B (Proto)Stars: Observations and Theory* 2006. arXiv: astro-ph/0603093 [astro-ph].
23. Cesaroni, R., Galli, D., Lodato, G., Walmsley, C. M. & Zhang, Q. *Disks Around Young O-B (Proto)Stars: Observations and Theory* in *Protostars and Planets V* (eds Reipurth, B., Jewitt, D. & Keil, K.) (Jan. 2007), 197. arXiv: astro-ph/0603093 [astro-ph].
24. Cesaroni, R. *et al.* Chasing discs around O-type (proto)stars: Evidence from ALMA observations. *A&A* **602,** A59 (June 2017).
25. Codella, C. *et al.* SiO collimated outflows driven by high-mass YSOs in G24.78+0.08. *A&A* **550,** A81. arXiv: 1212.0473 [astro-ph.SR] (Feb. 2013).
26. Garrod, R. T., Belloche, A., Müller, H. S. P. & Menten, K. M. Exploring molecular complexity with ALMA (EMoCA): Simulations of branched carbon-chain chemistry in Sgr B2(N). *A&A* **601,** A48. arXiv: 1701.07160 [astro-ph.GA] (May 2017).
27. Garrod, R. T. A Three-phase Chemical Model of Hot Cores: The Formation of Glycine. *ApJ* **765,** 60. arXiv: 1302.0688 [astro-ph.GA] (Mar. 2013).
28. Garrod, R. T., Widicus Weaver, S. L. & Herbst, E. Complex Chemistry in Star-forming Regions: An Expanded Gas-Grain Warm-up Chemical Model. *ApJ* **682,** 283–302. arXiv: 0803.1214 [astro-ph] (July 2008).

29. Gibb, A. G., Hoare, M. G., Little, L. T. & Wright, M. C. H. A detailed study of G35.2-0.7N: collimated outflows in a cluster of high-mass young stellar objects. *MNRAS* **339,** 1011–1024. arXiv: astro-ph/0211059 [astro-ph] (Mar. 2003).
30. Gibb, E., Nummelin, A., Irvine, W. M., Whittet, D. C. B. & Bergman, P. Chemistry of the Organic-Rich Hot Core G327.3-0.6. *ApJ* **545,** 309–326 (Dec. 2000).
31. Ginsburg, A., Bally, J., Goddi, C., Plambeck, R. & Wright, M. A Keplerian Disk around Orion SrCI, a 15 $M_\odot$ YSO. *ApJ* **860,** 119. arXiv: 1804.10622 [astro-ph.GA] (June 2018).
32. Goldsmith, P. F. & Langer, W. D. Population Diagram Analysis of Molecular Line Emission. *ApJ* **517,** 209–225 (May 1999).
33. Green, S. Collisional Excitation of Interstellar Methyl Cyanide. *ApJ* **309,** 331 (Oct. 1986).
34. Greene, T. Protostars. *American Scientist* **89,** 316 (Aug. 2001).
35. Hirota, T. Recent Progress in High-Mass Star-Formation Studies with ALMA. *Publication of Korean Astronomical Society* **33,** 21–30. arXiv: 1806.10837 [astro-ph.GA] (Sept. 2018).
36. Hofner, P. *et al.* High-resolution Observations of the Massive Protostar in IRAS 18566+0408. *ApJ* **843,** 99. arXiv: 1705.07203 [astro-ph.GA] (July 2017).
37. Johnston, K. G. *et al.* A Detailed View of the Circumstellar Environment and Disk of the Forming O-star AFGL 4176. *arXiv e-prints,* arXiv:2004.13739. arXiv: 2004.13739 [astro-ph.SR] (Apr. 2020).
38. Johnston, K. G. *et al.* A Keplerian-like Disk around the Forming O-type Star AFGL 4176. *ApJ* **813,** L19. arXiv: 1509.08469 [astro-ph.SR] (Nov. 2015).
39. Kenyon, S. J. & Hartmann, L. Spectral Energy Distributions of T Tauri Stars: Disk Flaring and Limits on Accretion. *ApJ* **323,** 714 (Dec. 1987).
40. Klassen, M., Pudritz, R. E., Kuiper, R., Peters, T. & Banerjee, R. Simulating the Formation of Massive Protostars. I. Radiative Feedback and Accretion Disks. *ApJ* **823,** 28. arXiv: 1603.07345 [astro-ph.GA] (May 2016).
41. Koumpia, E. *et al.* Temperatures of dust and gas in S 140. *A&A* **580,** A68. arXiv: 1504.05000 [astro-ph.SR] (Aug. 2015).
42. Kratter, K. M., Matzner, C. D., Krumholz, M. R. & Klein, R. I. On the Role of Disks in the Formation of Stellar Systems: A Numerical Parameter Study of Rapid Accretion. *ApJ* **708,** 1585–1597. arXiv: 0907.3476 [astro-ph.SR] (Jan. 2010).
43. Li, S. *et al.* Formation of Massive Protostellar Clusters—Observations of Massive 70 μm Dark Molecular Clouds. *ApJ* **886,** 130. arXiv: 1909.08916 [astro-ph.GA] (Dec. 2019).
44. Linke, R. A., Frerking, M. A. & Thaddeus, P. Interstellar methyl mercaptan. *ApJ* **234,** L139–L142 (Dec. 1979).
45. Lumsden, S. L. *et al.* The Red MSX Source Survey: The Massive Young Stellar Population of Our Galaxy. *ApJ* **208,** 11. arXiv: 1308.0134 [astro-ph.GA] (Sept. 2013).

46. Martín, S. *et al.* Spectral Line Identification and Modelling (SLIM) in the MAdrid Data CUBe Analysis (MADCUBA) package. Interactive software for data cube analysis. *A&A* **631,** A159. arXiv: 1909.02147 [astro-ph.IM] (Nov. 2019).
47. Maud, L. T. *et al.* Chasing discs around O-type (proto)stars. ALMA evidence for an SiO disc and disc wind from G17.64+0.16. **620,** A31. arXiv: 1810.03920 [astro-ph.SR] (Nov. 2018).
48. McKee, C. F. & Ostriker, E. C. Theory of Star Formation. *ARA&A* **45,** 565–687. arXiv: 0707.3514 [astro-ph] (Sept. 2007).
49. McKee, C. F. & Tan, J. C. The Formation of Massive Stars from Turbulent Cores. *ApJ* **585,** 850–871. arXiv: astro-ph/0206037 [astro-ph] (Mar. 2003).
50. McMullin, J. P., Waters, B., Schiebel, D., Young, W. & Golap, K. *CASA Architecture and Applications* in *Astronomical Data Analysis Software and Systems XVI* (eds Shaw, R. A., Hill, F. & Bell, D. J.) **376** (Oct. 2007), 127.
51. Möller, T., Endres, C. & Schilke, P. eXtended CASA Line Analysis Software Suite (XCLASS). *A&A* **598,** A7. arXiv: 1508.04114 [astro-ph.IM] (Feb. 2017).
52. Moscadelli, L. *et al.* A 10-$M_\odot$ YSO with a Keplerian disk and a nonthermal radio jet. *A&A* **622,** A206. arXiv: 1901.02713 [astro-ph.SR] (Feb. 2019).
53. Moscadelli, L. *et al.* The feedback of an HC HII region on its parental molecular core. The case of core A1 in the star-forming region G24.78+0.08. *A&A* **616,** A66 (Aug. 2018).
54. Motte, F., Bontemps, S. & Louvet, F. High-Mass Star and Massive Cluster Formation in the Milky Way. *ARA&A* **56,** 41–82. arXiv: 1706.00118 [astro-ph.GA] (Sept. 2018).
55. Mundy, L. G., Looney, L. W. & Welch, W. J. *The Structure and Evolution of Envelopes and Disks in Young Stellar Systems* in *Protostars and Planets IV* (eds Mannings, V., Boss, A. P. & Russell, S. S.) (May 2000), 355.
56. Oberg, K. I. *et al. Interstellar Ice Chemistry: From Water to Complex Organics* in *American Astronomical Society Meeting Abstracts* **222** (June 2013), 202.02.
57. Öberg, K. I. *et al.* The Spitzer Ice Legacy: Ice Evolution from Cores to Protostars. *ApJ* **740,** 109. arXiv: 1107.5825 [astro-ph.GA] (Oct. 2011).
58. Ossenkopf, V. & Henning, T. Dust opacities for protostellar cores. *A&A* **291,** 943–959 (Nov. 1994).
59. Palmeirim, P. *et al.* Herschel view of the Taurus B211/3 filament and striations: evidence of filamentary growth? *A&A* **550,** A38. https://doi.org/10.1051/0004-6361/201220500 (2013).
60. Perault, M. *et al.* First ISOCAM images of the Milky Way. *A&A* **315,** L165–L168 (Nov. 1996).
61. Pringle, J. E. Accretion discs in astrophysics. *ARA&A* **19,** 137–162 (Jan. 1981).
62. Rathborne, J. M., Jackson, J. M., Zhang, Q. & Simon, R. Submillimeter Array Observations of Infrared Dark Clouds: A Tale of Two Cores. *ApJ* **689,** 1141–1149. arXiv: 0808.2973 [astro-ph] (Dec. 2008).

63. Salpeter, E. E. The Luminosity Function and Stellar Evolution. *ApJ* **121,** 161 (Jan. 1955).
64. Sánchez-Monge, Á. *et al.* A candidate circumbinary Keplerian disk in G35.20-0.74 N: A study with ALMA. *A&A* **552,** L10. arXiv: 1303.4242 [astro-ph.GA] (Apr. 2013).
65. Sanchez-Monge, A. *Caught in the act: disruption of a high-mass disk by anisotropic accretion* in *ALMA2019: Science Results and Cross-Facility Synergies* (Dec. 2019), 122.
66. Sanhueza, P. *et al.* Molecular Outflows Within the Filamentary Infrared Dark Cloud G34.43+0.24. *ApJ* **715,** 18–32. arXiv: 1005.3048 [astro-ph.GA] (May 2010).
67. Sanna, A. *et al.* Discovery of a sub-Keplerian disk with jet around a 20 $M_\odot$ young star. ALMA observations of G023.01-00.41. *A&A* **623,** A77. arXiv: 1805.09842 [astro-ph.SR] (Mar. 2019).
68. Sanna, A. *et al.* Momentum-driven outflow emission from an O-type YSO. Comparing the radio jet with the molecular outflow. *A&A* **596,** L2. arXiv: 1611.00408 [astro-ph.GA] (Nov. 2016).
69. Schöier, F. L., van der Tak, F. F. S., van Dishoeck, E. F. & Black, J. H. An atomic and molecular database for analysis of submillimetre line observations. *A&A* **432,** 369–379. arXiv: astro-ph/0411110 [astro-ph] (Mar. 2005).
70. Seifried, D., Sánchez-Monge, Á., Walch, S. & Banerjee, R. Revealing the dynamics of Class 0 protostellar discs with ALMA. *MNRAS* **459,** 1892–1906. arXiv: 1601.02384 [astro-ph.SR] (June 2016).
71. Shepherd, D. S. *et al.* Molecular Outflows and a Mid-Infrared Census of the Massive Star Formation Region Associated with IRAS 18507+0121. *ApJ* **669,** 464–482. arXiv: 0706.4330 [astro-ph] (Nov. 2007).
72. Shu, F. H., Adams, F. C. & Lizano, S. Star formation in molecular clouds: observation and theory. *ARA&A* **25,** 23–81 (Jan. 1987).
73. Silva, A. *et al.* SMA Observations of the Hot Molecular Core IRAS 18566+0408. *ApJ* **847,** 87. arXiv: 1708.07431 [astro-ph.GA] (Oct. 2017).
74. Solomon, P. M., Jefferts, K. B., Penzias, A. A. & Wilson, R. W. Detection of Millimeter Emission Lines from Interstellar Methyl Cyanide. *ApJ* **168,** L107 (Sept. 1971).
75. Tan, J. C. *et al. Massive Star Formation* in *Protostars and Planets VI* (eds Beuther, H., Klessen, R. S., Dullemond, C. P. & Henning, T.) (Jan. 2014), 149. arXiv: 1402.0919 [astro-ph.GA].
76. Tan, J. C. *Fire from Ice - Massive Star Birth from Infrared Dark Clouds* in *IAU Symposium* (eds Cunningham, M., Millar, T. & Aikawa, Y.) **332** (Sept. 2018), 139–152. arXiv: 1710.11607 [astro-ph.GA].
77. Terebey, S., Shu, F. H. & Cassen, P. The collapse of the cores of slowly rotating isothermal clouds. *ApJ* **286,** 529–551 (Nov. 1984).
78. Tielens, A. G. G. M. & Hagen, W. Model calculations of the molecular composition of interstellar grain mantles. *A&A* **114,** 245–260 (Oct. 1982).
79. Toomre, A. On the gravitational stability of a disk of stars. *ApJ* **139,** 1217–1238 (May 1964).

80. Turner, B. E. A Molecular Line Survey of Sagittarius B2 and Orion–KL from 70 to 115 GHz. II. Analysis of the Data. *ApJ* **76,** 617 (June 1991).
81. van der Tak, F. F. S., Black, J. H., Schöier, F. L., Jansen, D. J. & van Dishoeck, E. F. A computer program for fast non-LTE analysis of interstellar line spectra. With diagnostic plots to interpret observed line intensity ratios. *A&A* **468,** 627–635. arXiv: 0704.0155 [astro-ph] (June 2007).
82. van der Tak, F. F. S. *The chemistry of high-mass star formation* in *Massive Star Birth: A Crossroads of Astrophysics* (eds Cesaroni, R., Felli, M., Churchwell, E. & Walmsley, M.) **227** (Jan. 2005), 70–79. arXiv: astro-ph/0506146 [astro-ph].
83. van der Walt, D. J. Pumping of the 4.8 GHz H_2CO masers and its implications for the periodic masers in G37.55+0.20. *A&A* **562,** A68. arXiv: 1312.6212 [astro-ph.GA] (Feb. 2014).
84. Vastel, C., Bottinelli, S., Caux, E., Glorian, J. M. & Boiziot, M. *CASSIS: a tool to visualize and analyse instrumental and synthetic spectra.* in *SF2A-2015: Proceedings of the Annual meeting of the French Society of Astronomy and Astrophysics* (Dec. 2015), 313–316.
85. Viti, S. & Williams, D. A. Time-dependent evaporation of icy mantles in hot cores. *MNRAS* **305,** 755–762 (May 1999).
86. Vitrichenko, E. A., Nadyozhin, D. K. & Razinkova, T. L. Mass—luminosity relation for massive stars. *Astronomy Letters* **33,** 427–427 (June 2007).
87. Wang, K. S., van der Tak, F. F. S. & Hogerheijde, M. R. Kinematics of the inner thousand AU region around the young massive star AFGL 2591-VLA3: a massive disk candidate? *A&A* **543,** A22. arXiv: 1204.4367 [astro-ph.GA] (July 2012).
88. Wang, K.-S. *Small scale kinematics of massive star-forming cores* PhD thesis (Leiden University, Dec. 2013).
89. Watanabe, Y. *et al.* Discovery of Striking Difference of Molecular-emission-line Richness in the Potential Proto-binary System NGC 2264 CMM3. *ApJ* **847,** 108. arXiv: 1708.07582 [astro-ph.GA] (Oct. 2017).
90. Wright, N. J. The Kinematics of Star Formation: Theory and Observation in the Gaia Era. *arXiv e-prints,* arXiv:1512.06854. arXiv: 1512.06854 [astro-ph.SR] (Dec. 2015).
91. Yorke, H. W. & Bodenheimer, P. The Formation of Protostellar Disks. III. The Influence of Gravitationally Induced Angular Momentum Transport on Disk Structure and Appearance. *ApJ* **525,** 330–342 (Nov. 1999).
92. Zapata, L. A. *et al.* ALMA reveals a candidate hot and compact disc around the O-type protostar IRAS 16547-4247. *MNRAS* **447,** 1826–1833. arXiv: 1411.7421 [astro-ph.SR] (Feb. 2015).
93. Zhang, Q. *et al.* A jet-like outflow toward the high-mass (proto) stellar object IRAS 18566+0408. *A&A* **470,** 269–279. arXiv: 0704.2767 [astro-ph] (July 2007).
94. Zinnecker, H. & Yorke, H. W. Toward Understanding Massive Star Formation. *ARAA* **45,** 481–563. arXiv: 0707.1279 [astro-ph] (Sept. 2007).